

Effect of surface roughness on fatigue performance of additive manufactured Ti–6Al–4V

D. Greitemeier^{*1}, C. Dalle Donne¹, F. Syassen², J. Eufinger³ and T. Melz³

Additive manufacturing is increasingly considered for production of high quality, metallic, aerospace parts. Despite the high potential of this manufacturing process to reduce weight and lead time, the fundamental understanding of additive manufactured Ti–6Al–4V material is still at an early stage, especially in the area of fatigue and damage tolerance. This paper covers the effects of inherent surface roughness on the fatigue life. In the as built condition, metallic parts have a poor surface texture, which is generally removed in fatigue critical areas. It is shown that the fatigue properties of Ti–6Al–4V samples, produced by direct metal laser sintering and electron beam melting, are dominated by surface roughness effects. A simple model based on an equivalent initial flaw size is formulated.

Keywords: Ti–6Al–4V, Additive manufacturing, Fatigue, EBM, DMLS, Surface roughness, Fracture mechanics, EIFS

Introduction

Additive manufacturing (AM) can produce complex shaped metallic parts without the need for dies, form tools or moulds. The parts are effectively grown rather than machined from a larger block. A three-dimensional model is virtually sliced into thin layers and sent to a manufacturing unit, in which an energy source directly builds the part by joining material layer by layer.^{1,2} Lead time reduction and design freedom are some of the main drivers for AM within the aerospace industry.^{2,3} Compared to metallic forged or cast components, better material utilisation and the avoidance of tooling lead to potentially lower costs, whereas the design freedom is an enabler for weight savings through topology optimisation.

It is known that the AM process produces a new material challenges with associated features like defects or inherent surface roughness, which can lower the fatigue performance.^{4–6} However, it is shown for additive manufactured Ti–6Al–4V using wire that in the absence of these features, the mechanical properties can be compared to wrought material.⁷ The same trend can be seen for powder bed processes, if a post-processing, like hot isostatic pressing (HIP), is applied to reduce internal defects of milled specimens. In the absence of defects, the fatigue performance is increased and scatter is reduced.⁵

Aside from the effect of defects, recent studies have investigated the influence of surface roughness on the

fatigue performance.^{6,8–10} Wycisk *et al.*⁸ reported a significant lower endurance limit of ~210 MPa ($R=0.1$, $K_t = 1$) for specimens with inherent surface roughness compared to polished one (500 MPa).

Mastering the influence of inherent surface roughness from a damage tolerance assessment point of view could be key to assure the reliability of future structural applications.

In the framework of a larger effort undertaken in Airbus Group, this work will describe the fatigue performance of Ti–6Al–4V samples, produced by direct metal laser sintering (DMLS) and electron beam melting (EBM), with rough surfaces (as built). The aim is to offer a better experimental documentation, as well as to elaborate a practical engineering approach, to estimate the fatigue performance of as built specimens based on linear elastic fracture mechanics.

Experimental

Manufacturing process and heat treatment

Two different manufacturing processes are investigated; in the first, samples are produced by DMLS using an EOSINT M 280 (EOS) platform, with the standard parameter from EOS, shown in Table 1. The builds take place under protective argon atmosphere, with a process chamber temperature of ~35°C. The scan strategy is based on a shell and core concept, rotating each layer with an angle of 30°. The second method utilises EBM performed using an ARCAM A2 (ARCAM AB) platform to manufacture identical samples and thus provide a direct comparison between the techniques (Table 1). Unlike DMLS, the EBM process is performed under vacuum (~5x10³ mbar), with a process chamber temperature of ~620°C. The utilised shell core scan strategy alternates each layer between 0 and 90°.

¹Airbus Group Innovations, 81663 Munich, Germany

²Airbus Operations, 28199 Bremen, Germany

³Fraunhofer Institute for Structural Durability and System Reliability LBF, 64289 Darmstadt, Germany

*Corresponding author, email daniel.greitemeier@airbus.com

Table 1 Used parameters for DMLS and EBM Ti-6Al-4V

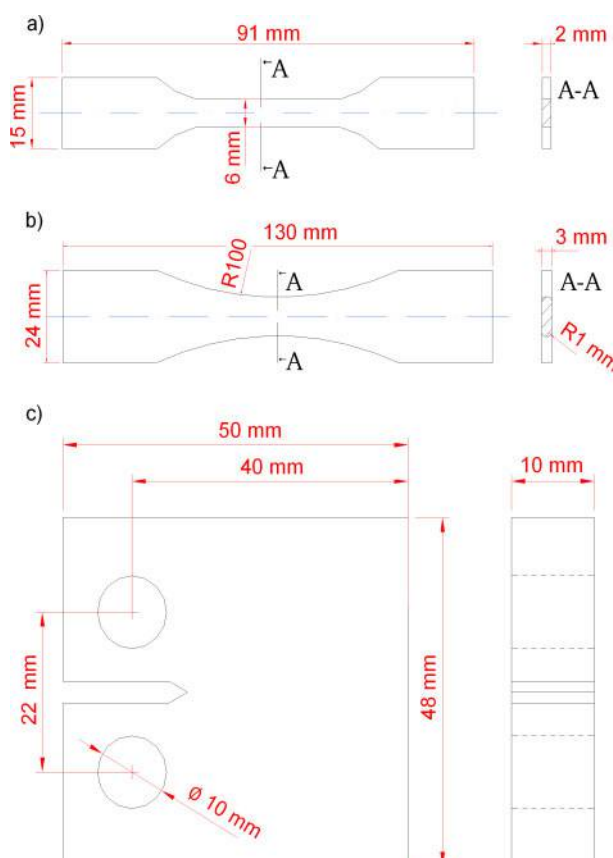
Process	DMLS	EBM
Machine	EOSINT M 280	ARCAM A2
Power/W	370	50–3500
Scan speed/mm s ⁻¹	≤7000	≤8 × 10 ⁶
Layer thickness/μm	60	50

All parts are heat treated at 710°C for 2 h under vacuum, followed by furnace cooling under argon atmosphere, to reduce residual stresses.¹¹ Especially for DMLS parts, high cooling rates and steep temperature gradients can tend toward the formation of residual stresses within the as built parts.¹² Leuders *et al.*¹³ investigated residual stress for DMLS parts before and after an applied heat treatment at 800°C for 2 h. Nearly no residual stress remained in the material.

Mechanical characterisation

Static tensile, axial fatigue and fatigue crack growth tests are performed at ambient condition. The load is applied perpendicular to the layer deposition direction.

- (i) Static tensile tests are performed on a servo hydraulic test machine Z 250 (Zwick), in accordance to EN 2002,¹⁴ on flat specimens (Fig. 1a). A strain rate of 0.5% min⁻¹ is applied for yield stress at 0.2% ($R_{p,0.2}$) and 2% min⁻¹ for tensile strength (R_m). Elongation (A) is calculated based on an extensometer gauge length of 20 mm. Three to four test samples are used to calculate an average value.



1 Specimen geometries: a static tensile test specimen, b axial fatigue test specimens and c fatigue crack growth tests specimens

(ii) Axial fatigue tests are performed on a resonant testing machine, Microtron 2 (Rumul), in accordance to EN 6072.¹⁵ Flat specimens ($K_t = 1$; Fig. 1b) are tested under a constant load, with a load ratio of $R = 0.1$ at 150 Hz. It has to be noted that the reported fatigue limit is statistically not proven due to the amount of 10–11 specimens for each SN curve.

(iii) Fatigue crack growth tests are performed using a servo hydraulic test device, PC 160N (Schenck), in accordance to American Society for Testing and Materials (ASTM) E 647.¹⁶ A compact tension specimen [C (T) 40, Fig. 1c] is used under constant load ($R = 0.1$). The crack size is measured by the electrical potential drop method.

Roughness measurements

Roughness measurements are performed using contact profilometry with a DektakXT (Bruker) in accordance with DIN EN ISO 4288:1998.¹⁷ The average value of three measuring sections in the build direction describes the arithmetic average height (R_a) and the maximum height (R_t) of the profile. All measurements are based on the used axial fatigue specimens.

Estimation model

A simple estimation model is proposed based on the equivalent initial flaw size (EIFS) approach to total life estimation. In short, this is a method where cracks are analytically grown backwards to a time equal to zero (time or cycles) to determine an initial flaw, referred to as an EIFS. By growing a number of cracks back to a time equal to zero, a distribution of EIFS can therefore be established; the method is widely used within commercial aerospace manufacturing.^{18–20} Here, a deterministic approach is utilised for simplicity.

Takahashi and Murakami²¹ have shown that it is possible to relate characteristic surface roughness values to an EIFS. On the basis of these findings, an EIFS is back extrapolated from SN data and linked to the experimentally determined surface roughness value (R_t). The flaw geometry is described by a semielliptical surface crack.

The calculation of the stress intensity factor (SIF) is taken to be

$$K_{NR} = \left((\sigma_n + H_s S_b) \left(\frac{\pi a}{Q} \right) \right)^{0.5} \cdot F_s \left(\frac{a}{c}, \frac{a}{t}, \frac{c}{b}, \phi \right)$$

The first term contains the uniform tension stress (σ_n), a correction factor for bending ($H_s S_b$), the crack length (a) and a shape factor (Q), which is multiplied by F_s as a function of crack depth (ϕ) and length ($c = a/2$), plate thickness (t) and width (b), as well as a parametric angle (ϕ) of the ellipse. Detailed description of all parameters can be found in the work of Newman and Raju.²²

The experimentally determined crack growth curves are described by the Forman/Mettu equation (NASGRO crack growth equation):

$$\frac{da}{dN} = C_{FM} * \left[\left(\frac{1 - \gamma}{1 - R} \right) \Delta K_I \right]^{n_{FM}} * \frac{\left(1 - \frac{\Delta K_{I,th}}{\Delta K_I} \right)^P}{\left(1 - \frac{K_{I,max}}{K_{IC}} \right)^q}$$

Beside the cyclic SIF threshold ($\Delta K_{I,\text{th}}$), the cyclic SIF (ΔK_I), the fracture toughness (K_{ic}) and the maximum SIF ($K_{I,\text{max}}$), C_{FM} , N_{FM} , p and q are constants describing the slope and shape of the curve. Crack closure effects are considered by γ .

Detailed descriptions including all parameters can be found in the work of Forman and Mettu.²³

By combining both equations, the initial crack length (a_i) can be calculated based on the cycles to failure (N_F) for each experimental value as follows:

$$N_F = \int_0^{N_F} dN = \frac{1}{C_{\text{FM}}} \int_{a_i}^{a_c} \left(\left[\left(\frac{1-\gamma}{1-R} \right) \Delta K_{I,NR} \right]^{nFM} * \frac{\left(1 - \frac{\Delta K_{I,\text{th},NR}}{\Delta K_{I,MR}} \right)^p}{\left(1 - \frac{K_{I,\text{max},NR}}{K_{\text{IC}}} \right)^q} \right)^{-1} * da$$

The calculated initial crack length is then set equal to the determined surface roughness parameter R_t .

SN curves are estimated for different surface roughness by the assumption of a linear relationship between surface roughness and EIFS.

In order to keep the model as simple as possible, the following assumptions are made:

- (i) Fatigue life estimations are based on linear elastic fracture mechanics.
- (ii) Fatigue crack initiation is neglected.
- (iii) Fatigue crack propagation of short cracks is neglected.

Results

Roughness characterisation

The surface roughness can influence the fatigue performance due to multiple stress concentrations. Figure 2 therefore shows a typical DMLS (Fig. 2a) and EBM (Fig. 2b) surface.

It is notable that both processes show two types of roughness:

- (i) Roughness induced due to solidification of the melt pool (primary roughness).
- (ii) Roughness induced by partly melted powder particles (secondary roughness).

The results from the sieve analysis, in accordance to ASTM B214, indicate a maximum particle size for EBM powder more than twice as high as for DMLS, which results in a higher surface roughness of the EBM material.

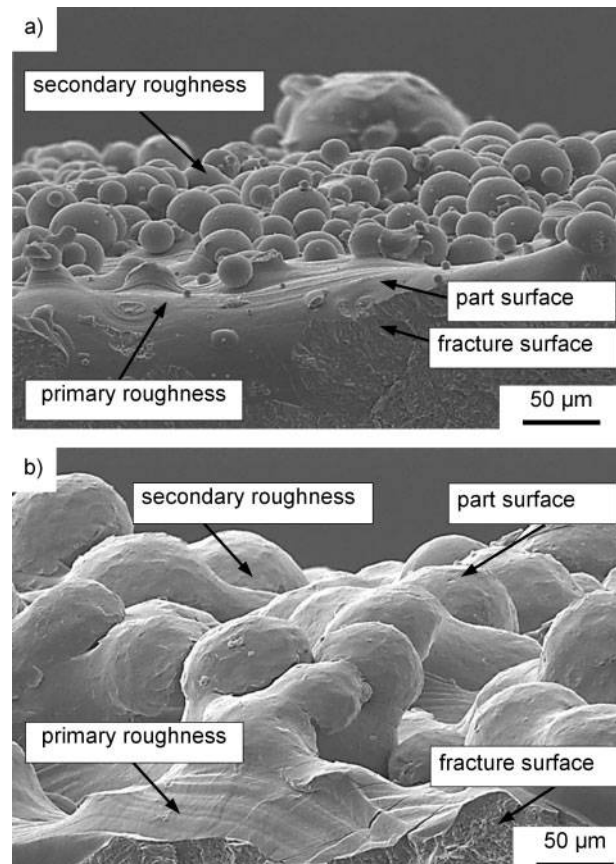
As a result, the roughness values for the EBM specimens are greater (R_a : 27 µm, R_t : 214 µm) when compared directly to the DMLS specimens (R_a : 13 µm, R_t : 110 µm), shown in Table 2.

Mechanical characterisation

Tensile properties

The tensile properties are summarised in Table 3. Each test series consists of three to four specimens. The DMLS tensile specimens show high ultimate tensile strength (UTS) of 1096 MPa, with elongation of 12%. The average UTS of the EBM specimens is slightly lower at 965 MPa, while elongation is reduced to 6%.

It has to be noted that defects can be detected on the fracture surface of the EBM specimens. Furthermore, initial chemical analysis of the specimens reveals



2 Surface roughness of Ti-6Al-4V: a DMLS (side view), b EBM (side view)

Table 2 Surface roughness values for DMLS and EBM Ti-6Al-4V, in build direction, according to DIN EN ISO 4288:1998¹⁷

Process	$R_a/\mu\text{m}$	$R_t/\mu\text{m}$
DMLS	13.03 ± 0.72	109.88 ± 0.62
EBM	27.12 ± 0.91	214.01 ± 9.62

Table 3 Average tensile tension properties including standard deviation for DMLS and EBM Ti-6Al-4V, build direction: ZX, heat treatment: 710°C/2 h, surface: as built

Process	UTS (R_m)/MPa	YS ($R_{p0,2}$)/MPa	A/%	Z/%
DMLS	1096 ± 7	1017 ± 7	12 ± 0.5	15 ± 0.9
EBM	965 ± 5	869 ± 7	6 ± 0	5 ± 5

a notably lower aluminium content (DMLS: 6.5 wt.-%, EBM 5.9 wt.-%) and lower oxygen content (DMLS: 0.17 wt.-%, EBM 0.13 wt.-%) for the EBM specimens.

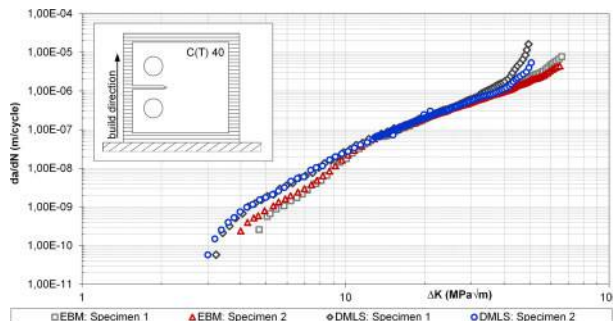
Fatigue crack growth properties

To estimate the fatigue properties, the crack growth was measured and plotted logarithmically as a function of the stress intensity range (Fig. 3).

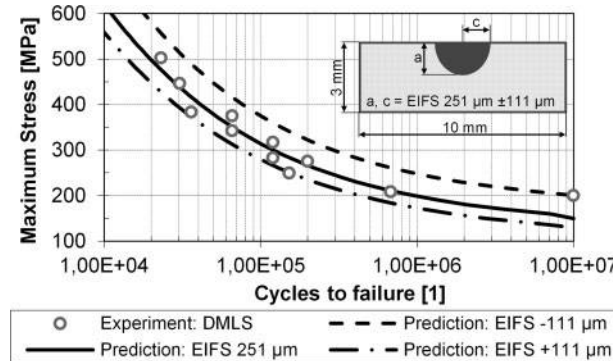
The processes differ mainly in the threshold regime, where the crack growth is reduced for the EBM specimens.

Experimental and estimated high cycle fatigue properties

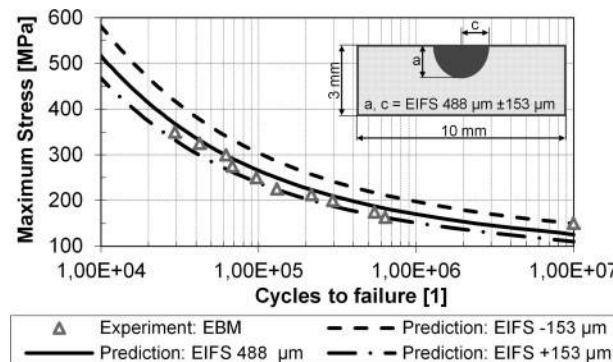
The high cycle fatigue behaviours of DMLS and EBM Ti-6Al-4V are plotted in Figs. 4 and 5. Fractographic



3 Fatigue crack growth properties of DMLS and EBM Ti-6Al-4V, C (T) 40, $R = 0.1$, build direction: XZ, heat treatment: $710^{\circ}\text{C}/2\text{ h}$, surface: milled



4 Description of experimental results for Ti-6Al-4V DMLS specimens based on an EIFS, $R = 0.1$, $K_t = 1$, heat treatment: $710^{\circ}\text{C}/2\text{ h}$



5 Description of experimental results for Ti-6Al-4V EBM specimens based on EIFS, $R = 0.1$, $K_t = 1$, heat treatment: $710^{\circ}\text{C}/2\text{ h}$

analysis reveals multiple cracks initiating at the surface. Standard deviations of 19.6 MPa for DMLS and 6.5 MPa for EBM were calculated based on an SN curve with 50% probability of failure. The fatigue limit (1×10^7) is slightly higher for the DMLS specimens when compared directly to the EBM specimens (DMLS: $S_{\max} = 200$ MPa, EBM: $S_{\max} = 150$ MPa).

To estimate the influence of surface roughness on linear elastic fracture mechanics, an EIFS is calculated to capture both the experimental measurements and the scatter. The fatigue performance of the DMLS specimens can be therefore completely described by an EIFS of $251 \mu\text{m} \pm 111 \mu\text{m}$ (Fig. 4), while an EIFS of $488 \mu\text{m} \pm 153 \mu\text{m}$ describes the SN curve (including the scatter) for the EBM specimens (Fig. 5).

Figure 6 displays the resulting EIFS for different R_t . It has to be noted that this correlation is based on the averaged values of Fig. 4 (EIFS: $251 \mu\text{m}$), Fig. 5 (EIFS: $488 \mu\text{m}$), and results of HIP and milled specimens.

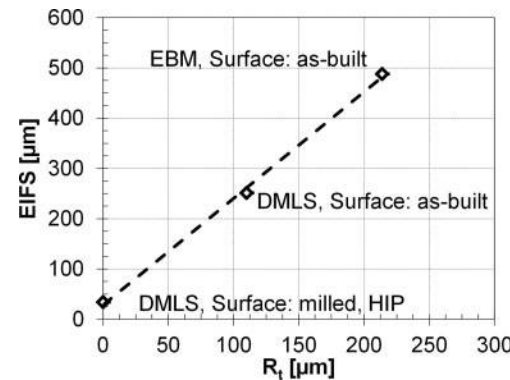
HIPed DMLS material was used to reduce the size of (internal) defects, which can distract the influence of surface roughness on fatigue performance. Although the use of HIP tends toward a more coarse microstructure (which also has a subsequent impact on the fatigue performance), internal defects were deemed to be more critical.

Based on Fig. 6, estimations are made for SN curves with different surface roughness (Fig. 7) and compared with literature values.^{8,10,24} Fatigue crack growth curves of DMLS material (Fig. 3) are used as input for this estimation.

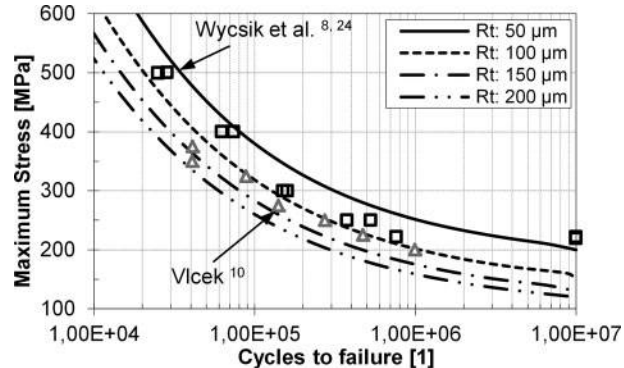
Wycsik *et al.*^{8,24} investigated the fatigue properties of as built, round, DMLS, Ti-6Al-4V specimens ($K_t = 1$), with an r ratio of 0.1. The specimens were subsequently heat treated at $650^{\circ}\text{C}/3\text{ h}$; a maximum surface roughness (R_t) of $90 \mu\text{m}$ was then determined. This experimental value is in accordance to the estimated range of R_t : $50\text{--}100 \mu\text{m}$.

Vlcek¹⁰ investigated the fatigue properties of as built, DMLS, Ti-6Al-4V. The round specimens ($K_t = 1$) were tumbled with ceramic stones to reduce the surface roughness ($R_t = 165 \mu\text{m}$) and hot isostatic pressed at $843^{\circ}\text{C}/4\text{ h}/1000$ bars. Fatigue properties were evaluated at an r ratio of 0.1. The estimation indicates a surface roughness of $100\text{--}200 \mu\text{m}$ (R_t).

It must be noted that the heat treatment of both literature data sets differs from the materials investigated here. Therefore, the da/dN - ΔK curves of the literature data sets may be different.



6 Calculation of EIFS from maximum height of profile (R_t)



7 SN curves for different EIFS based on crack growth rates of DMLS Ti-6Al-4V compared with literature data^{8,10,24}

Discussion

Tensile tests

Through comparison of the measured tensile properties, it can be seen that the EBM specimens demonstrate a slightly lower UTS and YS when compared to their DMLS counterparts. Several factors can have an influence on the results: process related defects can tend toward a reduced cross-section and therefore lower the tensile properties; chemical composition is a further important aspect that can lead to decreased tensile properties; indeed, it was noted that the strength improving²⁵ elements Al and O are reduced in the manufactured EBM specimens; microstructure and therefore build temperature and post-heat treatment can heavily influence the YS due to a coarsening of the microstructure, as reported by Filip *et al.*,²⁶ for lamellar two-phase titanium alloys. Which of these factors are responsible for the lower tensile properties must be evaluated in detail in future studies.

Optimised EBM process parameters may help to avoid defects and evaporation of Al.²⁷ Additionally, chemical analysis of the powder could help to understand the influence of oxygen on the mechanical properties of additive manufactured Ti-6Al-4V as Gysler and Lütjering²⁸ reported for Ti-6Al-4V.

Fatigue crack growth

In the presence of large cracks, fatigue crack growth resistance can partly be ascribed to the underlying microstructure, as reviewed by Lütjering and Williams.²⁹ A coarser lamella size therefore increases crack growth rates. Crack deflection due to roughness induced crack closure could be responsible for the increased resistance of crack growth near the threshold ($R \sim 0.1$).^{25,29}

Similar conclusion can be made for the different crack growth behaviour of EBM and DMLS (Fig. 3). It is known from the literature that the microstructure of Ti-6Al-4V EBM is generally coarser than that of DMLS.^{5,30}

Experimental high cycle fatigue properties

Although the fatigue behaviour of AM Ti-6Al-4V depends in general upon a number of mechanical, microstructural and chemical factors,³¹ it seems that the presence of surface roughness, dependent on the process and powder used, is the dominant factor for the low fatigue performance of AM Ti-6Al-4V when compared to AM milled material.³² This can also be concluded from the point of crack initiation, which starts from stress concentrations at the surface and not from defects or non-homogeneous microstructure.

It has to be noted that the influence of defects on the fatigue performance is only negligible to a certain size.

The lower fatigue limits of the EBM specimens can therefore be ascribed to the surface roughness, which tends toward higher stress concentrations, resulting in a lower fatigue limit when compared to the DMLS material. The determined experimental fatigue limits are in accordance with the recent literature for DMLS (S_{max} : 210 MPa³³) and EBM (S_{max} : 150 MPa³³) Ti-6Al-4V material.

Estimated high cycle fatigue properties

Both Figs. 4 and 5 indicate that, for smooth specimens, the surface roughness effect can be described by a unique

EIFS value using a fracture mechanics approach. A linear relationship between EIFS and R_t was used to successfully estimate SN data of additively manufactured Ti-6Al-4V.

Although these results appear promising, it has to be noted that the verification of the model is based only on small and un-notched specimens, solicited by constant amplitude loading. Therefore, more extensive validation with more realistic specimen designs (i.e. notched) and loading conditions (variable amplitude loading and multiaxial loading) must be undertaken in any future work.

Conclusions

Two different AM technologies have been investigated for comparison reasons. An experimental test programme was performed in order to determine the influence of surface roughness on fatigue performance of additive manufactured specimens. First insights in estimating the influence of surface roughness have been given and compared to literature data.

The following conclusions can be drawn:

1. High cycle fatigue properties are dominated by surface roughness (direct metal laser sintered specimens: $R_t = 110 \mu\text{m}$, electron beam melted specimens: $R_t = 214 \mu\text{m}$).
2. The crack growth rate differs between electron beam melted and direct metal laser sintered specimens in the near threshold regime.
3. Estimation of fatigue life based on an EIFS seems to be a suitable approach to estimating the influence of surface roughness on fatigue life.

Acknowledgement

The author would like to thank Vitus Holzinger, Christian Pander, Dieter Meixner, Martin Muir and Wolfgang von Bestenbostel for their support.

References

1. D. D. Gu, W. Meiners, K. Wissenbach and R. Proprawé: 'Laser additive manufacturing of metallic components: materials, processes and mechanisms', *Int. Mater. Rev.*, 2012, **57**, (3), 133–164.
2. P. A. Kobryn and S. L. Semiatin: 'The laser additive manufacture of Ti-6Al-4V', *JOM*, 2001, **53**, (9), 40–42.
3. I. Gibson, D. W. Rosen and B. Stucker: 'Additive manufacturing technologies: rapid prototyping to direct digital manufacturing'; 2009, New York, Springer.
4. K. S. Chan, M. Koike, R. L. Mason and T. Okabe: 'Fatigue life of titanium alloys fabricated by additive layer manufacturing techniques for dental implants', *Metall. Mater. Trans. A*, 2013, **44**, (2), 1010–1022.
5. D. Greitemeier, K. Schmidke, V. Holzinger and C. Dalle Donne: 'Additive layer manufacturing of Ti-6Al-4V and scalmalloyRP: fatigue and fracture', 27th ICAF Symposium, Jerusalem; 2013
6. E. Wycisk, C. Emmelmann, S. Siddique and F. Walther: 'High cycle fatigue (HCF) performance of Ti-6Al-4V alloy processed by selective laser melting', *Adv. Mater. Res.*, 2013, **816**, 134–139.
7. E. Brandl: 'Microstructural and mechanical properties of additive manufactured titanium (Ti-6Al-4V) using wire, evaluation with respect to additive processes using powder and aerospace material specifications'; 2010, Aachen, Technische Universität Cottbus.
8. E. Wycisk, A. Solbach, S. Siddique, D. Herzog, F. Walther and C. Emmelmann: 'Effects of defects in laser additive manufactured Ti-6Al-4V on fatigue properties', *Phys. Proc.*, 2014, **56**, 371–378.

9. P. Edwards and M. Ramulu: 'Fatigue performance evaluation of selective laser melted Ti-6Al-4V', *Mater. Sci. Eng. A*, 2014, **A598**, 327–337.
10. J. Vlcek: 'Property investigation of Ti-Al6-V4 produced by additive manufacturing', TMS 2007, 136th Annual Meeting & Exhibition, Minerals, Metals and Materials Society/Light Metals 2007, 89–98.
11. ASM International: 'ASM handbook: vol. 4: heat treating'; 1991, Materials Park, OH, ASM International.
12. M. Shiomii, K. Osakada, K. Nakamura, T. Yamashita and F. Abe: 'Residual stress within metallic model made by selective laser melting process', *CIRP Ann*, 2004, **53**, (1), 195–198.
13. S. Leuders, M. Thöne, A. Riemer, T. Niendorf, T. Tröster, H. A. Richard and H. J. Maier: 'On the mechanical behaviour of titanium alloy TiAl6V4 manufactured by selective laser melting: fatigue resistance and crack growth performance', *Int. J. Fatigue*, 2013, **48**, 300–307.
14. G. I.F. Standardisation: 'Aerospace series – metallic materials – test methods – part 1: tensile testing at ambient temperature'; 2006.
15. A. o.E.A.a.C. Manufacturers: 'Aerospace series – metallic materials – test methods – constant amplitude fatigue testing', 2008
16. A. International: 'Standard test method for measurement of fatigue crack growth rates'.
17. G. I.o. Standardisation: 'Geometrical product specifications (GPS) – surface texture: profile method – rules and procedures for the assessment of surface texture', 1998.
18. W. S. Jonson, R. A. Heller and J. N. Yang: 'Flight inspection data and crack initiation times', *Proc. Annu. Reliab. Maintain. Symp*, 1977, 148–154.
19. W. S. Johnson: 'The history, logic and uses of the equivalent initial flaw size approach to total fatigue life prediction', *Proc. Eng*, 2010, **2**, (1), 47–58.
20. S. A. Fawaz: 'Equivalent initial flaw size testing and analysis of transport aircraft skin splices', *Fatigue Fract. Eng. Mater. Struct*, 2003, **26**, (3), 279–290.
21. K. Takahashi and Y. Murakami: 'Quantitative evaluation of effect of surface roughness on fatigue strength', 693–703; 1999, Sheffield, UK, Engineering Against Fatigue.
22. J. C. Newman Jr. and I. S. Raju: 'Stress-intensity factor equations for cracks in three-dimensional finite bodies subjected to tension and bending loads', *Comput. Methods Mech. Fract*, 1986, **2**, 312–334.
23. R. G. Forman and S. R. Mettu: 'Behavior of surface and corner cracks subjected to tensile and bending loads in Ti-6AL-4V alloy'; 1990, Houston, TX, National Aeronautics and Space Administration.
24. E. Wycisk, J. Kranz and C. Emmelmann: 'Influence of surface properties on fatigue strength of light weight structures produced by laser additive manufacturing in TiAl6V4', DDMC Direct Digital Manufacturing Fraunhofer Conference, Berlin; 2012.
25. S. R. Lampman: 'ASM handbook: volume 19: fatigue and fracture'; 1997, Materials Park, OH, ASM International.
26. R. Filip, K. Kubiak, W. Ziaja and J. Sieniawski: 'The effect of microstructure on the mechanical properties of two-phase titanium alloys', *J. Mater. Process. Technol*, 2003, **133**, (1–2), 84–89.
27. V. Juechter, T. Scharowsky, R. F. Singer and C. Körner: 'Processing window and evaporation phenomena for Ti-6Al-4V produced by selective electron beam melting', *Acta Mater*, 2014, **76**, 252–258.
28. A. Gysler and G. Lütjering: 'Influence of test temperature and microstructure on the tensile properties of titanium alloys', *Metall. Trans. A*, 1982, **13A**, (8), 1435–1443.
29. G. Lütjering and J. C. Williams: 'Titanium'; 2003, New York, Springer.
30. A. A. Antonysamy: 'Microstructure, texture and mechanical property evolution during additive manufacturing of Ti6Al4V alloy for aerospace applications'; 2012, Manchester, University of Manchester.
31. R. Boyer, G. Welsch and E. W. Collings: 'Materials properties handbook, titanium alloys'; 1998, Materials Park, OH, ASM International.
32. E. Brandl, D. Greitemeier, H. J. Maier and F. Syassen: 'High cycle fatigue properties of electron beam melted Ti-6Al-4V samples without and with integrated defects ("effects of defects")', European Conference on Spacecraft Structures, Materials and Environmental Testing, Noordwijkerhout (Netherlands); 2012.
33. H. K. Rafi, N. V. Karthik, T. L. Starr and B. E. Stucker: 'Mechanical property evaluation of Ti-6Al-4V parts made using electron beam melting'. International Solid Freeform Fabrication Symposium, Austin, TX, 2012, Laboratory for Freeform Fabrication and University of Texas at Austin.

P. Edwards

Boeing Research & Technology,
The Boeing Company,
Seattle, WA 98124
e-mail: Paul.D.Edwards2@boeing.com

A. O'Conner

Graduate Assistant
e-mail: apoc@u.washington.edu

M. Ramulu¹

Boeing-Pennell Professor of Engineering
e-mail: ramulum@u.washington.edu

Department of Mechanical Engineering,
University of Washington,
Seattle, WA 98195

Electron Beam Additive Manufacturing of Titanium Components: Properties and Performance

This research evaluates the fatigue properties of Ti-6Al-4V specimens and components produced by Electron Beam additive manufacturing. It was found that the fatigue performance of specimens produced by additive manufacturing is significantly lower than that of wrought material due to defects such as porosity and surface roughness. However, evaluation of an actual component subjected to design fatigue loads did not result in premature failure as anticipated by specimen testing. Metallography, residual stress, static strength and elongation, fracture toughness, crack growth, and the effect of post processing operations such as machining and peening on fatigue performance were also evaluated. [DOI: 10.1115/1.4025773]

Keywords: additive manufacturing, electron beam, titanium, fatigue, fracture

1 Introduction

With traditional manufacturing processes, such as machining from wrought plate, the design of the part is constrained by the geometries that can be feasibly produced by the machining process. An example of a small machined titanium bracket, or clip, is shown in Fig. 1(a). The machining process geometric produceability constraints often result in parts with more material, and weight, than is actually needed to safely support the design loads. However, the complex geometric build capabilities of additive manufacturing (AM) can provide nearly complete design freedom. By combining design optimization and AM, parts can be produced with material only where it is needed to transfer the required design loads, resulting in significant weight reductions. Figure 1(b) shows an example of the same bracket, Fig. 1(a), with a numerically optimized design that is 48% lighter than the machined part design.

Although AM holds promise for reducing the weight of aerospace structures, it must be shown that the mechanical performance of AM parts will meet stringent commercial aerospace design criteria. A number of AM processes are currently available [1,2] and most studies performed on titanium, specifically Ti-6Al-4V, are defined by their heat source, such as electron beam [3–12], Laser [12–23] or Arc [21,22], and how the raw material is supplied, such as layers of powder where selected regions are melted and the unmelted powder is subsequently removed [1–20] or when material, such as solid wire or powder, is directly deposited onto a base plate [21,22]. In order to utilize these AM technologies to leverage their ability to produce novel light weight designs for structural applications, the static, fatigue, and damage tolerance performance of specimens and components subjected to a variety of post processing conditions must be assessed and understood. AM of titanium is of particular interest due to its increased usage in aerospace structures for it is thermal and galvanic compatibility with composites.

The static performance of Ti-6Al-4V parts produced by AM is dependent on the particular AM technique used, processing conditions, post deposition heat treatment, location in build envelope and orientation, among other variables. However, AM is generally found to be comparable to wrought Ti-6Al-4V ultimate strength,

yield strength, and elongation [3,8,12,20–22]. Related to the static properties, microstructures and hardness are also dependent on these same variables. Microstructures have been characterized as acicular alpha in prior beta grains [3,4], very fine lamellar [7], alpha laths in prior beta [6], or prior beta grains that grow across build layers [21,22]. Process conducted outside of an elevated temperature build chamber, like Laser and Arc, can result in martensitic structure [20]. Inhomogeneous microstructures due to the build direction can lead to the location and orientation dependence on the mechanical performance of the parts [5]. Heat treatment can reduce, or eliminate, residual stresses as well as coarsen the lamellar alpha structure and dissolve the martensite, which may lower the strength slightly, but recover ductility [20]. Heat treatment has a larger impact on laser processes [20] compared to electron beam [7] because electron beam processes are typically carried out in build chambers at temperatures ranging from 600 to 700 °C, which essentially stress relieves the parts in situ.

While microstructures and static properties are important, characterization of fatigue and damage tolerance performance is often more difficult, time consuming, and costly. In addition, it is challenging to clearly define, the most critical aspects in design for long life, safety critical, high performance structures, such as those in commercial aerospace. As with static properties, fatigue and damage tolerance are also dependent on similar process variables, but in fatigue, surface condition and porosity have the most

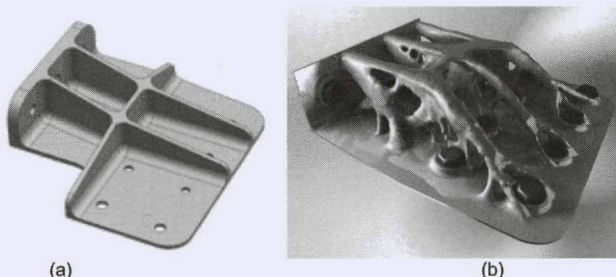


Fig. 1 (a) Typical titanium aerospace bracket made by machining from wrought material and (b) optimized design based on the loading conditions leveraging the build capabilities of additive manufacturing. Drawings are not to scale.

¹Corresponding author.

Manuscript received April 30, 2013; final manuscript received October 17, 2013; published online November 18, 2013. Assoc. Editor: Yung Shin.

significant impact on fatigue performance [7,8,20–22]. Leuders et al. [20] evaluated the fatigue and crack growth characteristics of Ti-6Al-4V manufactured by selective laser melting (SLM). It was found that in the as-built condition, the fatigue strength was significantly reduced due to porosity. However, when hot isostatic pressed (HIP'ed), the fatigue strength became more comparable to conventionally processed titanium alloys. With respect to crack growth, the controlling factor was internal residual stresses, but regardless of post process heat treatment the crack growth behavior was similar to wrought titanium. Chan et al. [8] studied the fatigue performance of Ti-6Al-4V ELI materials produced by both electron beam melting (EBM) and SLM with both as-built and electro discharged machined (EDM) surfaces. In all cases, the performance of wrought material was significantly better than EBM and SLM. EDM improved the fatigue performance, but still did not compare to the wrought titanium properties. Internal porosity was not observed and all fatigue crack initiations originated from rough features on either the as-built or machined surfaces. Facchini et al. [7] assessed the fatigue performance of Ti-6Al-4V specimens produced by EBM in the as-built and HIP'ed conditions. In the as-built condition, the fatigue life was similar to cast products and in the HIP'ed condition the fatigue strength became more comparable to wrought material. Brandl et al. [21,22] investigated the fatigue strength of wire deposited materials consolidated with both laser and arc heat sources. While there were low performing outliers due to near surface porosity, the fatigue strength was comparable to wrought material, ranging from 760 to 780 MPa in the as-built conditions to 840 MPa after heat treatment.

Even though several studies have been conducted on the fatigue performance of AM Ti-6Al-4V materials, there is still a need to generate more data in this area. Additionally, there is very limited information available on damage tolerance properties, such as fracture toughness and fatigue crack growth propagation. Furthermore, and more importantly, while specimen testing can provide insight into the expected performance of full-scale components, in fatigue, test coupon data is only good at estimating the life of test coupons [27]. When using fatigue properties derived from coupon testing for estimating the life of other structures, a life estimate within a factor of 2 would be exceptional and even one within an order of magnitude would not be considered abnormal. Life estimates of structures made from coupon test data should be verified by testing the actual structure, or component, of interest. Therefore, in this research, a typical aerospace component was built by AM and subjected to its design loads to validate the fatigue life trends developed by coupon testing.

Additionally, while using AM to minimize part weight is a primary motivation, manufacturing costs, and environmental impacts, must also be minimized. Post processing of AM parts, such as heat treatment, machining, and peening can all potentially improve part performance, but add to the total manufacturing cost and increase the net carbon footprint for the part. Thus, this study will also evaluate the effect of machining and peening on fatigue performance to try and gain an understanding of the cost versus benefit trade off for post processing AM titanium parts. Heat treatment was not used in this research since the AM process used, EBM, is conducted in a high temperature build chamber that effectively stress relieves the parts during build. Metallography, static properties, residual stress, fracture toughness, and crack growth behavior were also evaluated.

2 Experimental Setup and Procedure

All test specimens and parts were produced by EBM on an ARCAM A1 machine [24]. This machine builds up components by selectively melting layers, 700 μm in thickness, of titanium powder using an electron beam with power ranging from 50 to 3500 W with a spot size of 0.2–1.0 mm and a beam speed of 3 m/s. All processing was done in a vacuum chamber ($<1 \times 10^{-4}$ bar) at elevated temperature (700 °C) to minimize residual stresses during solidification and cooling of the melted layers. The exact processing

parameters were identified by the Boeing Company via a trial-and-error basis starting from the machine manufacturers recommended conditions to achieve optimal results. However, these exact processing conditions remain proprietary. The titanium powder material used in this study was a Ti-6Al-4V powder produced by plasma rotation electrode process (PREP). This produces powder with a spherical shape ranging between 100 and 300 μm in size.

Since parts are made in an elevated temperature build chamber to minimize residual stresses, specimens were not heat treated after depositing. While heat treating, either stress relief or hot isostatic pressing, after deposition could further stress relieve the parts and/or consolidate the materials, it was desired to test the specimens in the as-deposited condition since post processing such as this would add cost to the manufacturing process that may make AM cost prohibitive. Residual stress measurements would be made to ensure adequate levels of residual stresses were being achieved without post build heat treatment.

A variety of specimens were produced on the ARCAM machine for this study. At this point it is important to define the orientation of the specimens built. The base, horizontal plane, of the build chamber can be defined as the *x* and *y* directions of a Cartesian coordinate system, Fig. 2. The depth, or vertical dimension, of the build chamber is then in the *z* direction. With the ARCAM machine, the beam traverse direction rotates 90 deg with respect to the beam traversing direction after every layer. This negates any build orientation directional differences between the two horizontal directions, *x* and *y*, of the build chamber. Thus, rather than needing to build specimens in both the *x* and *y* directions to determine potential property variations due to orientation, only one set of horizontal specimens would be needed. Specimens built in the vertical, *z* direction would still be needed for comparison to those built in the horizontal directions.

Small cubes were built for metallographic analysis. These cubes were 10 mm × 10 mm × 10 mm in size. Samples were sectioned and mounted so that the microstructure of the materials could be examined with respect to all three build orientation directions, normal to the *x-y*, *y-z*, and *z-x* planes. After mounting, specimens were polished, etched, and photographed under high magnification. This metallographic analysis would provide insight into the build process and resulting mechanical properties.

Since it is desired to minimize manufacturing costs by avoiding a post build heat treatment and rely solely on the elevated build chamber temperatures to minimize residual stresses, it is necessary to measure the resulting as-built residual stresses. A 100 mm × 100 mm part in the horizontal plane of the build chamber was made with a thickness of 12 mm in the vertical direction. Residual stress measurements were made at the center of these samples on both the top and bottom sides at nominal depths of 13, 25, 51, 76, 127, 178, and 254 × 10⁻³ mm using X-ray diffraction in accordance with SAE HS-784.

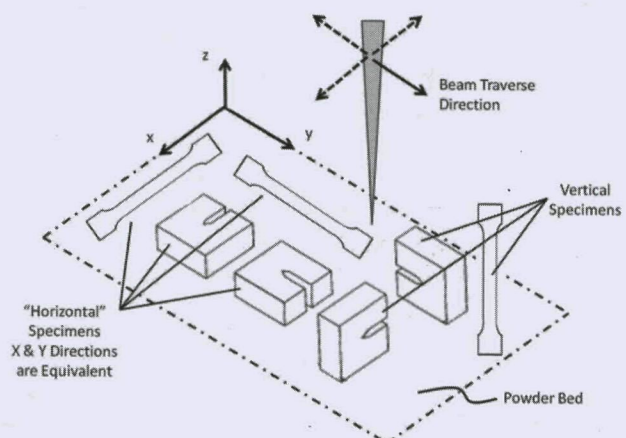


Fig. 2 Schematic of specimen orientation in machine

In this study 10 tensile specimens, were built to net shape, meaning no post process machining would be performed. Half were made in the horizontal orientation where the length and width directions of the specimens corresponded to the x and y directions of the build chamber with the thickness direction of the specimen in the vertical direction of the chamber. The other half of the specimens were built in the vertical direction, with the lengthwise direction of the specimens being in the vertical, z, direction of the chamber. All specimen dimensions (flat bar) and test conditions were in accordance with ASTM E 8. The overall dimensions of the tensile specimens produced were 200 mm in length, 20 mm wide, and 6 mm thick. In each test, the yield and ultimate strengths were recorded in addition to the elongation to failure. A clip on extensometer was used to measure elongation of the specimen gage section through failure.

Fracture toughness compact tension, (CT), specimens were fabricated per ASTM E 399 with $B = 40$ mm and $W = 80$ mm. 100 mm \times 100 mm \times 50 mm blocks were deposited and the CT specimens were then machined to net dimensions as opposed to building the CT specimens with the notch and loading pin holes directly during the AM process so that critical specimen dimensions could be controlled closely by precision machining. Five specimens were built in both the horizontal and vertical orientations, where the loading direction of the CT specimen corresponds to the indicated build orientation. The crack is then perpendicular to the specified build orientation.

Fatigue crack growth tests were performed per ASTM E647. For this test a standard CT specimen was used with the dimensions $W = 101.6$ mm and $B = 19.05$ mm. 125 mm \times 125 mm \times 25 mm blocks were deposited and then machined to the net specimen. Paris Law Region II testing was performed at a frequency of 10 Hz and a load ratio of $R = 0.1$ at constant load amplitude (increasing ΔK). Electric potential drop method was used to monitor the crack growth and the crack length measurement was verified using periodic optical measurements. Five specimens were built in both the horizontal and vertical orientations, where the loading direction of the CT specimen corresponds to the indicated build orientation. The crack is then perpendicular to the specified build orientation.

High cycle fatigue (HCF) specimens were made in a wide variety of conditions. Flat bar, low K_t (1.0), fatigue specimens were made in the vertical and horizontal orientations of the build chamber. Specimens were built via AM directly to net dimensions as well as machined to net dimensions from 250 mm long \times 40 mm wide \times 8 mm thick bars produced by AM to assess the difference in as-built surface finish and a machined finish. The final overall dimensions of the fatigue specimens were 200 mm long \times 30 mm wide \times 6 mm thick. Furthermore, in many fatigue critical applications titanium components are peened to induce compressive residual stresses at the surface and suppress fatigue crack initiation. Thus, some of the fatigue specimens machined to the net shape were also peened with 0.006 A intensity and 100% coverage. Five samples were made in each condition (as-built, machined, machined & peened) and orientation (horizontal and vertical) combination. Each specimen was tested at different constant maximum stress level, from 100 to 600 MPa, to failure in order to generate a rough S-N curve for that given condition/orientation. Testing of the samples was carried out per ASTM E466-07 at a frequency of 20 Hz and a load ratio of $R = -0.2$.

Typical bracket type parts were selected to be built and tested in fatigue to validate the results of the specimen tests for this study. Components were tested in both the as-built and machined conditions. Figure 3 shows the as-built part tested along with a component that was deposited with excess and subsequently machined to the net shape dimensions. Testing of the weight optimized design, Fig. 1(b), was not included in this particular study.

After fabrication, these test components were then drilled and fastened to a fixture, Fig. 4, designed to mimic the design loads for this component. Design loads and fastener requirements were provided by the project sponsor, but details remain proprietary.

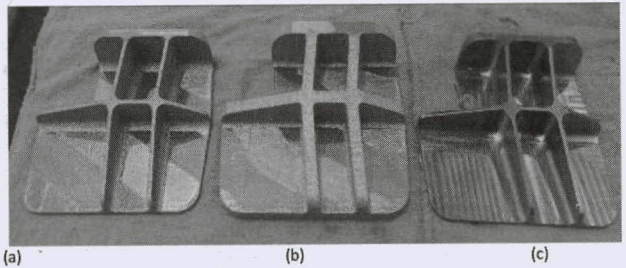


Fig. 3 Ti-6Al-4V egg crate/bracket prototype parts. (a) As-deposited, (b) deposited with excess, and (c) machined.

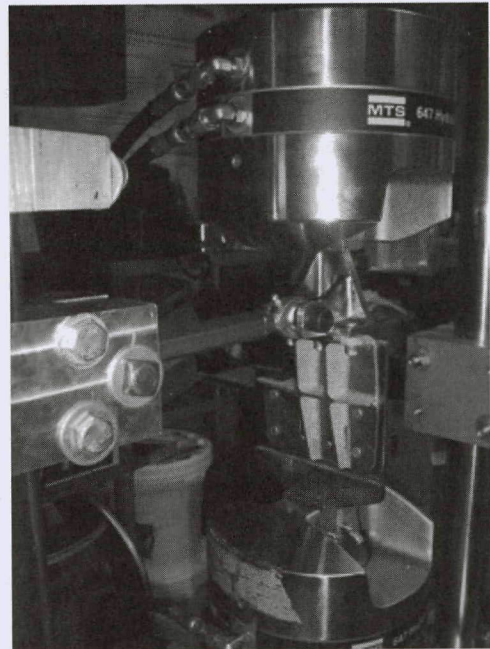


Fig. 4 Component fatigue test setup

All components were subjected to the design loads at a load ratio of $R = -0.39$ for $2 \times$ lifetimes (defined as 500,000 cycles). If the components survived $2 \times$ lifetimes at the design loads, the load was doubled and the parts were cycled for another lifetime. If failure still had not occurred after the double design load phase, the parts were then statically loaded to failure. The tests were carried out at room temperature and at a 10 Hz frequency.

3 Results

A 3D metallographic image of the Ti-6Al-4V material produced by EBM and a higher magnification image of the y-z plane orientation microstructure are given in Fig. 5. As expected, a transformed beta structure is observed as a result of solidification from the molten state. A columnar, or epitaxial, prior beta grain structure is also seen. These columnar grains point upward, in the z-direction, in the build and the columnar grains are continuous across multiple build layers. It is expected that this directionally dependent microstructure will result in anisotropic mechanical properties. Some small porosity was also observed.

Figure 6 shows a cross section of an as-deposited sample at the surface. This clearly highlights the as-built surface condition, which would be expected to result in poor high cycle fatigue performance due to the roughness and large number of potential crack initiation sites. This rough surface will likely have to be machined away for any part that would be subjected to fatigue loading, which will add to manufacturing costs. Machining complex part shapes produced by AM could even result in higher costs

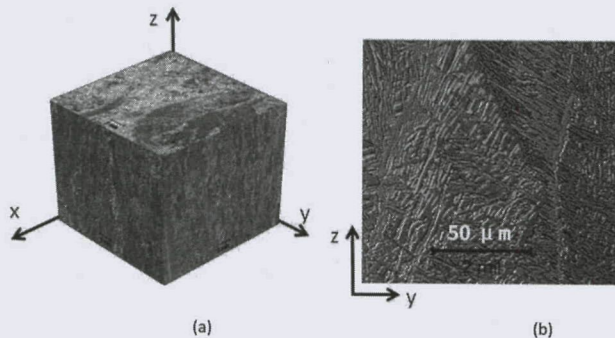


Fig. 5 (a) Microstructure cube and (b) high magnification microstructure of y-z plane

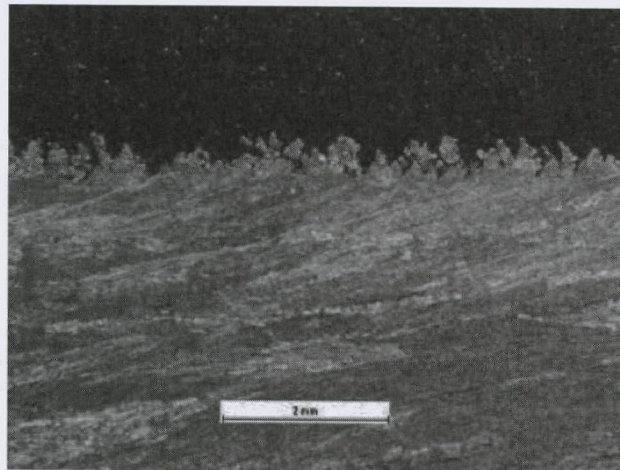


Fig. 6 Cross section at the surface of an ARCAM sample showing typical surface condition

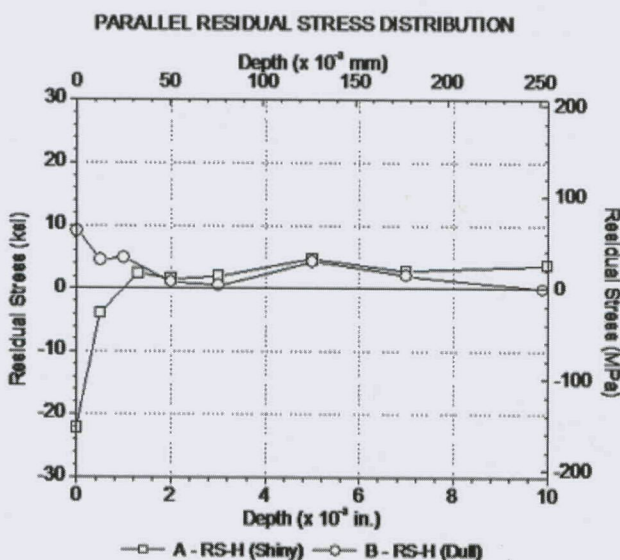


Fig. 7 Residual stress measurements in the x-direction as a function of depth taken from the top (a) and bottom (b) of EBM part

compared to machining from wrought material, unless the AM part geometry is so complex machining from wrought becomes impossible.

Residual stress measurements taken from the top and bottom of 100 mm × 100 mm × 12 mm thick specimens are given in Fig. 7.

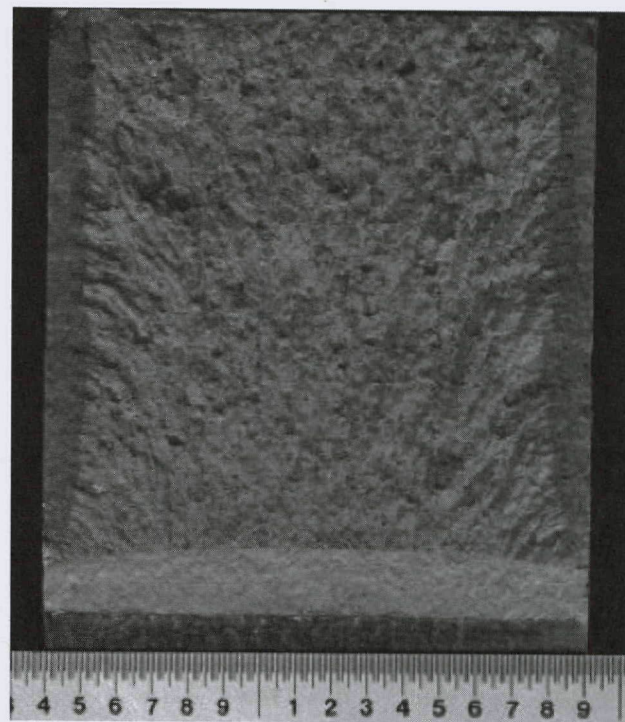


Fig. 8 Fracture toughness specimen fracture surface

These results show that there are compressive residual stresses at the bottom of the sample and tensile stresses on the top of the part. Compressive residual stresses would be beneficial in fatigue while tensile stresses would be detrimental. After approximately 0.03 mm into the specimen, on both sides, the residual stresses reduce to nearly zero. Thus, for parts that are machined, residual stress should have a negligible effect on performance. This illustrates that the elevated build temperature used in the EBM process is effective at minimizing residual stresses and avoiding a mandatory post build stress relief.

Tensile properties for the specimens built in the horizontal and vertical orientations are given in Table 1. Both average values and standard deviations are given for the limited number of tensile specimens tested. In both orientations, the strength and elongations are lower than handbook values for wrought Ti-6Al-4V [25].

3.1 Fracture Toughness. The apparent fracture toughness values for both the horizontal and vertical orientations are given in Table 2. Values are given for both the average and standard deviation for the population of specimens tested in each

Table 1 Tensile properties

Orientation	UTS (MPa)		0.2% YS (MPa)		Elong %	
	Ave	Stdev	Ave	Stdev	Ave	Stdev
Horizontal	833	22	783	15	2.7	0.4
Vertical	851	19	812	12	3.6	0.9

Table 2 Fracture toughness properties

Orientation	Kq (MPa \sqrt{m})	
	Ave	Stdev
Horizontal	110	8.9
Vertical	102	7.4

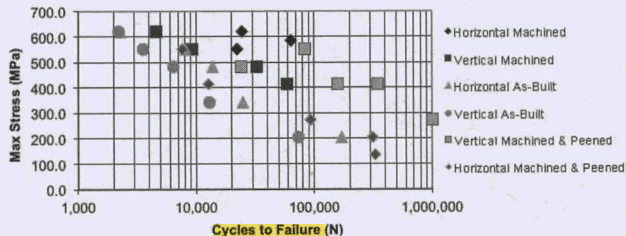


Fig. 9 Fatigue results $R = -0.2$, $K_t = 1.0$

orientation. For annealed Ti-6Al-4V, the fracture toughness is on the order of $66 \text{ MPa}\sqrt{\text{m}}$ [25], thus these AM parts have superior fracture toughness. This is likely related to the coarse grained acicular alpha microstructure when compared to standard Ti-6Al-4V plate fine equiaxed structure. Apparent fracture toughness (K_q ($\text{MPa}\sqrt{\text{m}}$)) is reported as opposed to K_{ic} due to a failed specimen geometry validity check. Predicating the correct fracture toughness specimen size is difficult as it depends on the yield strength. These tests resulted in higher fracture toughness and lower strengths than expected, which led to the invalid result. Thicker specimens ($W = 120 \text{ mm}$ and $B = 60 \text{ mm}$) would likely be needed for a valid result.

A typical fracture surface is given in Fig. 8. Some porosity was observed on this fracture surface. While small porosity is not expected to have a large influence on the fracture toughness, it will be an issue in fatigue.

3.2 High Cycle Fatigue. The results of the fatigue testing are shown in Fig. 9 on a plot of maximum applied stress versus number of cycles to failure. Two specimen build orientations, vertical and horizontal, are given along with three different conditions, as-built, machined and machined then peened. Compared to wrought Ti-6Al-4V, which has a fatigue strength of approximately 750 MPa at $100,000$ cycles [25] all build orientations and conditions have significantly lower fatigue strengths. Peening of the vertical build orientation specimens provided a noticeable improvement in fatigue strength at higher cycles, but this improvement was not seen on the horizontal peened specimens.

Fracture surface evaluation of the fatigue specimens in the as-deposited (net), machined and peened conditions for both build orientations are given in Fig. 10. The net specimens highlight the rough as-built surface finish that leads to multisite crack initiation and virtually no stable crack growth behavior before final fracture. In the machined condition, internal porosity was brought to the surface during machining, which then acted as the crack initiation

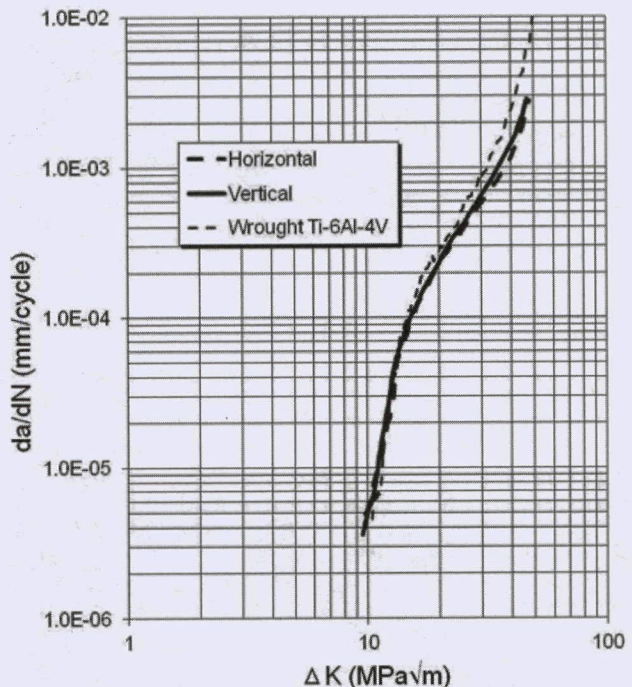


Fig. 11 Fatigue crack growth rate results $R = 0.1$

site instead of the rough surface finish. This is why no significant difference was observed between the as-deposited and machined conditions. By peening, the induced compressive residual stresses drove crack initiation to a sub-surface porosity defect for the vertical build specimens. However, for the horizontal specimen, it appears that a crack still initiated at near surface porosity.

3.3 Crack Growth. Fatigue crack growth curves for the Horizontal and Vertical orientation specimens are given in Fig. 11 along with base metal data obtained from a previous study [26] for comparison. The AM specimens in both orientations displayed essentially equivalent behavior with respect to each other. This indicates that there is no noticeable difference in crack growth rates as a function of specimen, crack, or loading orientation. Compared to wrought material, the additive parts behave similarly in the Region I, the threshold region. However, in Region II, the Paris Law Region, the additive curves deviate slightly from the wrought curve. The additive materials actually exhibit slower

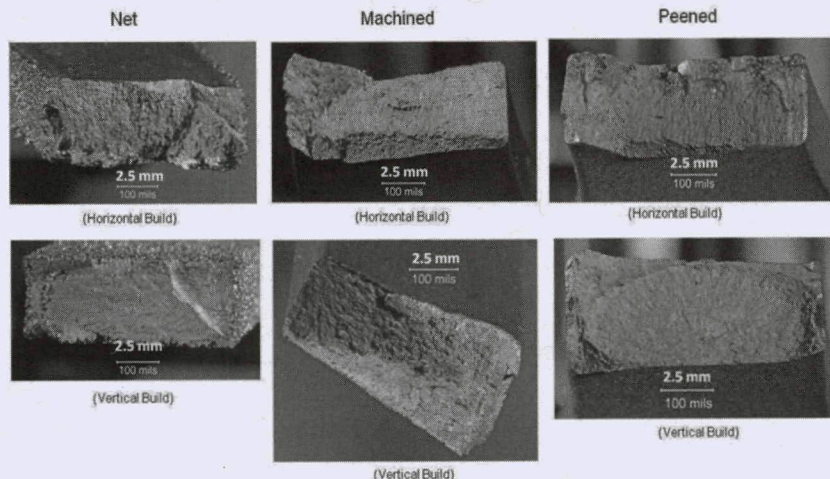


Fig. 10 ARCAM fatigue specimen fracture surfaces

crack growth rates for a given ΔK in Region II and as the crack/load combinations, or ΔK , approach the point of instability and eventual fracture in Region III.

In the component testing of both the net shape and fully machined conditions, no parts failed at the design load before two lifetimes (500,000 cycles) were reached. When loads were doubled and the parts were cycled for another lifetime (250,000 cycles), they either still did not fail or failure occurred in the fasteners, Fig. 12. In one of the net shape parts, a fastener failed at 177 k cycles in the double design loading phase. This fastener was replaced and testing continued, but this same fastener failed again after an additional 32 k cycles. This fastener was replaced two more times, lasting 26 k and 19 k cycles each time, respectively. At this point, it was noticed that a crack had begun to form at this fastener hole, Fig. 12(b), and the testing was stopped. This was the only component tested where any kind of part failure was observed. It is expected that the number of cycles the replaced fastener lasted continued to decrease because the crack at the hole was growing throughout this process, which allowed the part to become more compliant and lead to more and more deflection of the fastener as the testing continued and the crack grew.

Several of the parts, both net and machined, which survived both the single and double design load testing for a total of three lifetimes (750,000 cycles) with no fastener failures, were then subjected to monotonic static loading to failure. In all of these static tests, failure occurred in the fasteners and not the parts. This component testing, both fatigue and static, suggest that even though the performance of Ti-6Al-4V AM materials was found to be lower than wrought material via specimen testing, fasteners are more susceptible to failure in structural component testing than the actual AM parts.

4 Discussion

The primary focus of this study was to evaluate the fatigue performance of Ti-6Al-4V materials produced by additive manufacturing with standard test specimens and to validate the applicability of the results to the fatigue performance of actual components. It was found that fatigue performance of the Ti-6Al-4V specimens was significantly reduced, on the order of 80%, compared to wrought material regardless of the condition (net, machined, and peened). In previously published research [7,8,20–22], it was found that the fatigue performance of Ti-6Al-4V AM materials could be equivalent to wrought material when porosity is avoided, the rough as-built surface condition is removed and, in the case of non EBM process, heat-treated. For this study, the fatigue life was limited by the rough surface in the net condition and then the sub-surface porosity in the machined and peened conditions. Peening was shown to improve the fatigue life in some specimens, but porosity defects present generally negated any benefit provided by peening in this set of experiments. If the porosity could be eliminated and the surfaces

machined, it is expected that the fatigue performance would increase to similar levels as seen by previous researchers.

The tensile properties (strength and elongation) reported here were lower than handbook values [25,27] for wrought material and other published studies [3,12,20] on the static properties of AM Ti materials. However, in this case, all tensile specimens were tested in the as-deposited condition. There was no post process machining, stress relief or HIP. In most all of the previous studies [3,10–14] tensile specimens were machined prior to testing. It is possible that the porosity, as-deposited surface finish and residual stresses may have all contributed to this difference. This highlights the importance of testing specimens in the same condition that parts will be used in. If it is desired to use AM parts in the as-built state to minimize weight and cost, tensile data from fully machined specimens could be misleading.

The fracture toughness of the AM materials tested in this study was consistent and/or superior to handbook values of $44\text{--}66 \text{ MPa m}^{0.5}$ for wrought and $88\text{--}110 \text{ MPa m}^{0.5}$ for transformed (cast type) Ti-6Al-4V [27,25]. This is attributed to the large, coarse grained, microstructure of the AM materials compared to the fine, equiaxed (wrought) material. With respect to crack growth, the AM materials had equivalent Region I and slightly improved Region II da/dN behavior compared to wrought material. The fatigue crack growth results obtained are consistent with that of the data on cast versus wrought titanium alloys published in Ref. 25 [p. 565]. Thus, for fracture and damage tolerant driven designs, AM appears to be a viable candidate manufacturing process. It should be noted that the porosity defects that degraded the fatigue properties had no noticeable effect on the fracture toughness or crack growth behavior.

This study also evaluated the microstructure and residual stress in Ti-6Al-4V AM materials. The observed microstructure was consistent with previous studies [12,13], consisting of columnar prior beta grains containing lamellar alpha laths that span multiple build layers. The directionality of the microstructure was expected to result in anisotropic material behavior. However, static strengths were less than 4% different between the horizontal and vertical direction. The elongation difference between these two directions was 25%, but this only corresponded to a 1% difference in measured elongation. For fracture toughness, there was a 7% difference between the two build orientations. There was no quantifiable difference between the build orientations seen in the fatigue or crack growth testing. Overall, the differences in properties with build orientation did not appear to be significant, but only a limited number of specimens were tested, so more tests would be required to obtain a more statistically meaningful comparison. Moreover, additional testing is required to provide statistically meaningful to all of the results presented here.

Residual stress measurements showed that there were small amounts of compressive and tensile residual stresses on as-deposited parts, but the depths of these stresses were shallow. After approximately $760 \mu\text{m}$ the residual stresses essentially went

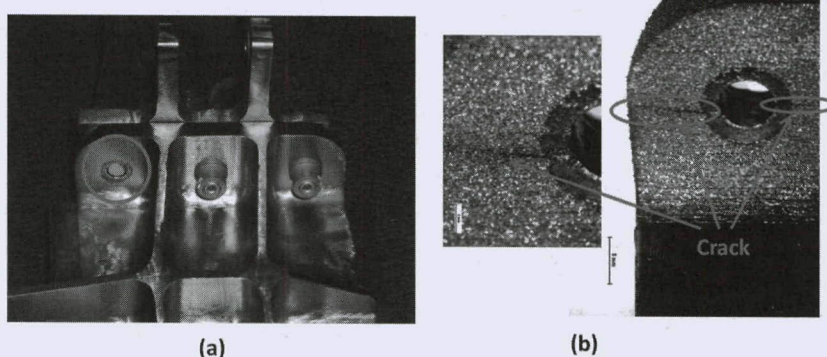


Fig. 12 (a) Location of repeat fastener failure and (b) crack initiated under the failed fastener

to zero. Post deposition machining of the part surface would remove these surface stresses. In the as-deposited net condition the rough surface finish likely overshadowed any tensile residual stress effects. These residual stress results support the conclusion that the elevated build temperature chamber used during fabrication of these parts using the EBM process is sufficient in minimizing residual stresses. However, for AM processes that do not use an elevated build chamber temperature, residual stresses will likely be higher and require post deposition heat treatment for stress relief. Stress relief or HIP'ing may also still be needed for EBM parts to reduce porosity and modifying the microstructure to improve mechanical performance.

Even though the fatigue performance of the specimens was inferior to wrought material and, would therefore, not likely be considered for use in the fabrication of fatigue critical components, the fatigue testing of parts, both net and machined, always resulted in fastener failure before part failure. This demonstrates that using AM, or any novel process, for the fabrication of fatigue driven components shouldn't be dismissed based solely on specimen test data. An opportunity for future research would be to test a part that has been optimized for weight based on the geometric build capabilities of AM. This was not possible due to logistical constraints for this particular program.

5 Conclusions

For the Ti-6Al-4V specimens and parts produced in this study by the Electron Beam Melting Additive Manufacturing process, it was found that:

- Fracture toughness and fatigue crack growth were comparable to literature properties of wrought Ti-6Al-4V.
- Residual stresses are low due to the elevated temperature in the build chamber, which minimizes temperature gradients during local melting and solidification. Thus, post process stress relief heat treatment is not required.
- The fatigue performance was significantly lower than handbook values for wrought Ti-6Al-4V. The rough surface finish in the as-deposited net condition and porosity in the machined conditions led to the premature failures. Peening provided little benefit.
- Structural components tested under design loads, and even double the design loads, for multiple design lifetimes, did not result in the premature failures expected based on coupon testing results. This shows that for fatigue driven designs, decisions should not be made solely on coupon data and structural element testing is needed to determine if a process such as this is acceptable for a given application.

Acknowledgment

The authors of this paper would like to thank Dr. Richard Hague, Dr. Chris Tuck and everyone else who contributed to this work from the Additive Manufacturing and 3D Printing Research Group at the University of Nottingham as well as the United Kingdom's Technology Strategy Board and The Boeing Company for their support.

References

- [1] Kruth, J. P., Leu, M. C., and Nakagawa, T., 1998, "Progress in Additive Manufacturing and Rapid Prototyping," *CIRP Ann.*, **47**(2), pp. 525–540.
- [2] Levy, G. N., Schindel, R., and Kruth, J. P., 2003, "Rapid Manufacturing and Rapid Tooling With Layer Manufacturing (LM) Technologies, State of the Art and Future Perspectives," *CIRP Ann.*, **52**(2), pp. 589–609.
- [3] Murr, L. E., Esquivel, E. V., Quinones, S. A., Gaytan, S. M., Lopez, M. I., Martinez, E. Y., Medina, F., Hernandez, D. H., Martinez, E., Martinez, J. L., Stafford, S. W., Brown, D. K., Hoppe, T., Meyers, W., Lindhe, U., and Wicker, R. B., 2009, "Microstructures and Mechanical Properties of Electron Beam-Melted Ti-6Al-4V Biomedical Prototypes Compared to Wrought Ti-6Al-4V," *Mater. Charact.*, **60**, pp. 96–105.
- [4] Murr, L. E., Gaytan, S. M., Ceylan, A., Martinez, E., Martinez, J. L., Hernandez, D. H., Machado, B. I., Ramirez, D. A., Medina, F., Collins, S., and Wicker, R. B., 2010, "Characterization of Titanium Aluminide Alloy Components Fabricated by Additive Manufacturing Using Electron Beam Melting," *Acta Mater.*, **58**(5), pp. 1887–1894.
- [5] Hrabe, N., and Quinn, T., 2013, "Effects of Processing on Microstructure and Mechanical Properties of a Titanium Alloy (Ti-6Al-4V) Fabricated Using Electron Beam Melting (EBM), Part 1: Distance From Build Plate and Part Size," *Mater. Sci. Eng. A*, **537**, pp. 264–270.
- [6] Hrabe, N., and Quinn, T., 2013, "Effects of Processing on Microstructure and Mechanical Properties of a Titanium Alloy (Ti-6Al-4V) Fabricated Using Electron Beam Melting (EBM), Part 2: Energy Input, Orientation, and Location," *Mater. Sci. Eng. A*, **537**, pp. 271–277.
- [7] Facchini, L., Magalini, E., Robotti, P., and Molinari, A., 2009, "Microstructure and Mechanical Properties of Ti-6Al-4V Produced by Electron Beam Melting of Pre-Alloyed Powders," *Rapid Prototyping J.*, **15**(3), pp. 171–178.
- [8] Chan, K., Koike, M., Mason, R., and Okabe, T., 2013, "Fatigue Life of Titanium Alloys Fabricated by Additive Manufacturing Techniques for Dental Implants," *Metall. Mater. Trans. A*, **44**A, pp. 1010–1022.
- [9] Harrysson, O., Deaton, B., Bardin, J., West, H., Cansizoglu, O., Cormier, D., and Little, D. M., 2005, "Evaluation of Titanium Implant Components Directly Fabricated Through Electron Beam Melting Technology," *Adv. Mater. Process.*, **163**(7), pp. 72–77.
- [10] Parthasarathy, J., Starly, B., Raman, S., and Christensen, A., 2010, "Mechanical Evaluation of Porous Titanium (Ti6Al4V) Structures With Electron Beam Melting (EBM)," *J. Mech. Behav. Biomed. Mater.*, **3**, pp. 249–259.
- [11] Heinl, P., Rottmair, A., Körner, A., and Singer, R. F., 2007, "Cellular Titanium by Selective Electron Beam Melting," *Adv. Eng. Mater.*, **9**(5), pp. 360–364.
- [12] Koike, M., Greer, P., Owen, K., Lilly, G., Murr, L., Gaytan, S., Martinez, E., and Okabe, T., 2011, "Evaluation of Titanium Alloys Fabricated Using Rapid Prototyping Technologies—Electron Beam Melting and Laser Beam Melting," *Materials*, **4**, pp. 1776–1792.
- [13] Thijs, L., Verhaeghe, F., Craeghs, T., Humbeeck, J., and Kruth, J., 2010, "A Study of the Microstructural Evolution During Selective Laser Melting of Ti-6Al-4V," *Acta Mater.*, **58**, pp. 3303–3312.
- [14] Facchini, L., Magalini, E., Robotti, P., Molinari, A., Hoeges, S., and Wissenbach, K., 2010, "Ductility of a Ti-6 Al-4 V Alloy Produced by Selective Laser Melting of Prealloyed Powders," *Rapid Prototyping J.*, **16**, pp. 450–459.
- [15] Kobry, P., Moore, E., and Semiatin, S., 2000, "The Effect of Laser Power and Traverse Speed on Microstructure, Porosity, and Build Height in Laser-Deposited Ti-6Al-4V," *Scr. Mater.*, **43**, pp. 299–305.
- [16] Kobry, P., and Semiatin, S., 2001, "The Laser Additive Manufacture of Ti-6Al-4V," *JOM*, **53**, pp. 40–42.
- [17] Kelly, S., and Kampe, S., 2004, "Microstructural Evolution in Laser-Deposited Multilayer Ti-6Al-4V Builds: Part I. Microstructural Characterization," *Metall. Mater. Trans. A*, **35**, pp. 1861–1867.
- [18] Mercelis, P., and Kruth, J., 2006, "Residual Stresses in Selective Laser Sintering and Selective Laser Melting," *Rapid Prototyping J.*, **12**, pp. 254–265.
- [19] Shiomi, M., Osakada, K., Nakamura, K., Yamashita, T., and Abe, F., 2004, "Residual Stress Within Metallic Model Made by Selective Laser Melting Process," *CIRP Ann.*, **53**(1), pp. 195–198.
- [20] Leuders, S., Thone, M., Riemer, A., Niendorf, T., Troster, T., Richard, H., and Maier, J., 2013, "On the Mechanical Behavior of Titanium Alloy TiAl6V4 Manufacture by Selective Laser Melting: Fatigue Resistance and Crack Growth Performance," *Int. J. Fatigue*, **48**, pp. 300–307.
- [21] Baufeld, B., Brandl, E., and Biest, O., 2011, "Wire Based Additive Layer Manufacturing: Comparison of Microstructural and Mechanical Properties of Ti-6Al-4 V Components Fabricated by Laser-Beam Deposition and Shaped Metal Deposition," *J. Mater. Process. Technol.*, **211**, pp. 1146–1158.
- [22] Brandl, E., Baufeld, B., Leynes, C., and Gault, R., 2010, "Additive Manufactured Ti-6Al-4V Using Welding Wire: Comparisons of Laser and Arc Beam Deposition and Evaluation With Respect to Aerospace Material Specifications," *Phys. Procedia*, **5**, pp. 595–606.
- [23] Santos, E. C., Osakada, K., Shiomi, M., Kitamura, Y., and Abe, F., 2004, "Microstructure and Mechanical Properties of Pure Titanium Models Fabricated by Selective Laser Melting," *Proc. Inst. Mech. Eng., Part C: J. Mech. Eng. Sci.*, **218**(7), pp. 711–719.
- [24] Arcam AB, "The Future in Implant Manufacturing," <http://www.arcam.com/wp-content/uploads/Arcam-A1.pdf>
- [25] Boyer, R., Welsch, G., and Collings, E. W., 1994, *Materials and Properties Handbook Titanium Alloys*, ASM International, Materials Park, OH, pp. 517–548.
- [26] Edwards, P., Petersen, M., Ramulu, M., and Boyer, R., 2010, "Mechanical Performance of Heat Treated Ti-6Al-4V Friction Stir Welds," *Key Eng. Mater.*, **436**, pp. 213–221.
- [27] Cameron, D. W., and Hoepfner, D. W., 1996, "Fatigue Properties in Engineering," *ASM Handbook: Fatigue and Fracture*, ASM International, Materials Park, OH, Vol. 19, p. 15.

Copyright of Journal of Manufacturing Science & Engineering is the property of American Society of Mechanical Engineers and its content may not be copied or emailed to multiple sites or posted to a listserv without the copyright holder's express written permission. However, users may print, download, or email articles for individual use.



LaserForm® 17-4PH (B)

for ProX® DMP 100, 200 and 300 Direct Metal Printers

General purpose metal powder with high strength, good corrosion resistance and thermal properties.

Chemical Composition

LaserForm 17-4PH (B)

ELEMENT	% OF WEIGHT
Fe	Balance
Cr	15 - 17.5
Ni	3 - 5
Cu	3 - 5
Si	< 1.0
Mn	< 1.0
Nb	0.15 - 0.45

Mechanical Properties¹

	CONDITION	AS-BUILT ²	AFTER POST HEAT TREATMENT ³
Ultimate Tensile Strength, MPa	ASTM E8	1100 ± 50	1300 ± 50
Yield Strength, MPa	ASTM E8	620 ± 30	1100 ± 50
Elongation at break, %	ASTM E8	16 ± 2.0	10 ± 2.0
Hardness		300 ± 20 HV5	400 ± 20 HV5
Density			approx. 100%

¹ Parts built on a ProX DMP 200 Direct Metal Production Printer

² As-built refers to the state of components built on the ProX DMP 200 Direct Metal Printer before any post processing except removal from the build platform

³ Different post heat treatments might be applied for this type of alloy

Applications

Industrial grade prototypes, production parts or spare parts for:

- Aerospace
- Chemical and petrochemical industry
- Energy sector
- Surgical instruments
- High-wear components
- General metalworking

Features

- Outstanding combination of high strength and good corrosion resistance
- Excellent mechanical properties at elevated temperatures — up to 300 °C
- High hardness
- Good thermal properties



www.3dsystems.com

Warranty/Disclaimer: The performance characteristics of these products may vary according to product application, operating conditions, or with end use. 3D Systems makes no warranties of any type, express or implied, including, but not limited to, the warranties of merchantability or fitness for a particular use.

©2017 by 3D Systems, Inc. All rights reserved. Specifications subject to change without notice. 3D Systems, ProX and LaserForm are registered trademarks and the 3D Systems logo is a trademark of 3D Systems, Inc.



LaserForm® 17-4PH (A)

LaserForm 17-4PH (A) is fine-tuned for use with ProX® DMP 320 metal printer producing industrial parts with good corrosion resistance, high mechanical strength combined with excellent ductility. Mechanical properties of LaserForm 17-4PH (A) can be varied upon different heat treatments.

LaserForm 17-4PH (A) is formulated and fine-tuned specifically for 3D Systems DMP 320 metal 3D printers to deliver high part quality and consistent properties. The print parameter database that 3D Systems provides together with the material has been extensively developed, tested and optimized in 3D Systems' part production facilities that holds the unique expertise of printing 500,000 challenging metal production parts in a broad choice of materials year over year. And for your 24/7 production 3D Systems' thorough Supplier Quality Management System guarantees consistent, monitored material quality for reliable results.

Material Description

LaserForm 17-4PH (A) is known for its outstanding combination of excellent corrosion resistance and high strength with good toughness. These good mechanical properties and corrosion resistance are maintained at temperatures up to 316°C (600°F). With these characteristics, LaserForm 17-4PH (A) is ideal for surgical instruments (sterilizable), aerospace, chemical, petrochemical and general metalworking applications.

Classification

The chemical composition of LaserForm 17-4PH (A) corresponds to a stainless steel 17-4 PH alloy according to ASTM F899, A564, A693 and UNS S17400 specifications, and is indicated in the table below in wt%.

Mechanical Properties^{1,2,3}

MEASUREMENT	CONDITION	METRIC			U.S.		
		AS-BUILT	H900	H1150	AS-BUILT	H900	H1150
Ultimate strength (MPa ksi)	ASTM E8M						
Horizontal direction ⁴ - XY		NA	1450 ± 10	1180 ± 10	NA	210 ± 2	170 ± 2
Vertical direction ⁵ - Z		1100 ± 90	1380 ± 20	1080 ± 50	160 ± 13	200 ± 3	155 ± 8
Yield strength Rp0.2% (MPa ksi)	ASTM E8M						
Horizontal direction ⁴ - XY		NA	1280 ± 30	1130 ± 20	NA	185 ± 5	165 ± 3
Vertical direction ⁵ - Z		830 ± 110	1260 ± 100	1020 ± 170	120 ± 16	180 ± 15	145 ± 25
Elongation at break (%)	ASTM E8M						
Horizontal direction ⁴ - XY		NA	11 ± 1	12 ± 1	NA	11 ± 1	12 ± 1
Vertical direction ⁵ - Z		19 ± 4	12 ± 2	16 ± 4	19 ± 4	12 ± 2	16 ± 4
Hardness, Rockwell C	ASTM E18	32 ± 4	40 ± 2	35 ± 3	32 ± 4	40 ± 2	35 ± 3
Impact toughness ⁶ (J ft-lb)	ASTM E23	71 ± 20	7 ± 2	11 ± 5	52 ± 15	5 ± 2	8 ± 4

Thermal Properties⁷

MEASUREMENT	CONDITION	METRIC	U.S.
Thermal conductivity (W/(m.K) Btu/(h.ft².°F))	at 100°C / 212 °F	18.3	10.6
CTE - Coefficient of thermal expansion (µm/ (m.°C) µ inch/(inch. °F))	at 0°C	11.6	6.4
Melting range (°C °F)		1400 - 1450	2550 - 2640

¹ Parts manufactured with standard parameters on a ProX DMP 320, Config B

² Values based on average and double standard deviation

³ H900 and H1150 indicate heat treatments targeting resp. H900 and H1150 conditions

⁴ Tested on ASTM E8M specimen with rectangular cross sections

⁵ Tested on ASTM E8M specimen with circular cross sections type 4

⁶ Tested with Charpy V-notch impact test specimens type A at room temperature

⁷ Values based on literature

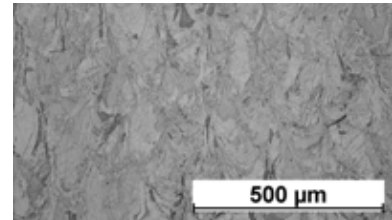
NA = Not available



LaserForm® 17-4PH (A)

Magnetic Properties¹

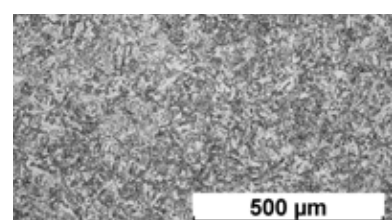
MEASUREMENT	METRIC	U.S.
Relative magnetic permeability	100	100



Microstructure as built

Physical Properties

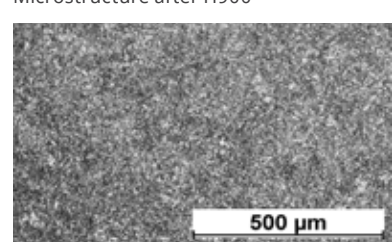
MEASUREMENT	METRIC	U.S.
Density		
Relative, based on pixel count ² (%)	>99.9	>99.9
Absolute theoretical ¹ (g/cm ³ lb/in ³)	7.75	0.28



Microstructure after H900

Surface Quality²

MEASUREMENT	METRIC		U.S.	
	AS BUILT	SAND BLASTED	AS BUILT	SAND BLASTED
Surface Roughness R _a				
Horizontal direction (XY) (μm μin)	5 - 7	4 - 7	195 - 275	155 - 275
Vertical direction (Z) (μm μin)	6 - 8	4 - 8	236 - 315	155 - 315



Microstructure after H1150

Chemical Composition

ELEMENT	% OF WEIGHT
Fe	Bal.
C	<0.07
Mn	<1.00
P	<0.040
S	<0.030
Si	<1.00
Cr	15.00-17.50
Ni	3.00-5.00
Cu	3.00-5.00
Nb+Ta	0.15-0.45

¹ Values based on literature

² Parts manufactured with standard parameters on a ProX DMP 320, Config B



www.3dsystems.com

Warranty/Disclaimer: The performance characteristics of these products may vary according to product application, operating conditions, or with end use. 3D Systems makes no warranties of any type, express or implied, including, but not limited to, the warranties of merchantability or fitness for a particular use.

©2017 by 3D Systems, Inc. All rights reserved. Specifications subject to change without notice. 3D Systems, ProX and LaserForm are registered trademarks and the 3D Systems logo is a trademark of 3D Systems, Inc.



LaserForm® 316L (A)

Extra low-carbon grade Stainless Steel which is fine-tuned for use with the ProX® DMP 320, producing parts with high corrosion resistance and sterilisability. LaserForm 316L (A) yields crack free and completely dense parts for all your applications.

LaserForm 316L (A) is formulated and fine-tuned specifically for 3D Systems DMP 320 metal 3D Printers to deliver highest part quality and best part properties. The print parameter database that 3D Systems provides together with the material has been extensively developed, tested and optimized in 3D Systems' part production facilities that hold the unique expertise of printing 500,000 challenging production parts year over year. Based on over 1000 test samples the below listed part quality data and mechanical properties give you high planning security. And for a 24/7 production 3D Systems' thorough Supplier Quality Management System guarantees consistent, monitored material quality for reliable process results.

Material Description

Austenitic stainless steel type LaserForm 316L is the extra low carbon grade of 316. This steel is used as a general purpose material with excellent mechanical and corrosion properties at room temperature. Its chloride resistance makes this specific grade of stainless steel suitable for marine applications. 316L stainless steel is also the preferred material for use in hydrogen atmospheres or for hydrogen piping / cooling applications. Furthermore 316L retains good mechanical properties at sub-zero and even cryogenic temperatures and is suitable for structural components in low-temperature applications.

Classification

Parts built with LaserForm 316L alloy have a chemical composition that conforms to the compositional requirements of DIN X2CrNiMo 17-12-2 or Werkstoff Nr. 1.4404.

Mechanical Properties^{1,3}

MEASUREMENT	CONDITION	METRIC		U.S.	
		AFTER STRESS RELIEF	FULL ANNEAL	AFTER STRESS RELIEF	FULL ANNEAL
Youngs modulus (GPa ksi)					
Horizontal direction — XY		180 ± 15	180 ± 15	27600 ± 1500	27600 ± 1500
Ultimate Strength (MPa ksi)	ASTM E8M				
Horizontal direction — XY		660 ± 20	610 ± 30	96 ± 3	89 ± 5
Vertical direction — Z		570 ± 30	540 ± 30	83 ± 5	78 ± 5
Yield strength Rp0.2% (MPa ksi)	ASTM E8M				
Horizontal direction — XY		530 ± 20	370 ± 30	77 ± 3	54 ± 5
Vertical direction — Z		440 ± 20	320 ± 20	63 ± 3	47 ± 3
Elongation at break (%)	ASTM E8M				
Horizontal direction — XY		39 ± 5	51 ± 5	39 ± 5	51 ± 5
Vertical direction — Z		49 ± 5	66 ± 5	49 ± 5	66 ± 5
Reduction of area (%)	ASTM E8M				
Horizontal direction — XY		65 ± 5	61 ± 5	65 ± 5	61 ± 5
Vertical direction — Z		65 ± 5	62 ± 5	65 ± 5	62 ± 5
Hardness, Rockwell B (HRB)	ASTM E18	90 ± 6	83 ± 4	90 ± 6	83 ± 4
Impact toughness ² (J/cm² lb.ft)	ASTM E23	215 ± 15	220 ± 15	158 ± 10	162 ± 10

Thermal Properties⁴

MEASUREMENT	CONDITION	METRIC	U.S.
Thermal conductivity (W/(m.K) Btu/(h.ft².°F))	At 20 °C/ 68 °F	15	9
Coefficient of Thermal Expansion (µm/m·°C µin/in·°F)	In the range of 20 - 600°C / 68-1112°F	19.0	10.6
Melting range (°C °F)		1370-1400	2500-2550

¹ Parts manufactured with standard parameters on a ProX DMP 320, Config B

² Tested with charpy V-notch toughness test, DMV probe

³ Values based on average and standard deviation

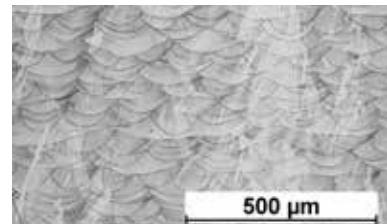
⁴ Values based on literature



LaserForm® 316L (A)

Physical Properties⁴

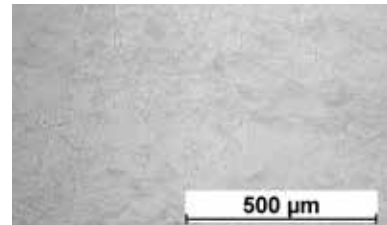
MEASUREMENT	METRIC		U.S.	
	AS BUILT AND AFTER STRESS RELIEF	AFTER FULL ANNEAL	AS BUILT AND AFTER STRESS RELIEF	AFTER FULL ANNEAL
Density — Absolute theoretical ⁵ (g/cm³ lb/in³)	8.0		0.286	



Microstructure after stress relief

Surface Quality

MEASUREMENT	METRIC		U.S.	
	SANDBLASTED	SANDBLASTED	SANDBLASTED	SANDBLASTED
Surface Roughness Vertical direction (Z) (μm μin)	5-10		200-400	



Microstructure after full anneal

Chemical Composition

ELEMENT	% OF WEIGHT
Fe	bal.
Cr	16.50-18.50
Ni	10.00-13.00
C	≤0.030
Mn	≤2.00
Mo	2.00-2.50
N	≤0.11
Si	≤1.00
P	≤0.045
S	≤0.030

 **3D SYSTEMS®**

www.3dsystems.com

Warranty/Disclaimer: The performance characteristics of these products may vary according to product application, operating conditions, or with end use. 3D Systems makes no warranties of any type, express or implied, including, but not limited to, the warranties of merchantability or fitness for a particular use.

©2017 by 3D Systems, Inc. All rights reserved. Specifications subject to change without notice. 3D Systems, ProX and LaserForm are registered trademarks and the 3D Systems logo is a trademark of 3D Systems, Inc.

⁴Values based on literature



LaserForm® CoCr (B)

Cobalt-chromium-molybdenum alloy fine-tuned for use with DMP Flex 100, ProX® DMP 200 and ProX® DMP 300 metal printers producing industrial parts with high corrosion and wear resistance that also require high temperature resistance.

LaserForm CoCr (B) is formulated and fine-tuned specifically for 3D Systems DMP Flex 100, ProX® DMP 200 and ProX® DMP 300 metal 3D printers to deliver high part quality and consistent part properties. The print parameter database that 3D Systems provides together with the material has been extensively developed, tested and optimized in 3D Systems' part production facilities that hold the unique expertise of printing 500,000 challenging metal production parts in various materials year over year. For a 24/7 production operation 3D Systems' thorough Supplier Quality Management System guarantees consistent, monitored material quality for reliable process results.

Material Description

Cobalt-chromium-molybdenum alloys are known for their high strength and hardness and retain these properties even at elevated temperatures. In addition, they spontaneously form a protective passive film, which makes LaserForm CoCr (B) both corrosion resistant and biocompatible.

These benefits make LaserForm CoCr (B) the ideal material for medical tools and devices, molds and dies, industrial, high wear applications and parts requiring high strength at elevated temperatures.

Classification

The chemical composition of LaserForm® CoCr (B) conforms to the requirements of the ASTM F75 and is indicated in the table below in % of weight.

Mechanical Properties^{1,2}

MEASUREMENT	CONDITION	METRIC		U.S.	
		AS-BUILT	AFTER SOLUTION ANNEAL	AS-BUILT	AFTER SOLUTION ANNEAL
Youngs modulus (GPa ksi)	ASTM E8M				
Horizontal direction - XY		220 ± 40	240 ± 40	31900 ± 5800	34800 ± 5800
Vertical direction - Z		170 ± 40	220 ± 40	24700 ± 5800	31900 ± 5800
Ultimate strength (MPa ksi)	ASTM E8M				
Horizontal direction - XY		1150 ± 80	1050 ± 50	165 ± 12	150 ± 7
Vertical direction - Z		1090 ± 40	1040 ± 50	160 ± 6	150 ± 7
Yield strength Rp0.2% (MPa ksi)	ASTM E8M				
Horizontal direction - XY		840 ± 80	590 ± 40	120 ± 12	85 ± 6
Vertical direction - Z		630 ± 40	570 ± 40	90 ± 6	85 ± 6
Elongation at break (%)	ASTM E8M				
Horizontal direction - XY		6 ± 2	33 ± 6	6 ± 2	33 ± 6
Vertical direction - Z		15 ± 4	35 ± 6	15 ± 4	35 ± 6
Reduction of area (%)	ASTM E8M				
Horizontal direction - XY		13 ± 8	31 ± 6	13 ± 8	31 ± 6
Vertical direction - Z		19 ± 8	32 ± 6	19 ± 8	32 ± 6
Hardness, Rockwell C	ASTM E18	32 ± 5	26 ± 5	32 ± 5	26 ± 5

¹ Parts manufactured with standard parameters on DMP Flex 100 and ProX® DMP 200

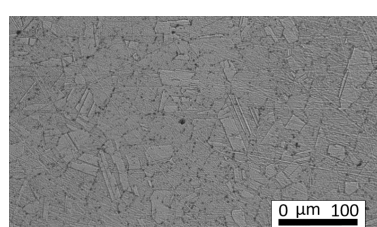
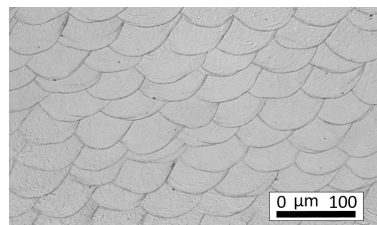
² Values based on average and double standard deviation



LaserForm® CoCr (B)

Thermal Properties¹

MEASUREMENT	CONDITION	METRIC	U.S.
Thermal conductivity (W/(m.K) Btu/(h.ft.°F))	at 20°C / 120 °F	14	8
CTE - Coefficient of thermal expansion (µm/(m.°C) µ inch/(inch . °F))	in the range of 20 to 600 °C	14	7.8
Melting range (°C °F)		1350 - 1430	2460 - 2610



Electrical Properties¹

MEASUREMENT	METRIC	U.S.
Electrical resistivity (µΩ.m µΩ.in)	0.87	34.41

Microstructure after solution anneal

Physical Properties

MEASUREMENT	METRIC	U.S.
	AS BUILT AND AFTER SOLUTION ANNEAL	AS BUILT AND AFTER SOLUTION ANNEAL
Density		
Relative, based on pixel count ² (%)	>99	
Absolute, theoretical ¹ (g/cm³ lb/in³)	8.30	0.300

Chemical Composition

ELEMENT	% OF WEIGHT
Co	Bal.
Cr	28.00-30.00
Mo	5.00-6.00
Ni	0.00-0.10
Fe	0.00-0.50
C	0.00-0.02
Si	0.00-1.00
Mn	0.00-1.00
Cd	0.00-0.02
Be	0.00-0.02
Pb	0.00-0.02

¹ Values based on literature

² Parts manufactured with standard parameters on a DMP Flex 100 and ProX® DMP 200



www.3dsystems.com

Warranty/Disclaimer: The performance characteristics of these products may vary according to product application, operating conditions, or with end use. 3D Systems makes no warranties of any type, express or implied, including, but not limited to, the warranties of merchantability or fitness for a particular use.

©2019 by 3D Systems, Inc. All rights reserved. Specifications subject to change without notice. 3D Systems, ProX and LaserForm are registered trademarks and the 3D Systems logo is a trademark of 3D Systems, Inc.



LaserForm® CoCrF75 (A)

Cobalt-chromium-molybdenum alloy fine-tuned for use with ProX DMP 320 metal printer producing industrial parts with high corrosion and wear resistance that also require high temperature resistance. In addition to various industrial applications, LaserForm CoCrF75 (A) is also suitable for medical applications.

LaserForm CoCrF75 (A) is formulated and fine-tuned specifically for 3D Systems DMP 320 metal 3D Printers to deliver high part quality and consistent part properties. The print parameter database that 3D Systems provides together with the material has been extensively developed, tested and optimized in 3D Systems' part production facilities that hold the unique expertise of printing 500,000 challenging metal production parts in various materials year over year. And for your 24/7 production 3D Systems' thorough Supplier Quality Management System guarantees consistent, monitored material quality for reliable results.

Material Description

Cobalt-chromium-molybdenum alloys are known for their high strength and hardness and retain these properties even at elevated temperatures. In addition, they spontaneously form a protective passive film, which makes LaserForm CoCrF75 (A) both corrosion resistant and biocompatible.

These benefits make LaserForm CoCr75 (A) the ideal material for medical tools and devices, molds and dies, industrial, high wear applications and parts requiring high strength at elevated temperatures. In biomedical applications, LaserForm CoCr75 (A) is ideal for dental implants and prostheses.

Classification

The chemical composition of LaserForm® CoCr F75 conforms to the requirements of the ASTM F75, ISO 5832 and ISO 22674 standards, and is indicated in the table below in wt%.

Mechanical Properties^{1,2,3}

MEASUREMENT	CONDITION	METRIC		U.S.	
		AFTER ANNEAL	AFTER HIP	AFTER ANNEAL	AFTER HIP
Youngs modulus (GPa ksi)	ASTM E8M	225 ± 5	225 ± 5	32650 ± 730	32650 ± 730
Ultimate strength (MPa ksi)	ASTM E8M				
Horizontal direction - XY		1030 ± 70	1020 ± 70	150 ± 10	150 ± 10
Vertical direction - Z		1000 ± 30	950 ± 40	145 ± 5	140 ± 5
Yield strength Rp0.2% (MPa ksi)	ASTM E8M				
Horizontal direction - XY		540 ± 30	510 ± 30	80 ± 5	75 ± 5
Vertical direction - Z		520 ± 30	475 ± 20	75 ± 5	70 ± 5
Elongation at break (%)	ASTM E8M				
Horizontal direction - XY		29 ± 6	29 ± 6	29 ± 6	29 ± 6
Vertical direction - Z		29 ± 4	23 ± 3	29 ± 4	23 ± 3
Hardness, Rockwell C	ASTM E18	25 ± 5	39 ± 3	25 ± 5	39 ± 3
Impact toughness ⁴ (J ft-lb)	ASTM E23	52 ± 3	NA	39±2	NA

Thermal Properties⁵

MEASUREMENT	CONDITION	METRIC	U.S.
Thermal conductivity (W/(m.K) Btu/(h.ft².°F))	at 20°C / 120 °F	14	8
CTE - Coefficient of thermal expansion (µm/(m.°C) µ inch/(inch. °F))	in the range of 20 to 600 °C	14	8
Melting range (°C °F)		1350 - 1430	2460 - 2610

¹ Parts manufactured with standard parameters on a ProX DMP 320, Config B

² Values based on average and standard deviation

³ HIP indicates hot isostatic pressing post treatment

⁴ Tested with Charpy V-notch impact test specimens type A at room temperature

⁵ Values based on literature

NA = Not available



LaserForm® CoCrF75 (A)

Electrical Properties⁵

MEASUREMENT	METRIC	U.S.
Electrical resistivity (nΩ.m μΩ.in)	874	34

Physical Properties

MEASUREMENT	METRIC		U.S.	
	AS BUILT AND AFTER STRESS RELIEF	AFTER HIP	AS BUILT AND AFTER STRESS RELIEF	AFTER HIP
Density				
Relative, based on pixel count ¹ (%)	>99,9	≈100	>99,9	≈100
Absolute theoretical ⁵ (g/cm³ lb/in³)		8.35		0.302

Surface Quality¹

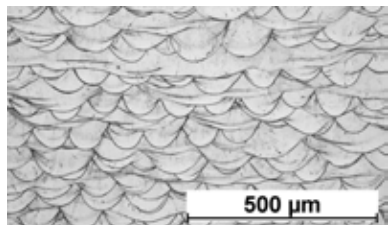
MEASUREMENT	METRIC		U.S.	
	AS BUILT	SAND BLASTED	AS BUILT	SAND BLASTED
Surface Roughness R _a				
Vertical direction (Z) (μm μin)	9 - 13	3 - 5	350 - 510	120 - 200

Chemical Composition

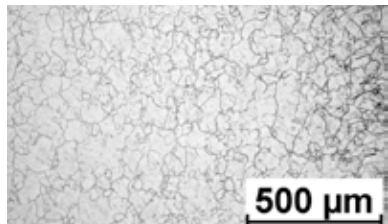
ELEMENT	% OF WEIGHT
Co	Bal.
Cr	27.00-30.00
Mo	5.00-7.00
Ni	≤0.50
Fe	≤0.75
C	≤0.35
Si	≤1.00
Mn	≤1.00
W	≤0.20
P	≤0.020
B, S	≤0.010
N	≤0.25
Al, Ti	≤0.10

¹ Parts manufactured with standard parameters on a ProX DMP 320, Config B

⁵ Values based on literature



Microstructure as built



Microstructure after anneal



Microstructure after HIP

 **3D SYSTEMS®**

www.3dsystems.com

Tel: +1 803 326 3930

Warranty/Disclaimer: The performance characteristics of these products may vary according to product application, operating conditions, or with end use. 3D Systems makes no warranties of any type, express or implied, including, but not limited to, the warranties of merchantability or fitness for a particular use.

©2017 by 3D Systems, Inc. All rights reserved. Specifications subject to change without notice. 3D Systems, ProX and LaserForm are registered trademarks and the 3D Systems logo is a trademark of 3D Systems, Inc.



LaserForm® Maraging Steel (B)

Maraging Steel fine-tuned for use with ProX® DMP 200 and ProX® DMP 300 metal printers producing industrial parts and tool inserts with a combination of high-strength and excellent hardness.

LaserForm Maraging Steel (B) is formulated and fine-tuned specifically for 3D Systems ProX DMP 200 and 300 metal 3D printers to deliver high part quality and consistent part properties. The print parameter database that 3D Systems provides together with the material has been extensively developed, tested and optimized in 3D Systems' part production facilities that hold the unique expertise of printing 500,000 challenging metal production parts in various materials year over year. For a 24/7 production operation 3D Systems' thorough Supplier Quality Management System guarantees consistent, monitored material quality for reliable process results.

Material Description

With properties like 1.2709, this steel is easily heat-treatable in a simple age-hardening process resulting in excellent hardness and strength. LaserForm Maraging Steel (B) has good wear resistance. In regards to post-processing, the material shows good weldability and machinability. LaserForm Maraging Steel (B) is ideal for innovative tool and mold designs including conformal cooling channels for injection molding, die casting and extrusion. The material is also used for high-performance aerospace, automotive and other industrial applications which require high strength and wear resistance.

Classification

The chemical composition of LaserForm Maraging Steel (B) with additional restrictions compared to the DIN 1.2709 standards is indicated in the table below in % of weight.

Mechanical Properties^{1,2}

MEASUREMENT	CONDITION	METRIC			U.S.		
		AS BUILT	AFTER STRESS RELIEF	AFTER AGEING	AS BUILT	AFTER STRESS RELIEF	AFTER AGEING
Youngs modulus (GPa ksi)	ASTM E8M						
Horizontal direction - XY Vertical direction - Z		160 ± 30 145 ± 30	160 ± 20 155 ± 20	185 ± 20 165 ± 20	23200 ± 4400 21000 ± 4400	23200 ± 2900 22500 ± 2900	26800 ± 2900 24000 ± 2900
Ultimate strength (MPa ksi)	ASTM E8M						
Horizontal direction - XY Vertical direction - Z		1180 ± 20 1050 ± 40	1130 ± 20 1100 ± 40	2190 ± 50 2140 ± 50	170 ± 3 150 ± 6	165 ± 3 160 ± 6	320 ± 7 310 ± 7
Yield strength Rp0.2% (MPa ksi)	ASTM E8M						
Horizontal direction - XY Vertical direction - Z		950 ± 60 780 ± 60	800 ± 50 790 ± 50	1870 ± 80 1750 ± 80	140 ± 9 115 ± 9	115 ± 7 115 ± 7	270 ± 12 255 ± 12
Elongation at break (%)	ASTM E8M						
Horizontal direction - XY Vertical direction - Z		13 ± 3 13 ± 3	13 ± 3 13 ± 3	3 ± 1.5 1.5 ± 0.5	13 ± 3 13 ± 3	13 ± 3 13 ± 3	3 ± 1.5 1.5 ± 0.5
Reduction of area (%)	ASTM E8M						
Horizontal direction - XY Vertical direction - Z		55 ± 5 60 ± 5	55 ± 10 50 ± 10	12 ± 5 7 ± 5	55 ± 5 60 ± 5	55 ± 10 50 ± 10	12 ± 5 7 ± 5
Hardness, Rockwell C	NF EN ISO 6508-1	36 ± 2	33 ± 2	55 ± 3	36 ± 2	33 ± 2	55 ± 3

¹ Parts manufactured with standard parameters on ProX® DMP 200 and ProX® DMP 300

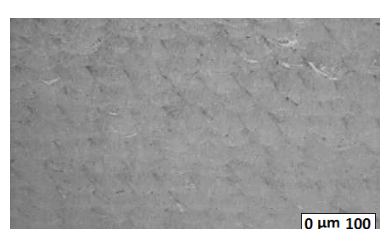
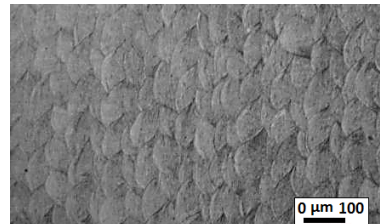
² Values based on average and double standard deviation



LaserForm® Maraging Steel (B)

Thermal Properties¹

MEASUREMENT	CONDITION	METRIC	U.S.
Thermal conductivity (W/(m.K) Btu/(h.ft.°F))	at 20°C / 120 °F	20.9	12.1
CTE - Coefficient of thermal expansion (µm/(m.°C) µ inch/(inch . °F))	in the range of 20 to 600 °C	10	5.6
Melting range (°C °F)		1430 - 1450	2610 - 2640



Electrical Properties¹

MEASUREMENT	METRIC	U.S.
Electrical resistivity (µΩ.m µΩ.in)	0.44	17.32



Physical Properties

MEASUREMENT	METRIC	U.S.
	AS BUILT, AFTER STRESS RELIEF AS BUILT, AFTER STRESS RELIEF AND AFTER AGEING AND AFTER AGEING	
Density		
Relative, based on pixel count ² (%)	>99,5	
Absolute theoretical ¹ (g/cm³ lb/in³)	8.06	0.291

Microstructure after ageing

Chemical Composition

ELEMENT	% OF WEIGHT
Fe	Bal.
Ni	17.00-19.00
Co	9.00-11.00
Mo	4.00-6.00
Ti	0.90-1.10
Si	≤1.00
Mn	≤1.00
C	≤0.03

¹ Values based on literature

² Parts manufactured with standard parameters on a ProX DMP 200 and 300

 **3D SYSTEMS®**

www.3dsystems.com

Warranty/Disclaimer: The performance characteristics of these products may vary according to product application, operating conditions, or with end use. 3D Systems makes no warranties of any type, express or implied, including, but not limited to, the warranties of merchantability or fitness for a particular use.

©2019 by 3D Systems, Inc. All rights reserved. Specifications subject to change without notice. 3D Systems, ProX and LaserForm are registered trademarks and the 3D Systems logo is a trademark of 3D Systems, Inc.



LaserForm® Ni625 (A)

Ni625 fine-tuned for use with ProX® DMP 320 metal printer producing industrial parts with high heat resistance, high strength and high corrosion resistance. LaserForm Ni626 (A) is especially resistant to crevice and pitting corrosion.

LaserForm Ni625 (A) is formulated and fine-tuned specifically for 3D Systems DMP 320 metal 3D Printers to deliver high part quality and consistent part properties. The print parameter database that 3D Systems provides together with the material has been extensively developed, tested and optimized in 3D Systems' part production facilities that hold the unique expertise of printing 500,000 challenging metal production parts in various materials year over year. And for your 24/7 production 3D Systems' thorough Supplier Quality Management System guarantees consistent, monitored material quality for reliable results.

Material Description

Ni625 is known for its combination of high strength and excellent corrosion resistance. LaserForm Ni625 (A) is the ideal material for industries where these two strengths need to come together: chemical, marine, aerospace and nuclear industry. Applications include: reaction vessels, tubing, heat exchangers, valves, engine exhaust systems, turbine seals, propeller blades, submarine fittings, propulsion motors, reactor core and control-rod components in nuclear water reactors.

Classification

The chemical composition of LaserForm Ni625 (A) corresponds to ASTM F3056, UNS N06625, Werkstoff Nr. 2.4856, DIN NiCr22Mo9Nb and AMS 5666 and is indicated in the table below in wt%.

Mechanical Properties^{1,2}

MEASUREMENT	CONDITION	METRIC			U.S.		
		AS-BUILT	AFTER STRESS RELIEF	AFTER LOW SOLUTION ANNEAL	AS-BUILT	AFTER STRESS RELIEF	AFTER LOW SOLUTION ANNEAL
Ultimate strength (MPa ksi)	ASTM E8M						
Horizontal direction - XY		1040 ± 20	1110 ± 60	1030 ± 20	150 ± 3	160 ± 9	150 ± 3
Vertical direction - Z		1030 ± 20	1050 ± 30	980 ± 20	150 ± 3	153 ± 5	142 ± 3
Yield strength Rp0.2% (MPa ksi)	ASTM E8M						
Horizontal direction - XY		770 ± 30	750 ± 60	640 ± 20	110 ± 5	110 ± 9	93 ± 3
Vertical direction - Z		730 ± 20	700 ± 40	600 ± 20	105 ± 3	100 ± 6	87 ± 3
Elongation at break (%)	ASTM E8M						
Horizontal direction - XY		22 ± 2	19 ± 3	27 ± 3	22 ± 2	19 ± 3	27 ± 3
Vertical direction - Z		33 ± 1	23 ± 3	34 ± 3	33 ± 1	23 ± 3	34 ± 3
Reduction of area (%)							
Vertical direction - Z	ASTM E8M	30 ± 2	26 ± 2	31 ± 1	30 ± 2	26 ± 2	31 ± 1
Hardness, Rockwell C	ASTM E18	29 ± 3	32 ± 3	28 ± 4	29 ± 3	32 ± 3	28 ± 4
Impact toughness ³ (J ft-lb)	ASTM E23	NA	NA	84 ± 7	NA	NA	62 ± 5

Thermal Properties⁴

MEASUREMENT	CONDITION	METRIC	U.S.
Thermal conductivity (W/(m.K) Btu/(h.ft².°F))	at 21 °C / 70 °F	9.8	5.7
CTE - Coefficient of thermal expansion (µm/(m.°C) µ inch/(inch . °F))	at 93 °C / 200 °F at 538°C / 1000°F at 871°C/1600°F	12.8 14.0 15.8	7.1 7.8 8.8
Melting range (°C °F)		1290 - 1350	2355 - 2465

¹ Parts manufactured with standard parameters on a ProX DMP 320, Config B

² Values based on average and standard deviation

³ Tested with Charpy V-notch impact test specimens type A at room temperature

⁴ Values based on literature

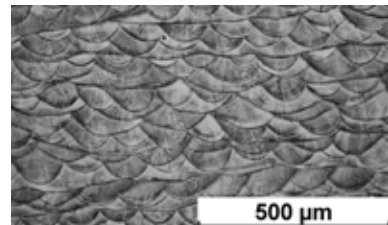
NA = Not available



LaserForm® Ni625 (A)

Physical Properties

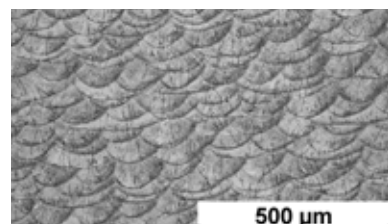
MEASUREMENT	METRIC	U.S.
	AS BUILT AND AFTER STRESS RELIEF	
Density		
Relative, based on pixel count ¹ (%)	>99,9	>99,9
Absolute theoretical ⁴ (g/cm ³ lb/in ³)	8.44	0.305



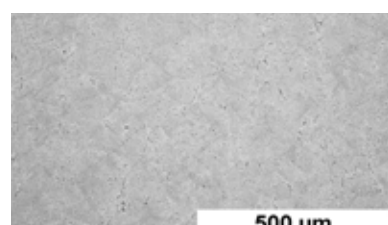
Microstructure as built

Surface Quality¹

MEASUREMENT	METRIC		U.S.	
	AS BUILT	SAND BLASTED	AS BUILT	SAND BLASTED
Surface Roughness R _a				
Horizontal direction (XY) (µm µin)	4 - 7	1 - 4	160 - 275	40 - 160
Vertical direction (Z) (µm µin)	8 - 11	4 - 7	320 - 433	160 - 275



Microstructure after stress relief



Microstructure after low solution anneal

Chemical Composition

The chemical composition of LaserForm Ni625 (A) corresponds to UNS N06625, Werkstoff Nr. 2.4856, DIN NiCr22Mo9Nb and AMS5 5666 and is indicated in the table below in wt%.

ELEMENT	% OF WEIGHT
Ni	≥ 58.00
Cr	20.00 - 23.00
Mo	8.00 - 10.00
Fe	≤ 5.00
Co	≤ 1.00
Nb	3.15 - 4.15
Ta	≤ 0.05
Ti	≤ 0.40
Al	≤ 0.40
Cu	≤ 0.50
Mn	≤ 0.50



www.3dsystems.com

Tel: +1 803 326 3930

Warranty/Disclaimer: The performance characteristics of these products may vary according to product application, operating conditions, or with end use. 3D Systems makes no warranties of any type, express or implied, including, but not limited to, the warranties of merchantability or fitness for a particular use.

©2017 by 3D Systems, Inc. All rights reserved. Specifications subject to change without notice. 3D Systems, ProX and LaserForm are registered trademarks and the 3D Systems logo is a trademark of 3D Systems, Inc.

¹ Parts manufactured with standard parameters on a ProX DMP 320, Config B

⁴ Values based on literature



LaserForm® Ni625 (B)

Ni625 fine-tuned for use with ProX® DMP 200 metal printers producing industrial parts with high heat resistance, high strength and high corrosion resistance. LaserForm Ni625 (B) is especially resistant to crevice and pitting corrosion.

LaserForm Ni625 (B) is formulated and fine-tuned specifically for 3D Systems DMP 200 metal 3D Printers to deliver high part quality and consistent part properties. The print parameter database that 3D Systems provides together with the material has been extensively developed, tested and optimized in 3D Systems' part production facilities that hold the unique expertise of printing 500,000 challenging metal production parts in various materials year over year. And for your 24/7 production 3D Systems' thorough Supplier Quality Management System guarantees consistent, monitored material quality for reliable results.

Material Description

Ni625 is known for its combination of high strength and excellent corrosion resistance. LaserForm Ni625 (B) is the ideal material for industries where these two strengths need to come together: chemical, marine, aerospace and nuclear industry. Applications include: reaction vessels, tubing, heat exchangers, valves, engine exhaust systems, turbine seals, propeller blades, submarine fittings, propulsion motors, reactor core and control-rod components in nuclear water reactors.

Classification

The chemical composition of LaserForm Ni625 (B) corresponds to ASTM F3056, UNS N06625, Werkstoff Nr. 2.4856, DIN NiCr22Mo9Nb and AMS 5666 and is indicated in the table below in wt%.

Mechanical Properties^{1,2}

MEASUREMENT	CONDITION	METRIC			U.S.		
		AS-BUILT	AFTER STRESS RELIEF	AFTER LOW SOLUTION ANNEAL	AS-BUILT	AFTER STRESS RELIEF	AFTER LOW SOLUTION ANNEAL
Ultimate strength (MPa ksi)	ASTM E8M						
Horizontal direction - XY		1120 ± 60	1190 ± 100	1090 ± 100	162 ± 9	173 ± 15	158 ± 15
Vertical direction - Z		1020 ± 60	1100 ± 100	1000 ± 100	148 ± 9	160 ± 15	145 ± 15
Yield strength Rp0.2% (MPa ksi)	ASTM E8M						
Horizontal direction - XY		855 ± 60	830 ± 100	710 ± 60	124 ± 9	120 ± 15	103 ± 9
Vertical direction - Z		740 ± 60	775 ± 100	660 ± 60	107 ± 9	112 ± 15	96 ± 9
Elongation at break (%)	ASTM E8M						
Horizontal direction - XY		28 ± 6	20 ± 4	28 ± 8	28 ± 6	20 ± 4	28 ± 8
Vertical direction - Z		31 ± 4	22 ± 4	30 ± 8	31 ± 4	22 ± 4	30 ± 8
Reduction of area (%)	ASTM E8M						
Horizontal direction - XY		32 ± 6	22 ± 4	29 ± 6	32 ± 6	22 ± 4	29 ± 6
Vertical direction - Z		45 ± 6	30 ± 4	32 ± 6	45 ± 6	30 ± 4	32 ± 6
Hardness, Rockwell C	ISO 6508-1	30 ± 3	34 ± 3	30 ± 3	30 ± 3	34 ± 3	30 ± 3
Youngs Modulus (GPa ksi)	ASTM E8M						
Horizontal direction - XY		220 ± 20	225 ± 20	225 ± 20	31900 ± 3000	32630 ± 3000	32630 ± 3000
Vertical direction - Z		170 ± 20	180 ± 20	180 ± 20	24650 ± 3000	26100 ± 3000	26100 ± 3000

¹ Parts manufactured with standard parameters on ProX DMP 200

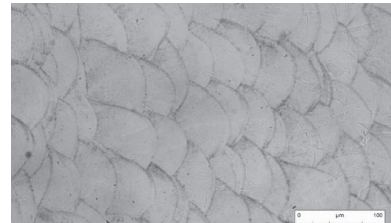
² Values based on average and double standard deviation



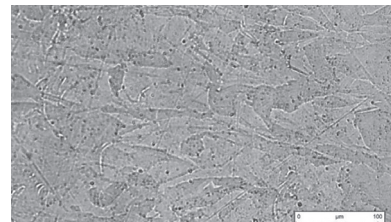
LaserForm® Ni625 (B)

Thermal Properties¹

MEASUREMENT	CONDITION	METRIC	U.S.
Thermal conductivity (W/(m.K) Btu/(h.ft².°F))	at 20 °C / 68 °F	9.8	5.7
CTE - Coefficient of thermal expansion (µm/(m.°C) µ inch/(inch . °F))	at 20 °C / 68 °F	12.0	6.7
Melting range (°C °F)		1290 - 1350	2355 - 2465



Microstructure as built



Microstructure after stress relief



Microstructure after low solution anneal

Physical Properties

MEASUREMENT	CONDITION	METRIC	U.S.
		AS BUILT AND AFTER STRESS RELIEF	
Density			
Relative, based on pixelcount (%)	Optical method	> 99.9	> 99.9
Absolute theoretical ¹ (g/cm³ lb/in³)		8.44	0.305

Chemical Composition

The chemical composition of LaserForm Ni625 (B) corresponds to UNS N06625, Werkstoff Nr. 2.4856, DIN NiCr22Mo9Nb and AMS 5666 and is indicated in the table below in wt%.

ELEMENT	% OF WEIGHT
Ni	balance
Cr	20.00 - 23.00
Nb	3.15 - 4.15
Mo	8.00 - 10.00
Ti	≤ 0.40
Al	≤ 0.40
Si	≤ 0.50
Mn	≤ 0.50
C	≤ 0.10
Co	≤ 1.00
P	≤ 0.015
S	≤ 0.015



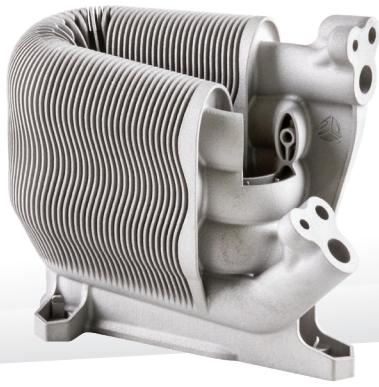
www.3dsystems.com

Tel: +1 803 326 3930

Warranty/Disclaimer: The performance characteristics of these products may vary according to product application, operating conditions, or with end use. 3D Systems makes no warranties of any type, express or implied, including, but not limited to, the warranties of merchantability or fitness for a particular use.

©2018 by 3D Systems, Inc. All rights reserved. Specifications subject to change without notice. 3D Systems, ProX and LaserForm are registered trademarks and the 3D Systems logo is a trademark of 3D Systems, Inc.

¹ Values based on literature



LaserForm® 316L (B)

Extra low-carbon grade Stainless Steel which is fine-tuned for use with the DMP Flex 100 and the ProX® DMP 200, producing parts with high corrosion resistance and sterilisability. LaserForm 316L (B) yields crack free and completely dense parts for all your applications.

LaserForm 316L (B) is formulated and fine-tuned specifically for 3D Systems DMP Flex 100 and DMP 200 metal 3D Printers to deliver highest part quality and best part properties. The print parameter database that 3D Systems provides together with the material has been extensively developed, tested and optimized in 3D Systems' part production facilities that hold the unique expertise of printing 500,000 challenging production parts year over year. And for a 24/7 production 3D Systems' thorough Supplier Quality Management System guarantees consistent, monitored material quality for reliable process results.

Material Description

Austenitic stainless steel type LaserForm 316L is the extra low carbon grade of 316. This steel is used as a general purpose material with excellent mechanical and corrosion properties at room temperature. Its chloride resistance makes this specific grade of stainless steel suitable for marine applications. 316L stainless steel is also the preferred material for use in hydrogen atmospheres or for hydrogen piping / cooling applications. Furthermore 316L retains good mechanical properties at sub-zero and even cryogenic temperatures and is suitable for structural components in low-temperature applications.

Classification

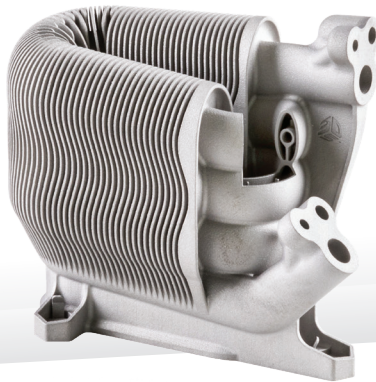
Parts built with LaserForm 316L alloy have a chemical composition that conforms to the compositional requirements of ASTM A276 - UNS S31603.

Mechanical Properties^{1,2}

MEASUREMENT	CONDITION	METRIC			U.S.		
		AS BUILT	AFTER STRESS RELIEF	FULL ANNEAL	AS BUILT	AFTER STRESS RELIEF	FULL ANNEAL
Youngs modulus (GPa ksi)							
Horizontal direction — XY		200 ± 30	200 ± 30	200 ± 30	29000 ± 4400	29000 ± 4400	29000 ± 4400
Vertical direction — Z		145 ± 30	160 ± 30	160 ± 30	21000 ± 4400	23200 ± 4400	23200 ± 4400
Ultimate Strength (MPa ksi)	ASTM E8M						
Horizontal direction — XY		710 ± 50	740 ± 50	670 ± 50	103 ± 7	107 ± 7	97 ± 7
Vertical direction — Z		630 ± 50	660 ± 50	600 ± 50	91 ± 7	96 ± 7	87 ± 7
Yield strength Rp0.2% (MPa ksi)	ASTM E8M						
Horizontal direction — XY		590 ± 50	610 ± 60	440 ± 60	86 ± 7	88 ± 9	64 ± 9
Vertical direction — Z		520 ± 50	530 ± 60	410 ± 60	75 ± 7	77 ± 9	59 ± 9
Elongation at break (%)	ASTM E8M						
Horizontal direction — XY		41 ± 5	37 ± 5	44 ± 5	41 ± 5	37 ± 5	44 ± 5
Vertical direction — Z		37 ± 5	34 ± 5	42 ± 5	37 ± 5	34 ± 5	42 ± 5
Reduction of area (%)	ASTM E8M						
Horizontal direction — XY		65 ± 5	65 ± 5	58 ± 5	65 ± 5	65 ± 5	58 ± 5
Vertical direction — Z		65 ± 10	59 ± 10	54 ± 10	65 ± 10	59 ± 10	54 ± 10
Hardness, Vickers (HV30)	ISO 6507-1	227 ± 10	230 ± 10	200 ± 10	227 ± 10	230 ± 10	200 ± 10

¹ Parts manufactured with standard parameters on a DMP Flex 100 and ProX® DMP 200

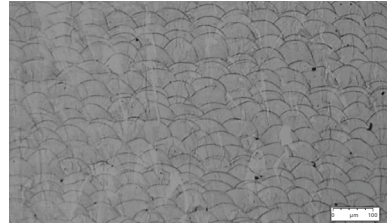
² Values based on average and double standard deviation



LaserForm® 316L (B)

Thermal Properties¹

MEASUREMENT	CONDITION	METRIC	U.S.
Thermal conductivity (W/(m.K) Btu/(h.ft. ^o F))	At 20 °C/ 68 °F	15	9
Coefficient of Thermal Expansion ($\mu\text{m}/(\text{m.}^{\circ}\text{C})$ $\mu\text{inch}/(\text{inch.}^{\circ}\text{F})$)	In the range of 20 - 600°C / 68-1112°F	19.0	10.6
Melting range (°C °F)		1370-1400	2500-2550



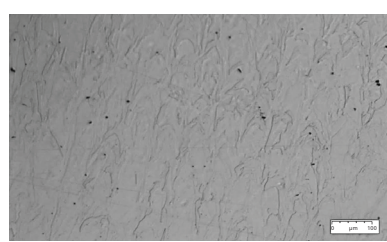
Microstructure as built

Physical Properties¹

MEASUREMENT	CONDITION	METRIC		U.S.	
		AS BUILT AND AFTER STRESS RELIEF	AFTER FULL ANNEAL	AS BUILT AND AFTER STRESS RELIEF	AFTER FULL ANNEAL
Density					
Relative, based on pixelcount (%)	Optical method	> 99.7		> 99.7	
Absolute theoretical (g/cm ³ lb/in ³)		7.95		0.287	



Microstructure after stress relief



Microstructure after full anneal

Chemical Composition

ELEMENT	% OF WEIGHT
Fe	bal.
Cr	16.50-18.00
Ni	10.00-13.00
C	≤0.030
Mn	≤2.00
Mo	2.00-2.50
Si	≤1.00
P	≤0.040
S	≤0.030

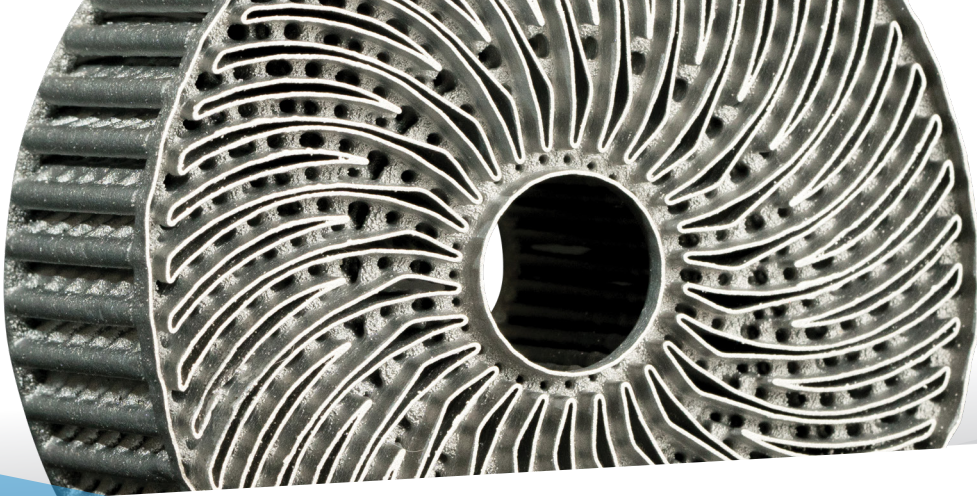
 **3D SYSTEMS®**

www.3dsystems.com

Warranty/Disclaimer: The performance characteristics of these products may vary according to product application, operating conditions, or with end use. 3D Systems makes no warranties of any type, express or implied, including, but not limited to, the warranties of merchantability or fitness for a particular use.

©2019 by 3D Systems, Inc. All rights reserved. Specifications subject to change without notice. 3D Systems, ProX and LaserForm are registered trademarks and the 3D Systems logo is a trademark of 3D Systems, Inc.

¹ Values based on literature



LaserForm AISi10Mg (A)

AISi10Mg fine-tuned for use with ProX® DMP 320, DMP Flex 350, DMP Factory 350 and DMP Factory 500 printers producing industrial parts with a combination of good mechanical properties and good thermal conductivity.

LaserForm AISi10Mg (A) is formulated and fine-tuned specifically for 3D Systems ProX® DMP 320, DMP Flex 350, DMP Factory 350 and DMP Factory 500 metal 3D printers to deliver high part quality and consistent part properties. The print parameter database that 3D Systems provides together with the material has been extensively developed, tested and optimized in 3D Systems' part production facilities that hold the unique expertise of printing more than 1,000,000 challenging metal production parts in various materials year over year. Based on a multitude of test samples, the properties listed below provide high confidence to the user in terms of job-to-job and machine-to-machine repeatability. Using the LaserForm material enables the user to experience consistent and reliable part quality.

Material Description

AISi10Mg combines silicon and magnesium as alloying elements, which results in a significant increase in strength and hardness compared to other aluminum alloys. Due to the very rapid melting and solidification during Direct Metal Printing, LaserForm AISi10Mg (A) in as-printed condition shows fine microstructure and high strengths.

In the aerospace and automotive industry, LaserForm AISi10Mg (A) is used for its light weight. Both innovative approaches to mold design and specific heat exchanger applications make use of the high thermal conductivity of this alloy.

CLASSIFICATION:

Parts built with LaserForm AISi10Mg (A) have a chemical composition that complies with EN AC-43000 and ASTM F3318.

Mechanical Properties

PROX DMP 320, DMP FLEX 350, DMP FACTORY 350 - LT 30 ^{1,4,5}	TEST METHOD	METRIC			U.S.		
		NHT	SR1	SR2	NHT	SR1	SR2
Ultimate tensile strength (MPa ksi)	ASTM E8						
Horizontal direction - XY		470 ± 10	300 ± 20	400 ± 15	68 ± 1	44 ± 3	58 ± 2
Vertical direction - Z		460 ± 25	300 ± 20	430 ± 15	67 ± 4	44 ± 3	62 ± 2
Yield strength Rp0.2% (MPa ksi)		280 ± 10	190 ± 20	270 ± 10	41 ± 1	28 ± 3	39 ± 1
Horizontal direction - XY		240 ± 10	180 ± 20	250 ± 10	35 ± 1	26 ± 3	36 ± 1
Vertical direction - Z							
Plastic elongation (%)		13.2 ± 4.8	15.6 ± 3.6	9.2 ± 3.8	13.2 ± 4.8	15.6 ± 3.6	9.2 ± 3.8
Horizontal direction - XY		8.3 ± 4.0	15.8 ± 2.7	5.2 +3.7/-2.6	8.3 ± 4.0	15.8 ± 2.7	5.2 +3.7/-2.6
PROX DMP 320, DMP FLEX 350, DMP FACTORY 350 - LT 60 ^{2,4,5}	TEST METHOD	METRIC			U.S.		
		NHT	SR1	SR2	NHT	SR1	SR2
Ultimate tensile strength (MPa ksi)	ASTM E8						
Horizontal direction - XY		440 ± 30	290 ± 20	390 ± 20	64 ± 4	42 ± 3	57 ± 3
Vertical direction - Z		425 ± 50	290 ± 20	400 ± 40	62 ± 7	42 ± 3	58 ± 6
Yield strength Rp0.2% (MPa ksi)		260 ± 15	170 ± 20	255 ± 10	38 ± 2	25 ± 3	37 ± 1
Horizontal direction - XY		225 ± 10	170 ± 20	230 ± 10	33 ± 1	25 ± 3	33 ± 1
Vertical direction - Z							
Plastic elongation (%)		8.9 ± 5.0	14.0 ± 5.3	8.6 ± 2.0	8.9 ± 5.0	14.0 ± 5.3	8.6 ± 2.0
Horizontal direction - XY		7.6 ± 4.9	13.2 ± 6.0	5.1 ± 2.8	7.6 ± 4.9	13.2 ± 6.0	5.1 ± 2.8
DMP FACTORY 500 - LT 60 ^{3,4,5}	TEST METHOD	METRIC			U.S.		
		NHT	SR1	SR2	NHT	SR1	SR2
Ultimate tensile strength (MPa ksi)	ASTM E8						
Horizontal direction - XY		NA	290 ± 20	405 ± 20	NA	42 ± 3	59 ± 3
Vertical direction - Z			300 ± 20	420 +20/-60		44 ± 3	61 +3/-9
Yield strength Rp0.2% (MPa ksi)		NA	170 ± 20	270 +15/-30	NA	25 ± 3	39 +2/-4
Horizontal direction - XY			180 ± 20	250 ± 20		26 ± 3	36 ± 3
Vertical direction - Z							
Plastic elongation (%)		NA	17.5 ± 4.9	9.4 ± 5.5	NA	17.5 ± 4.9	9.4 ± 5.5
Horizontal direction - XY			13.3 ± 5.7	5.8 ± 3.4		13.3 ± 5.7	5.8 ± 3.4

¹ Parts manufactured with standard parameters and protocols on a ProX DMP 320, DMP Flex and Factory 350, Config B, using layer thickness 30 µm (LT30)

² Parts manufactured with standard parameters and protocols on a ProX DMP 320, DMP Flex and Factory 350, Config B, using layer thickness 60 µm (LT60)

³ Parts manufactured with standard parameters and protocols on a DMP Factory 500, using layer thickness 60 µm (LT60)

⁴ NHT is non-heat-treated sample condition; SR1 is a heat treatment at 285 °C for 2 h; SR2 is a heat treatment at 190 °C for 6h. Values based on average and 95% tolerance interval with 95% confidence

⁵ Tested according to ASTM E8 using round tensile test specimen type 4

Printed Part Properties⁶

DENSITY	TEST METHOD	METRIC	U.S.
Theoretical density ⁷ (g/cm ³ lb/in ³)	Value from literature	2.68	0.097
Relative density (%), layer thickness 30 µm ^{1,8}	Optical method (pixel count)	≥ 99.7 Typical 99.9	≥ 99.7 Typical 99.9
Relative density (%), layer thickness 60 µm ^{2,3,8}	Optical method (pixel count)	≥ 99.5 Typical 99.8	≥ 99.5 Typical 99.8
SURFACE ROUGHNESS R _s ^{9,10}	TEST METHOD	METRIC	U.S.
Vertical side surface (µm µin) Layer thickness 30 µm	ISO 25178	Typically, around 8	Typically, around 315
Vertical side surface (µm µin) Layer thickness 60 µm	ISO 25178	Typically, around 15	Typically, around 591

Thermal Properties

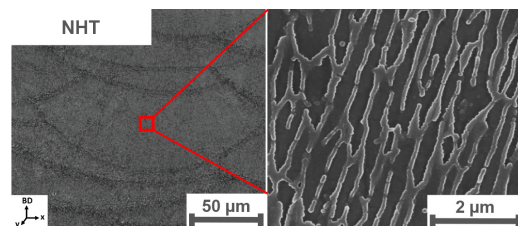
MEASUREMENT	CONDITION	METRIC			U.S.		
		NHT	SR1	SR2	NHT	SR1	SR2
Thermal conductivity ^{11,12} (W/(m.K) BTU-in/h-ft ² .°F)	at 20 °C / 68 °F	120-130	160-170	140-160	833-902	1110 -1180	971-1110
CTE - Coefficient of thermal expansion ⁷ (µm/(m.°C) µ inch/(inch . °F))	in the range of 20 to 100 °C	—typical 20.9—	—typical 11.6—	—	—	—	—
Melting range ⁷ (°C °F)		—typical 557 - 596—	—	—typical 1035 - 1105—	—	—	—

Electrical Properties^{12,13}

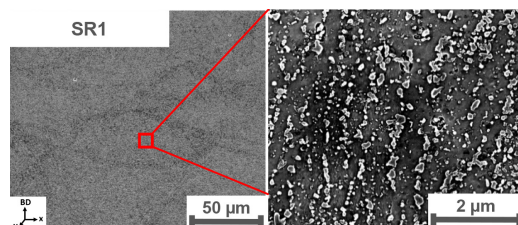
MEASUREMENT	CONDITION	METRIC			U.S.		
		NHT	SR1	SR2	NHT	SR1	SR2
Electrical conductivity (10 ⁶ S/m)	ASTM B193 at 20°C / 68°F	17-18	22-24	20-22	17-18	22-24	20-22

Chemical Composition

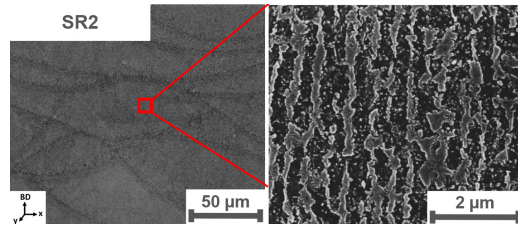
ELEMENT	% OF WEIGHT
Al	Balance
Si	9.00-11.00
Mg	0.20-0.45
Fe	≤0.55
Cu	≤ 0.03
Mn	≤0.35
Ni	≤0.05
Zn	≤0.10
Pb	≤0.05
Sn	≤0.05
Ti	≤0.15
Other (each)	≤ 0.05
Other (total)	≤ 0.15



Microstructure without heat treatment (NHT)



Microstructure after SR1



Microstructure after SR2



www.3dsystems.com

⁶ May deviate depending on specific part geometry

⁷ Values based on literature

⁸ Minimum values based on 95% tolerance interval with 95% confidence.

Tested on specific 3DS density test coupons

⁹ Surface treatment performed with zirconia blasting medium at 2 bar

¹⁰ Vertical side surface measurement along the building direction

¹¹ Thermal conductivity values are calculated by the Wiedemann-Franz law using the respective electrical resistivity values

¹² Results are based on limited sample size, not statistically representative.

Samples printed on a ProX DMP 320, Config B

¹³ Electrical resistivity measurements are based on four point contact

method according to ASTM B193

Warranty/Disclaimer: The performance characteristics of these products may vary according to product application, operating conditions, or with end use. 3D Systems makes no warranties of any type, express or implied, including, but not limited to, the warranties of merchantability or fitness for a particular use.

©2021 by 3D Systems, Inc. All rights reserved. Specifications subject to change without notice. 3D Systems, the 3D Systems logo and ProX are registered trademarks of 3D Systems, Inc.



LaserForm® AISi12 (B)

Aluminum alloy fine-tuned for use with ProX DMP 200 and 300 metal 3D printers for production of lightweight components with good thermal properties.

LaserForm AISi12 (B) is formulated and fine-tuned specifically for 3D Systems' ProX® DMP 200 and 300 metal 3D printers to deliver highest part quality and best part properties. The print parameter database that 3D Systems provides together with the material has been extensively developed, tested and optimized in 3D Systems' part production facilities that hold the unique expertise of printing 500,000 challenging production parts, year over year in a large variety of materials. And for 24/7 production, 3D Systems' thorough Supplier Quality Management System guarantees consistent, monitored material quality for reliable process results.

Material Description

Known for its high strength-to-weight ratio and good thermal properties, the lightweight Laserform AISi12 (B) is frequently used in aerospace, aviation, motorsports and automotive applications as well as for specifically thin-walled applications such as the production of heat exchangers. With Direct Metal Printing, parts that were typically cast are now being directly printed. Even more complex designs than typical casting processes allow can be produced in one single piece using DMP.

Classification

The chemical composition of LaserForm AISi12 (B) conforms to the requirements of ISO 18273, ISO 17672, UNS A94047 and DIN EN 1706 specifications and is indicated in the table below in wt%.

Mechanical Properties^{1,2}

MEASUREMENT	CONDITION	METRIC		U.S.	
		AS-BUILT	STRESS RELIEF	AS-BUILT	STRESS RELIEF
Youngs modulus ³ (GPa ksi)					
Horizontal direction - XY		70 ± 5	65 ± 10	10150 ± 750	9430 ± 1500
Vertical direction - Z		65 ± 5	60 ± 5	8760 ± 750	9430 ± 1500
Ultimate strength ³ (MPa ksi)	ASTM E8M				
Horizontal direction - XY		470 ± 30	340 ± 30	68 ± 4	49 ± 4
Vertical direction - Z		490 ± 10	340 ± 10	71 ± 2	49 ± 2
Yield strength Rp0.2% ³ (MPa ksi)	ASTM E8M				
Horizontal direction - XY		290 ± 20	220 ± 20	42 ± 3	32 ± 3
Vertical direction - Z		260 ± 10	210 ± 10	38 ± 2	30 ± 2
Elongation at break ³ (%)	ASTM E8M				
Horizontal direction - XY		8 ± 2	12 ± 2	8 ± 2	12 ± 2
Vertical direction - Z		6 ± 2	10 ± 2	6 ± 2	10 ± 2
Hardness, Brinell HBW2,5/62,5	ISO 6506-1	97 ± 13	115 ± 5	97 ± 13	115 ± 5

Thermal Properties⁴

MEASUREMENT	CONDITION	METRIC	U.S.
Thermal conductivity (W/(m.K) Btu/(h.ft².F))	at 50°C / 120 °F	130-150	75-87
CTE - Coefficient of thermal expansion (µm/(m.°C) µ inch/(inch. °F))	in the range of 20 to 600 °C	20	11
Melting range (°C °F)		573-585	1060-1090

¹ Parts manufactured with standard parameters on a ProX DMP 200

² Values based on average and double standard deviation

³ Tested on ASTM E8M specimen with circular cross sections

⁴ Values based on literature



LaserForm® AlSi12 (B)

Electrical Properties¹

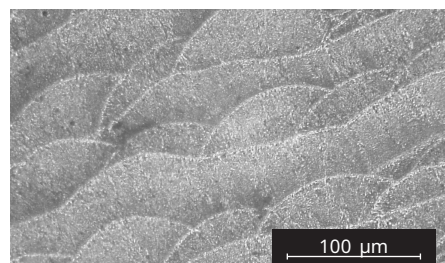
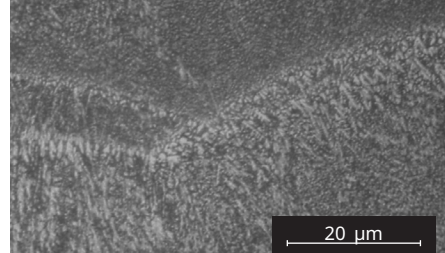
MEASUREMENT	METRIC	U.S.
Electrical resistivity (nΩ.m nΩ.in)	45-62	1771-2440

Physical Properties

MEASUREMENT	METRIC	U.S.
Density		
Relative, based on pixel count ² (%)	>99	>99
Absolute theoretical ¹ (g/cm ³ lb/in ³)	2.685	0.097

Chemical Composition

ELEMENT	% OF WEIGHT
Al	Balance
Si	11.0 - 13.0
Residuals	< 0.6



Microstructures after stress release



www.3dsystems.com

Warranty/Disclaimer: The performance characteristics of these products may vary according to product application, operating conditions, or with end use. 3D Systems makes no warranties of any type, express or implied, including, but not limited to, the warranties of merchantability or fitness for a particular use.

©2018 by 3D Systems, Inc. All rights reserved. Specifications subject to change without notice. 3D Systems, ProX and LaserForm are registered trademarks and the 3D Systems logo is a trademark of 3D Systems, Inc.

¹ Values based on literature

² Parts manufactured with standard parameters on a ProX DMP 200



LaserForm® AISi7Mg0.6 (A)

AISi7Mg0.6 fine-tuned for use with ProX® DMP 320 and DMP 350 metal printers to produce industrial parts with a combination of good mechanical properties and improved thermal conductivity.

LaserForm AISi7Mg0.6 (A) is formulated and fine-tuned specifically for 3D Systems DMP 320 and DMP 350 series 3D printers to deliver high part quality and consistent part properties. The print parameter database that 3D Systems provides together with the material has been extensively developed, tested and optimized in 3D Systems' part production facilities that hold the unique expertise of printing 500,000 challenging metal production parts in various materials year over year. And for 24/7 production 3D Systems' thorough Supplier Quality Management System guarantees consistent, monitored material quality for reliable results.

Material Description

AISi7Mg0.6 combines silicon and magnesium as alloying elements, which results in good mechanical properties. Due to the very rapid melting and solidification during Direct Metal Printing, LaserForm AISi7Mg0.6 (A) in as-printed condition shows a fine microstructure and obtains a good combination of strength and ductility. Lower silicon content improves electrical and thermal conductivity properties compared to AISi10Mg while the increased magnesium content maintains mechanical properties similar to AISi10Mg. Heat treatment allows electrical and thermal conductivity to be fine-tuned to the needs of the application. Additionally, the lower silicon content improves the anodization quality as well as the corrosion resistance.

LaserForm AISi7Mg0.6 (A)'s low material density is well suited for the aerospace and automotive industry. Innovative applications such as mold design and specific heat exchanger applications make use of the high thermal conductivity of this alloy.

Mechanical Properties^{1,2,3}

MEASUREMENT	CONDITION	METRIC			U.S.		
		AS-BUILT	AFTER STRESS RELIEF	DIRECT AGEING	AS-BUILT	AFTER STRESS RELIEF	DIRECT AGEING
Young's modulus (GPa ksi)	ASTM E1876						
Horizontal direction - XY		NA	NA	NA	NA	NA	NA
Vertical direction - Z		70-72	75-76	73-74	10100-10500	10800-11000	10600-10900
Ultimate strength (MPa ksi)	ASTM E8M						
Horizontal direction - XY		410 ± 20	280 ± 20	430 ± 20	59 ± 3	41 ± 3	62 ± 3
Vertical direction - Z		390 ± 40	290 ± 50	430 ± 30	56 ± 6	42 ± 7	62 ± 5
Yield strength Rp0.2% (MPa ksi)	ASTM E8M						
Horizontal direction - XY		240 ± 30	160 ± 40	310 ± 20	35 ± 5	23 ± 6	45 ± 3
Vertical direction - Z		210 ± 30	180 ± 40	280 ± 20	30 ± 5	26 ± 6	40 ± 3
Plastic elongation (%)	ASTM E8M						
Horizontal direction - XY		14 ± 4	18 ± 3	10 ± 3	14 ± 4	18 ± 3	10 ± 3
Vertical direction - Z		11 ± 5	11 ± 6	5 ± 3	11 ± 5	11 ± 6	5 ± 3
Hardness, Rockwell B (HRB)	ASTM E18	60 ± 3	39 ± 10	69 ± 2	60 ± 3	39 ± 10	69 ± 2

Thermal Properties

MEASUREMENT	CONDITION	METRIC			U.S.		
		AS BUILT	AFTER STRESS RELIEF	AFTER DIRECT AGEING	AS BUILT	AFTER STRESS RELIEF	AFTER DIRECT AGEING
Thermal conductivity ^{4,5} (W/(m.K) Btu/(h.ft.°F))	at 20°C / 68°F	120-140	180-190	150-170	70-80	105-110	85-100
CTE - Coefficient of thermal expansion ⁶ (µm/(m.°C) µ inch/(inch.°F))	in the range of 20 to 100 °C		typical 21.4			typical 11.9	
Melting range ⁶ (°C °F)			typical 557 - 613			typical 1035-1135	

Electrical Properties^{5,7}

MEASUREMENT	CONDITION	METRIC			U.S.		
		AS BUILT	AFTER STRESS RELIEF	AFTER DIRECT AGEING	AS BUILT	AFTER STRESS RELIEF	AFTER DIRECT AGEING
Electrical conductivity (10 ⁶ S/m)	ASTM B193 at 20°C / 68°F	17-19	25-27	22-24	17-19	25-27	22-24

¹ Parts manufactured with standard parameters on a ProX DMP 320, Config B

² Values based on average and double standard deviation

³ Surface condition of test samples: Horizontal samples (XY) tested in machined surface condition only, vertical (Z) tested in as-printed and machined surface condition

⁴ Thermal conductivity values are calculated via the Wiedemann-Franz law using the measured electrical resistivity values

⁵ Results are based on limited sample size, not statistically representative

⁶ Values based on literature

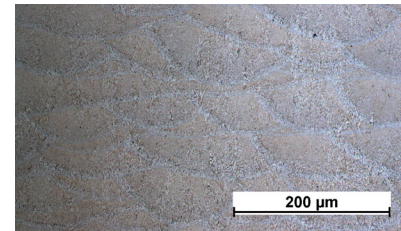
⁷ Electrical resistivity measurements are based on the four point contact method according to ASTM B193



LaserForm® AlSi7Mg0.6 (A)

Physical Properties

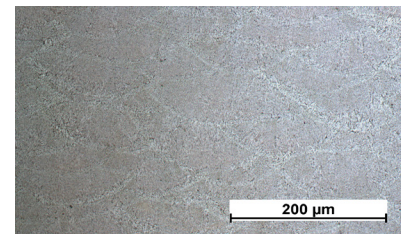
MEASUREMENT	CONDITION	METRIC	U.S.
Density			
Relative, based on pixel count ^{1,2,4} (%)	Optical method	> 99.2 typical 99.8	> 99.2 typical 99.8
Absolute theoretical ³ (g/cm³ lb/in³)		2.67	0.096



Microstructure as built

Surface Quality^{4,5}

MEASUREMENT	CONDITION	SAND BLASTED METRIC	SAND BLASTED U.S.
Surface Roughness R _a	ISO 25178		
Layer Thickness 30μm (μm μin)			
Vertical side surface ⁶		typical 5-7	typical 200-280
Layer Thickness 60μm (μm μin)			
Vertical side surface ⁶		typical 10-20	typical 400-800



Microstructure after stress relief

Chemical Composition

The chemical composition of LaserForm AlSi7Mg0.6 (A) conforms to the requirements EN AC-42200, and is indicated in the table below in wt%.

ELEMENT	% OF WEIGHT
Al	Balance
Si	6.50-7.50
Mg	0.45-0.70
Fe	≤0.15
Cu	≤0.03
Mn	≤0.10
Ni	≤0.05
Zn	≤0.07
Pb	≤0.05
Sn	≤0.05
Ti	≤0.18
Other (each)	≤ 0.03
Other (total)	≤ 0.10



www.3dsystems.com

Warranty/Disclaimer: The performance characteristics of these products may vary according to product application, operating conditions, or with end use. 3D Systems makes no warranties of any type, express or implied, including, but not limited to, the warranties of merchantability or fitness for a particular use.

©2020 by 3D Systems, Inc. All rights reserved. Specifications subject to change without notice. 3D Systems, the 3D Systems logo, ProX and LaserForm are registered trademarks of 3D Systems, Inc.

¹ Minimum value based on 95% confidence interval. Tested on typical density test coupons

² May deviate depending on specific part geometry

³ Values based on literature

⁴ Parts manufactured with standard parameters on a ProX DMP 320, Config B

⁵ Sand blasting performed with zirconia blasting medium at 2 bar

⁶ Vertical side surface measurement along the building direction



LaserForm® Maraging Steel (A)

Maraging steel fine-tuned for use with ProX® DMP 320 metal 3D printers to produce industrial parts and tool inserts with a combination of high-strength and excellent hardness.

LaserForm Maraging Steel (A) is formulated and fine-tuned specifically for 3D Systems DMP 320 metal 3D Printers to deliver highest part quality and best part properties. The print parameter database that 3D Systems provides together with the material has been extensively developed, tested and optimized in 3D Systems' part production facilities that hold the unique expertise of printing 500,000 challenging production parts year over year. Based on extensive testing the below listed part quality data and mechanical properties give you high planning security. For a 24/7 production operation, 3D Systems' thorough Supplier Quality Management System guarantees consistent, monitored material quality for reliable process results.

Material Description

With properties like 1.2709, this steel is easily heat-treatable in a simple age-hardening process resulting in excellent hardness and strength. LaserForm Maraging Steel (A) has good wear resistance. In regards to post-processing, the material shows good weldability and machinability. LaserForm Maraging Steel (A) is ideal for innovative tool and mold designs including conformal cooling channels for injection molding, die casting and extrusion. The material is also used for high-performance aerospace, automotive and other industrial applications which require high strength and wear resistance.

Classification

Parts built with LaserForm Maraging Steel (A) have a chemical composition that conforms to the compositional requirements of Werkstoff Nr. 1.2709.

Mechanical Properties^{1,2}

MEASUREMENT	CONDITION	METRIC			U.S.		
		AS-BUILT	AGEING 1	AGEING 2	AS-BUILT	AGEING 1	AGEING 2
Ultimate strength (MPa ksi)	ASTM E8M						
Horizontal direction - XY		1230 ± 70	2210 ± 30	2260 ± 30	178 ± 10	320 ± 5	328 ± 5
Vertical direction - Z		1220 ± 20	2120 ± 30	2160 ± 90	177 ± 3	307 ± 5	313 ± 13
Yield strength Rp0.2% (MPa ksi)	ASTM E8M						
Horizontal direction ⁴ - XY		1080 ± 90	2125 ± 30	2180 ± 40	115 ± 13	308 ± 4	316 ± 6
Vertical direction ⁵ - Z		1090 ± 50	2030 ± 60	2070 ± 80	158 ± 7	294 ± 9	300 ± 12
Elongation at break (%)	ASTM E8M						
Horizontal direction - XY		13 ± 2	5 ± 2	5 ± 2	13 ± 2	5 ± 2	5 ± 2
Vertical direction - Z		13 ± 2	5 ± 2	2 ± 1	13 ± 2	5 ± 2	2 ± 1
Hardness, Rockwell C	ASTM E18	35 ± 3	55 ± 3	55 ± 3	35 ± 3	55 ± 3	55 ± 3
Impact toughness ⁶ (J ft-lb) ³	ASTM E23	64 ± 5	8 ± 2	7 ± 2	47 ± 4	6 ± 2	5 ± 2

Thermal Properties⁴

MEASUREMENT	CONDITION	METRIC	U.S.
Thermal conductivity (W/(m.K) Btu/(h.ft².°F))	at 25°C / 36 °F	20.9	145
CTE - Coefficient of thermal expansion (µm/(m.°C) µ inch/(inch. °F))	In the range of 0 to 100 °C	10.0	5.6
Melting range (°C °F)		1430-1450	2610-2640

¹ Parts manufactured with standard parameters on a ProX DMP 320, Config B

² Values based on average and double standard deviation

³ Tested with Charpy V-notch impact test specimens type A at room temperature

⁴ Values based on literature



LaserForm® Maraging Steel (A)

Physical Properties¹

MEASUREMENT	METRIC		U.S.	
	AS-BUILT	AGEING	AS-BUILT	AGEING
Density				
Relative, based on pixelcount (%)			> 99.8%	
Absolute theoretical (g/cm ³ lb/in ³) ¹	8.1		0.293	



Microstructure as built

Surface Quality²

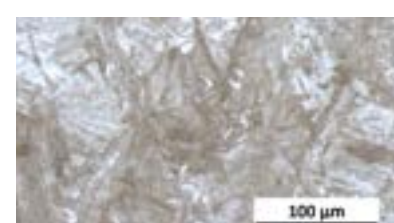
MEASUREMENT	SANDBLASTED METRIC	SANDBLASTED U.S.
Surface Roughness Ra		
Horizontal direction (XY) (μm μin)	4 - 7	157 - 276
Vertical direction (Z) (μm μin)	5 - 6	196 - 236



Microstructure ageing 1

Chemical Composition

ELEMENT	% OF WEIGHT
C	≤ 0.03
Si	≤ 0.10
Mn	≤ 0.15
P	≤ 0.01
S	≤ 0.01
Cr	≤ 0.25
Mo	4.50 - 5.20
Ni	17.0 - 19.0
Ti	0.80 - 1.20
Co	8.50 - 10.0
Fe	Rest



Microstructure ageing 2



www.3dsystems.com

Warranty/Disclaimer: The performance characteristics of these products may vary according to product application, operating conditions, or with end use. 3D Systems makes no warranties of any type, express or implied, including, but not limited to, the warranties of merchantability or fitness for a particular use.

©2017 by 3D Systems, Inc. All rights reserved. Specifications subject to change without notice. 3D Systems, ProX and LaserForm are registered trademarks and the 3D Systems logo is a trademark of 3D Systems, Inc.

¹ Values based on literature

² Values based on minimum and maximum ranges



LaserForm Ni718 (A)

A Nickel-based alloy fine-tuned for use with ProX® DMP 320, DMP Flex 350, DMP Factory 350 and DMP Factory 500 metal printers, producing parts for high temperature applications. LaserForm Ni718 (A) has outstanding corrosion resistance in various corrosive environments and excellent cryogenic properties.

LaserForm Ni718 (A) is formulated and fine-tuned specifically for 3D Systems ProX DMP 320, DMP Flex 350, DMP Factory 350 and DMP Factory 500 metal 3D printers to deliver highest part quality and best part properties. The print parameter database that 3D Systems provides together with the material has been extensively developed, tested and optimized in 3D Systems' part production facilities that hold the unique expertise of printing more than 1,000,000 challenging production parts year over year. Based on a multitude of test samples, the properties listed below provide high confidence to the user in terms of job-to-job and machine-to-machine repeatability. Using the LaserForm material enables the user to experience consistent and reliable part quality.

Material Description

LaserForm Ni718 (A) is a nickel-based heat resistant alloy. This precipitation-hardening nickel-chromium alloy is characterized by good tensile, fatigue, creep and rupture strength at temperatures up to 700°C. Moreover it has outstanding corrosion resistance in various corrosive environments as well as excellent cryogenic properties.

These benefits make LaserForm Ni718 (A) ideal for many high temperature applications such as gas turbine parts, instrumentation parts, power and process industry parts etc. Parts can be post-hardened over 1400 MPa Ultimate Tensile Strength (UTS) by precipitation-hardening heat treatments. The parts can be machined, spark-eroded, welded, shot-peened, polished and coated if required.

Classification

Parts built with LaserForm Ni718 Type (A) have a chemical composition that complies with ASTM F3055.

Mechanical Properties

PROX DMP 320, DMP FLEX 350, DMP FACTORY 350 – LT 30, 60 ^{1,2,3,4}		TEST METHOD	METRIC		U.S.	
NHT	HSAA		NHT	HSAA		
Ultimate Tensile Strength (MPa ksi)		ASTM E8/E8M				
Horizontal direction — XY			NA	1400 ± 60		
Vertical direction — Z			930 ± 20	1340 ± 40		
Yield strength Rp0.2% (MPa ksi)		ASTM E8/E8M				
Horizontal direction — XY			NA	1230 ± 60		
Vertical direction — Z			660 ± 20	1200 ± 40		
Elongation at break (%)		ASTM E8/E8M				
Horizontal direction — XY			NA	15 ± 4		
Vertical direction — Z			30 ± 4	14 ± 8		
					NA	203 ± 10
					135 ± 6	194 ± 6
					NA	178 ± 10
					96 ± 6	174 ± 10
					NA	15 ± 4
					30 ± 4	14 ± 8

DMP FACTORY 500 – LT 60 ^{5,6,7,8}		TEST METHOD	METRIC		U.S.	
NHT	HAA		NHT	HAA	NHT	HAA
Ultimate Tensile Strength (MPa ksi)		ASTM E8				
Horizontal direction — XY			1080 ± 20	1520 -40/+20		
Vertical direction — Z			1010 ± 25	1440 -40/+20		
Yield strength Rp0.2% (MPa ksi)		ASTM E8				
Horizontal direction — XY			790 ± 25	1350 -40/+30		
Vertical direction — Z			660 ± 30	1280 ± 50		
Plastic elongation (%)		ASTM E8				
Horizontal direction — XY			29 ± 6	16 ± 4		
Vertical direction — Z			32 ± 4	18 ± 5		
					29 ± 6	16 ± 4
					32 ± 4	18 ± 5

HIGH TEMPERATURE TENSILE PROPERTIES DMP FACTORY 500 – LT60 ⁹		TEST METHOD	METRIC		U.S.	
NHT	HAA		NHT	HAA	NHT	HAA
Ultimate Tensile Strength (MPa ksi)						
Vertical direction – Z			NA	1185 ± 25		
Yield strength Rp0.2% (MPa ksi)		ASTM E21, at 650°C	NA	1055 ± 20		
Vertical direction – Z			NA	20 ± 3		
Plastic elongation (%)					NA	172 ± 4
Vertical direction – Z					NA	153 ± 3
					NA	20 ± 3

¹ Parts manufactured with standard parameters on a DMP Flex 350 and DMP Factory 350, Config B using layer thickness 30 µm and layer thickness 60 µm

² Values based on average and double standard deviation

³ NHT refers to non-heat-treated sample condition; HSAA refers to a modified homogenization followed with solutioning and double aging as prescribed in ASTM F3055

⁴ NHT samples tested according to ASTM E8M using round tensile test specimen type 4. HSAA samples tested according to ASTM E8 using rectangular tensile test specimen type 8

⁵ Parts manufactured with standard parameters on a DMP Factory 500, using layer thickness 60 µm (LT60)

⁶ Values based on average and 95% tolerance interval with 95% confidence

⁷ Tested according to ASTM E8 using round tensile test specimen type 4

⁸ NHT refers to non-heat-treated sample condition; HAA refers to the homogenization with double aging (HAA) heat treatment as prescribed in ASTM F3055

⁹ High temperature tensile properties based on limited sample size. For information only. Values based on average and double standard deviation

Printed Part Properties¹⁰

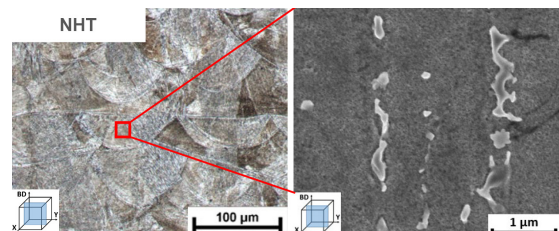
DENSITY	TEST METHOD	METRIC	U.S.
Theoretical density ¹¹ (g/cm ³ lb/in ³)	Value from literature	8.2	0.296
Relative density (%), DMP 350 ^{12, 13}	Optical method (pixel count)	≥ 99.6 Typical 99.9	≥ 99.6 Typical 99.9
Relative density (%), DMP 500 ^{12, 13}	Optical method (pixel count)	≥ 99.7 Typical 99.9	≥ 99.7 Typical 99.9
SURFACE ROUGHNESS R _a ^{12, 13, 14, 15}	TEST METHOD	METRIC	U.S.
Vertical side surface (µm µin) DMP 350	ISO 25178	Typically, around 5	Typically, around 197
Vertical side surface (µm µin) DMP 500	ISO 25178	Typically, around 5	Typically, around 197

Thermal Properties¹¹

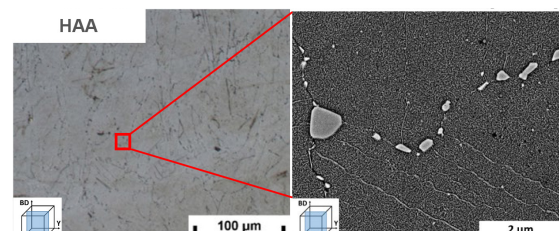
MEASUREMENT	CONDITION	METRIC	U.S.
Thermal conductivity (W/(m·K) BTU·in/h·ft ² ·°F)	At 21 °C / 69.8 °F	11.4	79
	At 100°C / 212°F	18.3	127
Coefficient of Thermal Expansion (µm/m·°C µinch/(inch·°F))	At 200°C / 392°F	13.2	7.33
	At 600°C / 1112°F	13.9	7.72
Melting range (°C °F)		1260-1335	2300-2435

Chemical Composition

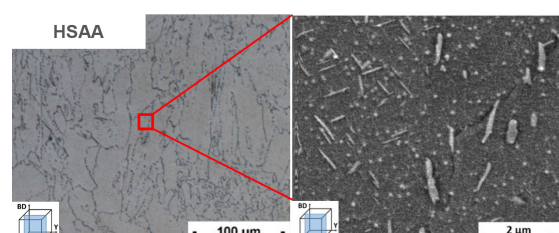
ELEMENT	% OF WEIGHT
Al	0.20-0.8
B	≤0.006
C	≤0.08
Co	≤1.00
Cr	17.00-21.00
Cu	≤0.30
Fe	Bal.
Mn,Si	≤0.35
Mo	2.80-3.30
Nb+Ta	4.75-5.50
Ni	50.00-55.00
P,S	≤0.015
Ti	0.65-1.15



Microstructure NHT



Microstructure after HAA



Microstructure after HSAA

¹⁰ May deviate depending on specific part geometry

¹¹ Values based on literature

¹² Parts manufactured with standard parameters on a DMP Flex and Factory 350, Config B using layer thickness 30 µm and 60 µm. Parts manufactured on a DMP Factory 500, using layer thickness 60 µm

¹³ Minimum values based on 95% tolerance interval with a 95% confidence. Tested on specific 3DS test coupons

¹⁴ Surface treatment performed with Finox zirconia blasting medium at 5 bar

¹⁵ Vertical side surface measurement along the building direction

Warranty/Disclaimer: The performance characteristics of these products may vary according to product application, operating conditions, or with end use. 3D Systems makes no warranties of any type, express or implied, including, but not limited to, the warranties of merchantability or fitness for a particular use.

©2021 by 3D Systems, Inc. All rights reserved. Specifications subject to change without notice. 3D Systems, the 3D Systems logo and ProX are registered trademarks of 3D Systems, Inc.





LaserForm® Ti Gr1 (A)

Commercially pure titanium fine-tuned for use with ProX® DMP 320 and DMP 350 printers; metal powder perfectly suited for medical applications and implants as LaserForm Ti Gr1 (A) is the purest Ti grade, known for its excellent biocompatibility and high ductility.

LaserForm Ti Gr1 (A) is formulated and fine-tuned specifically for 3D Systems ProX DMP 320 and DMP 350 metal 3D Printers to deliver highest part quality and best part properties. The print parameter database that 3D Systems provides together with the material has been extensively developed, tested and optimized in 3D Systems' part production facilities that hold the unique expertise of printing 500,000 challenging production parts year over year. Based on over 1000 test samples the below listed part quality data and mechanical properties give you high planning security. And for a 24/7 production 3D Systems' thorough Supplier Quality Management System guarantees consistent, monitored material quality for reliable process results.

Material Description

Commercially pure titanium is perfectly suited for medical applications because of its low stiffness and excellent biocompatibility. Grade 1 titanium is the most ductile medical titanium grade, rendering it ideal for implants, such as bone plates and other fixation devices, which need to be molded manually during surgery to fit the patient. Similar to other titanium grades, Grade 1 titanium has excellent corrosion resistance, including chloride and cavitation corrosion resistance.

Classification

Parts built with LaserForm Ti Gr1 Alloy have a chemical composition that complies with ASTM F3302, ASTM F67, ASTM B265, ASTM B348 (grade 1), ISO 5832-2, ISO 13782 and Werkstoff Nr. 3.7025 standards.

Mechanical Properties^{1,2,3}

MEASUREMENT	CONDITION	METRIC		U.S.	
		AFTER STRESS RELIEF 1	AFTER HIP	AFTER STRESS RELIEF 1	AFTER HIP
Youngs modulus (GPa ksi)	ASTM E8M	105-120	105-120	15000-17500	15000-17500
Ultimate Strength (MPa ksi)	ASTM E8M				
Horizontal direction — XY		500 ± 30	460 ± 30	73 ± 4	67 ± 4
Vertical direction — Z		500 ± 30	460 ± 30	73 ± 4	67 ± 4
Yield strength Rp0.2% (MPa ksi)	ASTM E8M				
Horizontal direction — XY		380 ± 30	340 ± 20	55 ± 4	49 ± 3
Vertical direction — Z		380 ± 30	340 ± 20	55 ± 4	49 ± 3
Elongation at break (%)	ASTM E8M				
Horizontal direction — XY		29 ± 5	36 ± 5	29 ± 5	36 ± 5
Vertical direction — Z		30 ± 5	36 ± 5	30 ± 5	36 ± 5
Reduction of area (%)	ASTM E8M				
Horizontal direction — XY		53 ± 5	58 ± 10	53 ± 5	58 ± 10
Vertical direction — Z		53 ± 6	60 ± 10	53 ± 6	60 ± 10
Hardness, Rockwell B (HRB)	ASTM E18	85 ± 5	80 ± 5	85 ± 5	80 ± 5

Thermal Properties⁴

MEASUREMENT	CONDITION	METRIC	U.S.
Thermal conductivity (W/(m.K) btu.in/(h.ft.°F))	At 50 °C / 120 °F	16	9.25
Coefficient of Thermal Expansion (µm/m.°C µin/(in.°F))	In the range of 20 to 600 °C	7.17	3.98
Melting point (°C °F)		1668	3070

¹ Parts manufactured with standard parameters on a ProX DMP 320, Config A

² Values based on average and double standard deviation

³ Surface condition of test samples: Horizontal samples (XY) tested in machined surface condition only, vertical (Z) tested in as-printed and machined surface condition

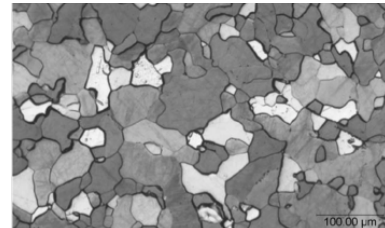
⁴ Values based on literature



LaserForm® Ti Gr1 (A)

Physical Properties

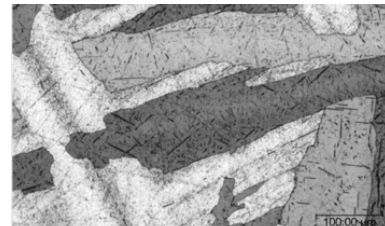
MEASUREMENT	CONDITION	METRIC		U.S.	
		AS BUILT AND AFTER STRESS RELIEF	AFTER HIP	AS BUILT AND AFTER STRESS RELIEF	AFTER HIP
Density — Relative, based on pixelcount (%) ^{1,2}	Optical method	> 99.6 typical 99.8		> 99.6 typical 99.8	
Density — Absolute theoretical ³ (g/cm ³ lb/in ³)		4.51		0.163	



Microstructure after stress relief 1

Surface Quality^{4,5}

MEASUREMENT	CONDITION	METRIC		U.S.	
		SANDBLASTED	SANDBLASTED	SANDBLASTED	SANDBLASTED
Surface Roughness Ra Top surface ⁶ (μm μin)	ISO 25178	4.8		160-310	
Vertical side surface ⁷ (μm μin)		4.8		160-310	



Microstructure after HIP

Chemical Composition

Ti	Bal.
N	≤0.03
C	≤0.08
H	≤0.015
Fe	≤0.20
O	≤0.18
Residuals (each)	≤0.1
Residuals (total)	≤0.4

¹ Minimum value based on 95% confidence interval
Tested on typical density test shapes

² May deviate depending on specific part geometry

³ Values based on literature

⁴ Parts manufactured with standard parameters on a ProX DMP 320, Config A

⁵ Sand blasting performed with zirconia blasting medium at 2 bar

⁶ Top surface measurements along the 2 perpendicular axes of the reference square geometry

⁷ Vertical side surface measurement along the building direction

3D SYSTEMS®

www.3dsystems.com

Warranty/Disclaimer: The performance characteristics of these products may vary according to product application, operating conditions, or with end use. 3D Systems makes no warranties of any type, express or implied, including, but not limited to, the warranties of merchantability or fitness for a particular use.

©2020 by 3D Systems, Inc. All rights reserved. Specifications subject to change without notice. 3D Systems, the 3D Systems logo, ProX and LaserForm are registered trademarks of 3D Systems, Inc.



LaserForm® Ti Gr5 (A)

Titanium alloy fine-tuned for use with ProX® DMP 320 and DMP 350 metal printers. This alloy is used in technical and medical applications because of its high strength, low density and excellent biocompatibility. The essential difference between Ti6Al4V ELI (grade 23) and Ti6Al4V (grade 5) is the allowed higher oxygen and iron content in Ti Gr5. This confers improved strength.

LaserForm Ti Gr5 (A) is formulated and fine-tuned specifically for 3D Systems ProX DMP 320 and DMP 350 metal 3D printers to deliver highest part quality and best part properties. The print parameter database that 3D Systems provides together with the material has been extensively developed, tested and optimized in 3D Systems' part production facilities that hold the unique expertise of printing 500,000 challenging production parts year over year. Based on over 1000 test samples the below listed part quality data and mechanical properties give you high planning security. And for a 24/7 production 3D Systems' thorough Supplier Quality Management System guarantees consistent, monitored material quality for reliable process results.

Material Description

This titanium alloy is commonly used for lightweight and high-strength components such as aerospace and motor sports applications. Because of its excellent biocompatibility Ti Gr5 (A) is also very well suited for medical implants, tools and devices and dental prostheses. The essential difference between Ti6Al4V ELI (grade 23) and Ti6Al4V (grade 5) is the allowed higher oxygen and iron content in Ti Gr5. This confers improved strength while slightly reducing ductility.

These benefits make LaserForm Ti Gr5 (A) the ideal material for light-weight, high-strength components as required for a broad scope of parts in aerospace, sports and marine products. Its high strength and biocompatibility make it the material of choice for medical tools and devices.

Classification

Parts built with LaserForm Ti Gr5 Alloy have a chemical composition that meets the requirements of ASTM B265, B348 (grade 5), F2924, F3302, ISO 5832-3 and Werkstoff Nr. 3.7165.

Mechanical Properties^{1,2,3}

MEASUREMENT	CONDITION	METRIC		U.S.	
		AFTER STRESS RELIEF 1	AFTER HIP	AFTER STRESS RELIEF 1	AFTER HIP
Youngs modulus (GPa ksi) ⁴	ASTM E8M	105-120	105-120	15000-17500	15000-17500
Ultimate strength (MPa ksi)	ASTM E8M				
Horizontal direction — XY		1180 ± 30	1000 ± 30	171 ± 5	145 ± 4
Vertical direction — Z		1160 ± 50	1020 ± 50	168 ± 8	148 ± 8
Yield strength Rp.0.2% (MPa ksi)	ASTM E8M				
Horizontal direction — XY		1090 ± 30	910 ± 30	158 ± 5	132 ± 5
Vertical direction — Z		1080 ± 50	930 ± 30	157 ± 8	134 ± 5
Elongation at break (%)	ASTM E8M				
Horizontal direction — XY		9 ± 2	15 ± 3	9 ± 2	15 ± 3
Vertical direction — Z		9 ± 2	14 ± 3	9 ± 2	14 ± 3
Hardness, Rockwell C (HRC)	ASTM E18	40 ± 2	36 ± 2	40 ± 2	36 ± 2

Thermal Properties⁴

MEASUREMENT	CONDITION	METRIC	U.S.
Thermal conductivity (W/(m.K) Btu in/(h.ft.°F)	At 50 °C/ 120 °F	6.7	3.9
Coefficient of thermal expansion (µm/m·°C / µin/(in.·°F)	In the range of 20 to 100 °C	8.6	4.8
Melting range (°C °F)		1692-1698	3046-3056

¹ Parts manufactured with standard parameters on a ProX DMP 320, Config A

² Values based on average and double standard deviation

³ Surface condition of test samples: Horizontal samples (XY) tested in machined surface condition only, vertical (Z) tested in as-printed and machined surface condition

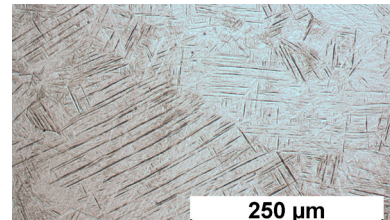
⁴ Values based on literature



LaserForm® Ti Gr5 (A)

Physical Properties

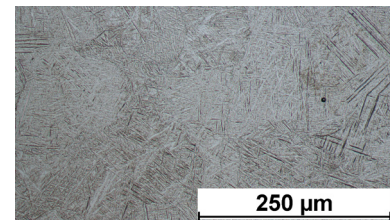
MEASUREMENT	CONDITION	METRIC		U.S.	
		AS BUILT AND AFTER STRESS RELIEF	AFTER HIP	AS BUILT AND AFTER STRESS	AFTER HIP
Density — Relative, based on pixelcount ^{1,2} (%)	Optical method	> 99.6 typical 99.8		> 99.6 typical 99.8	
Density — Absolute theoretical ³ (g/cm ³ lb/in ³)			4.42		0.159



Microstructure as built

Surface Quality

MEASUREMENT	CONDITION	SANDBLASTED METRIC	SANDBLASTED U.S.
Surface Roughness R _a ^{4,5}	ISO 25178		
Layer thickness 30μm and 60μm Top surface ⁶ (μm μin) Vertical side surface ⁷ (μm μin)		typical 3-8 typical 5-7	typical 120-320 typical 200-280
Layer thickness 90μm Top surface ⁶ (μm μin) Vertical side surface ⁷ (μm μin)		typical 13-19 typical 6-12	typical 500-750 typical 240-480



Microstructure after stress relief

Chemical Composition

Ti	bal.
N	≤0.05
C	≤0.08
H	≤0.015
Fe	≤0.30
O	≤0.20
Al	5.50-6.75
V	3.50-4.50
Y	≤0.005
residuals each	≤0.10
residuals total	≤0.40



www.3dsystems.com

¹ Minimum value based on 95% confidence interval. Tested on typical density test coupons

² May deviate depending on specific part geometry

³ Values based on literature

⁴ Parts manufactured with standard parameters on a ProX DMP 320, Config A

⁵ Sand blasting performed with zirconia blasting medium at 5 bar

⁶ Top surface measurements along the 2 perpendicular axes of the reference square geometry

⁷ Vertical side surface measurement along the building direction

Warranty/Disclaimer: The performance characteristics of these products may vary according to product application, operating conditions, or with end use. 3D Systems makes no warranties of any type, express or implied, including, but not limited to, the warranties of merchantability or fitness for a particular use.

©2020 by 3D Systems, Inc. All rights reserved. Specifications subject to change without notice. 3D Systems, the 3D Systems logo, ProX and LaserForm are registered trademarks of 3D Systems, Inc.



LaserForm® Ti Gr23 (A)

Titanium alloy fine-tuned for use with ProX® DMP 320 and DMP 350 metal printers. Metal powder producing technical and medical parts with a combination of high specific strength and excellent biocompatibility.
LaserForm Ti Gr23 (A) is ELI (Extra Low Interstitial) grade with lower iron, carbon, and oxygen content and is known for higher purity than LaserForm Ti Gr5 (A) resulting in improved ductility and fracture toughness.

LaserForm Ti Gr23 (A) is formulated and fine-tuned specifically for 3D Systems' ProX DMP 320 and DMP 350 metal 3D printers to deliver highest part quality and best part properties. The print parameter database that 3D Systems provides together with the material has been extensively developed, tested and optimized in 3D Systems' part production facilities that hold the unique expertise of printing 500,000 challenging production parts year over year. Based on over 1000 test samples the below listed part quality data and mechanical properties give you high planning security. And for a 24/7 production 3D Systems' thorough Supplier Quality Management System guarantees consistent, monitored material quality for reliable process results.

Mechanical Properties^{1,2,3}

MEASUREMENT	CONDITION	METRIC		U.S.		
		AFTER STRESS RELIEF 1	AFTER STRESS RELIEF 2	AFTER HIP	AFTER STRESS RELIEF 1	AFTER STRESS RELIEF 2
Youngs modulus (GPa ksi) Horizontal direction — XY Vertical direction — Z	ASTM E1876	119 ± 3 120 ± 1	119 ± 3 120 ± 1	122 ± 2 NA	17300 ± 730 17400 ± 300	17300 ± 730 17400 ± 300
Ultimate Strength (MPa ksi) Horizontal direction — XY Vertical direction — Z	ASTM E8M	1160 ± 20 1170 ± 50	1070 ± 30 1070 ± 30	980 ± 50 980 ± 70	168 ± 3 170 ± 7	155 ± 4 155 ± 4
Yield strength Rp0.2% (MPa ksi) Horizontal direction — XY Vertical direction — Z	ASTM E8M	1060 ± 30 1100 ± 60	970 ± 30 1000 ± 60	890 ± 50 890 ± 90	154 ± 4 160 ± 9	141 ± 4 145 ± 9
Plastic elongation (%) Horizontal direction — XY Vertical direction — Z	ASTM E8M	10 ± 2 10 ± 3	13 ± 2 13 ± 3	14 ± 2 14 ± 2	10 ± 2 10 ± 3	13 ± 2 13 ± 3
Reduction of area (%) Horizontal direction — XY Vertical direction — Z	ASTM E8M	35 ± 10 40 ± 10	45 ± 10 45 ± 15	45 ± 5 45 ± 5	35 ± 10 40 ± 10	45 ± 10 45 ± 15
Hardness, Rockwell C	ASTM E18	37 ± 2	37 ± 4	34 ± 1	37 ± 2	37 ± 4
Fatigue ^{4,5} (MPa ksi)	ASTM E466	NA	typical 637	NA	NA	typical 92

Thermal Properties

MEASUREMENT	CONDITION	METRIC	U.S.
Thermal conductivity ⁶ (W/(m.K) Btu in/(h.ft.°F))	At 20 °C / 68 °F	4.2 ± 0.1	29 ± 1
Coefficient of thermal expansion ⁷ (µm/(m.°C) µ inch/(inch.°F))	In the range of 20 to 600 °C	8.6	4.8
Melting range ⁷ (°C °F)		1692-1698	3046-3056

¹ Parts manufactured with standard parameters on a ProX DMP 320, Config A

² Values based on average and double standard deviation

³ Surface condition of test samples: Horizontal samples (XY) tested in machined surface condition only, vertical (Z) tested in as-printed and machined surface condition

⁴ Force-controlled axial fatigue testing (R=0.1). Endurance limit at 5 x 10⁶ cycles Fatigue samples with machined surface

⁵ Results are based on limited sample size, not statistically representative

⁶ Thermal conductivity values are calculated by the Wiedemann-Franz law using the respective electrical resistivity values

⁷ Values based on literature



Electrical Properties

MEASUREMENT	CONDITION	METRIC	U.S.
Electrical conductivity ^{1,2} (10^5 S/m)	ASTM B193 at 20°C / 68°F	5.9 ± 0.1	5.9 ± 0.1

Physical Properties

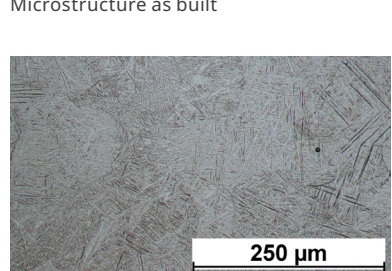
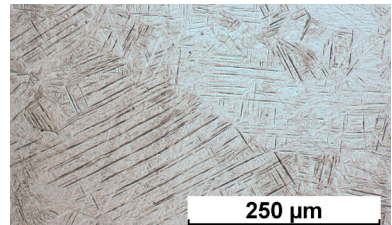
MEASUREMENT	CONDITION	METRIC	U.S.
		AS BUILT	AS BUILT
Density — Relative, based on pixel count ^{3,4} (%)	Optical method	> 99.6 typical 99.8	> 99.6 typical 99.8
Density — Absolute theoretical ⁵ (g/cm ³ lb/in ³)		4.42	0.16

Surface Quality^{6,7,8}

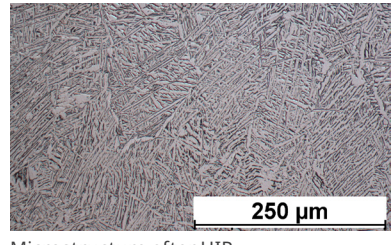
MEASUREMENT	CONDITION	METRIC	U.S.
		SANDBLASTED	SANDBLASTED
Surface Roughness R _a	ISO 25178		
Layer thickness 30µm and 60µm Top surface ⁹ (µm µin) Vertical side surface ¹⁰ (µm µin)		typical 3-8 typical 5-7	typical 120-320 typical 200-280
Layer thickness 90µm Top surface ⁹ (µm µin) Vertical side surface ¹⁰ (µm µin)		typical 13-19 typical 6-12	typical 500-750 typical 240-480

Chemical Composition

ELEMENT	% OF WEIGHT
Ti	Bal.
N	≤0.03
C	≤0.08
H	≤0.012
Fe	≤0.25
O	≤0.13
Al	5.5 - 6.5
V	3.5 - 4.5
Y	≤0.005
Residuals (each)	≤0.1
Residuals (total)	≤0.4



Microstructure after stress relief 2



Microstructure after HIP



www.3dsystems.com

¹ Electrical resistivity measurements are based on four point contact method according to ASTM B193

² Results are based on limited sample size, not statistically representative

³ Minimum value based on 95% confidence interval. Tested on typical density test shapes

⁴ May deviate depending on specific part geometry

⁵ Values based on literature

⁶ Parts manufactured with standard parameters on a ProX DMP 320, Config A

⁷ Values based on average and double standard deviation

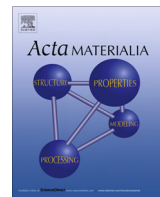
⁸ Sand blasting performed with zirconia blasting medium at 5 bar

⁹ Top surface measurements along the 2 perpendicular axes of the reference square geometry

¹⁰ Vertical side surface measurement along the building direction

Warranty/Disclaimer: The performance characteristics of these products may vary according to product application, operating conditions, or with end use. 3D Systems makes no warranties of any type, express or implied, including, but not limited to, the warranties of merchantability or fitness for a particular use.

©2020 by 3D Systems, Inc. All rights reserved. Specifications subject to change without notice. 3D Systems, the 3D Systems logo, ProX and LaserForm are registered trademarks of 3D Systems, Inc.



Graded microstructure and mechanical properties of additive manufactured Ti–6Al–4V via electron beam melting



Xipeng Tan ^{a,*}, Yihong Kok ^a, Yu Jun Tan ^a, Marion Descoins ^b, Dominique Mangelinck ^b, Shu Beng Tor ^{a,*}, Kah Fai Leong ^a, Chee Kai Chua ^a

^a Singapore Centre for 3D Printing, School of Mechanical and Aerospace Engineering, Nanyang Technological University, HW1-01-05, 2A Nanyang Link, Singapore 637372, Singapore
^b IM2NP, UMR 7334 CNRS, Université Aix-Marseille, 13397 Marseille Cedex 20, France

ARTICLE INFO

Article history:

Received 7 April 2015

Revised 15 June 2015

Accepted 16 June 2015

Available online 24 June 2015

Keywords:

3D printing

Electron beam melting

Titanium alloy

Gradient

Microstructure formation mechanism

Atom probe tomography

ABSTRACT

Electron beam melting (EBM[®])-built Ti–6Al–4V has increasingly shown great potential for orthopedic implant and aerospace applications in recent years. The microstructure and mechanical properties of EBM-built Ti–6Al–4V have been systematically investigated in this work. Its microstructure consists of columnar prior β grains delineated by wavy grain boundary α and transformed α/β structures with both cellular colony and basket-weave morphology as well as numerous singular α bulges within the prior β grains. The β phase is found to form as discrete flat rods embedded in continuous α phase and its volume fraction is determined to be $\sim 3.6\%$. Moreover, α' martensite was not observed as it has decomposed into α and β phases. In particular, the α/β interface was studied in detail combined transmission electron microscopy with atom probe tomography. Of note is that graded Ti–6Al–4V microstructure i.e. both prior β grain width and β phase interspacing continuously increase with the build height, was observed, which mainly arises from the decreasing cooling rate. Furthermore, an increasingly pronounced strain hardening effect was also observed as the previously built layers undergo a longer annealing compared to the subsequent layers. As a result, graded mechanical properties of Ti–6Al–4V with degraded microhardness and tensile properties were found. A good agreement with the Hall–Petch relation indicates that the graded property takes place mainly due to the graded microstructure. In addition, this graded microstructure and mechanical properties were discussed based on a quantitative characterization.

© 2015 Acta Materialia Inc. Published by Elsevier Ltd. All rights reserved.

1. Introduction

Additive manufacturing (AM), commonly known as 3D printing, is a process of joining materials to make objects from 3D model data, usually layer upon layer, as opposed to subtractive manufacturing methodologies [1]. In recent years, AM processes have been recognized as attractive techniques for producing prototypes or finalized parts rapidly and cost-effectively, correspondingly they were termed “rapid prototyping” or “rapid manufacturing” [2]. Electron beam melting (EBM[®]) is an AM technique which was made commercially available quite recently, using a high-energy electron beam to selectively melt a conductive metal powder bed directed by a computer aided design (CAD) model under a high vacuum. EBM is capable of producing fully dense, near-net-shape complex parts with high mechanical properties [3].

Ti–6Al–4V is the most prevalent titanium alloy and one of the most important engineering materials. Due to its high

strength-to-weight ratio, good biocompatibility and outstanding corrosion resistance, Ti–6Al–4V has been widely used in aerospace, biomedical implants, marine and offshore, etc. [4]. Ti–6Al–4V is a typical α (hcp: hexagonal close-packed) + β (bcc: body-centered cubic) dual-phase alloy, where α phase normally precipitates in β matrix with the classic Burgers relationship: $(0001)_\alpha//(110)_\beta$, $[11\bar{2}0]_\alpha//[111]_\beta$. Aluminum is added to increase the strength of the alloy by solid solution hardening and α stabilization. Vanadium addition stabilizes β which significantly improves the room temperature ductility, by achieving balanced mechanical properties from duplex α/β microstructure. The duplex microstructure usually consists of numerous lamellar colonies composed of alternating layers of acicular α and thin layers of retained β , which gives rise to a combination of attractive mechanical properties such as high strength and good ductility [5]. Of particular interest is the so-called “interface phase” or “interfacial layer” which occur under certain conditions at the α/β interfaces in the two-phase titanium alloys [6,7]. Previous work indicates that the interface phase width in Ti–6Al–4V will increase with decreasing cooling rate and can be varied from 50 nm to 450 nm. The interface phase

* Corresponding authors.

E-mail addresses: xptan1985@gmail.com (X. Tan), msbtor@ntu.edu.sg (S.B. Tor).

was previously identified as an intermediate transition phase with a face-centered cubic (fcc) or hcp structure formed during the β to α transformation, probably as a result of sluggish diffusion of β stabilizer such as vanadium [8]. However, it was argued that it is an artifact and consists of a titanium hydride formed during thin foil preparation for TEM examination [9]. The α/β interface phase has been extensively studied by using transmission electron microscope (TEM) over the past decades. Nevertheless, it is still a controversy on the nature of this interface phase or interface layer [10]. More recently, a grain boundary α - β - α layered structure was observed under TEM mode in a sintered Ti-6Al-4V, and its formation was explained as a result of a high O content of 0.49 wt.% [11]. Its morphology appears to be very similar with the interfacial layer that often found in α/β duplex titanium alloys. The α/β interface phase has been shown to be a significant factor in the tensile or fatigue fracture of two-phase Ti-6Al-4V alloy, because it may provide an easy crack path or crack initiation sites [8]. Therefore, it is very necessary to investigate this particular interface phase in order to obtain a better understanding of the $\alpha \leftrightarrow \beta$ phase transformation. Atom probe tomography (APT) is the unique and powerful technique, which is able to locate the alloying elements and quantify the composition at the atomic scale and in the three dimensions. In particular, APT is specialized in analysis of interphase interfaces in a wide variety of materials [12].

EBM is a preferred AM technique for fabricating Ti-6Al-4V parts because of titanium's high affinity for oxygen. Due to its broad application prospect in orthopedic implant and aerospace industries, Ti-6Al-4V parts built by EBM has been most investigated till date. The microstructure of Ti-6Al-4V fabricated by EBM consists of columnar prior β grains delineated by grain boundary α and a transformed $\alpha + \beta$ structure with both colony and basket-weave (or Widmanstätten) morphology within the prior β grains [13,14]. The columnar β grains formed due to the extreme solidification conditions (e.g. high thermal gradient and rapid solidification rate in the small melt pool) and the strong partitioning behavior of the main alloying elements in Ti-6Al-4V. They will grow epitaxially along the <001> build direction as a pseudo-uniaxial heat transfer direction occurs [15]. The retained β phase was found to be rod-like and its volume fraction was calculated to be only ~2.7% [16]. Moreover, numerous spherical or even irregular pores can be observed in EBM-built samples either as a result of the entrapped argon during the production of gas-atomized Ti-6Al-4V powder [16] or an insufficient melting around the interface between in-fill hatch and contour [14,17]. In addition to the typical α/β duplex microstructure that stated above, the presence of α' martensite was also reported either in short builds, thin-wall structures or net structures of EBM-fabricated Ti-6Al-4V [13,18,19]. As a thermal cycling of rapid solidification, high cooling in solid state and long-term annealing at a build temperature of ~600–650 °C is involved layer by layer during the entire EBM process, an out-of-equilibrium, very fine, and build space- and geometry-dependent microstructure will be obtained in the as-built materials. It is thus easy to imagine that graded microstructure as well as the resulting graded properties would appear in EBM-built Ti-6Al-4V parts. Murr et al. [20] reported earlier that there existed significant differences on α platelet thickness (e.g. 1.6 μm and 3.2 μm at the bottom and the top, respectively) in microstructure and the corresponding hardness (42 HV and 37 HV) within a dimensional range of ~40 mm build height in EBM-built cylindrical Ti-6Al-4V samples. However, Hrabe et al. [21] pointed out that there was no difference on microstructure and mechanical properties with varying build height in EBM-built parts with a total build height of 27 mm. Ladani et al. [22] studied the mechanical anisotropy of EBM-built parts. It suggests that the flat-built (X-orientated) net-shaped specimens have superior tensile strength and microhardness compared

to the other two build directions. It is imperative for any AM parts to have consistent microstructure and properties throughout, particularly for critical load bearing components. Overall, the published works on the microstructural consistency of EBM-built Ti-6Al-4V parts are very limited.

It has been reported that the tensile properties of EBM-built Ti-6Al-4V are comparable to wrought form and better than that of cast form [3]. However, it is still not extensively studied regarding the high strength and good ductility that are achieved in as-built EBM parts. It is worth noting that the α/β duplex microstructure of EBM-built Ti-6Al-4V has not yet been characterized in detail, particularly on the structure of α/β interface and the elemental segregation behavior at α/β interface. In order to elucidate the microstructure–property relationship from the viewpoint of atomic scale, APT was employed for α/β interface analysis in this work. Furthermore, the paper provides a quantitative composition and crystallography analysis of the microstructure of EBM-built Ti-6Al-4V, and discusses its microstructural evolution under such a complex process in detail.

2. Experimental

All test samples were fabricated by an Arcam A2XX system (as schematically shown in Fig. 1a) using the standard processing themes provided by Arcam AB. Pre-alloyed Ti-6Al-4V ELI (Grade 23) powder supplied by Arcam AB was used for the evaluation of graded microstructure and mechanical properties. The perfectly spherical morphology and clean surface of each powder are revealed in Fig. 1b–d, indicating good flowability and no oxidation. The powder size ranges from 45 to 105 μm . The nominal composition of as-supplied powders is 6Al-4V-0.03C-0.1Fe-0.15O-0.01N-0.003H and Ti Bal. (wt.%). Two build themes were employed in this work, i.e. Ti6Al4V-PreHeat-50 μm and Ti6Al4V-melt-50 μm . A 10 mm-thick stainless steel start plate is heated by the electron beam when a pressure of ~5.0e–4 mBar within the build chamber is achieved. Once a bottom temperature of 730 °C is reached, parts are built directly onto the preheated start plate by selectively melting layers of 50 μm under a controlled vacuum in the temperature range of 600–650 °C. The entire building process was kept under a vacuum of ~2.0e–3 mBar, controlled by using high-purity helium as regulating gas in order to prevent powder charging. Recycling of non-melted and/or sintered powder was achieved via the powder recovery system (PRS) and a vibrating sieve (mesh size $\leq 150 \mu\text{m}$). In order to investigate the consistency of microstructure and mechanical properties of EBM-built parts, two horizontal blocks (100 mm × 10 mm × 30 mm) were fabricated. Four tensile testpieces were wire-cut one-by-one from a horizontal block. They are termed 10 mm-1, 10 mm-2, 10 mm-3 and 10 mm-4 from bottom to top (as illustrated in Fig. 2).

Optical microscopy (OM; ZEISS Axioskop 2 MAT), scanning electron microscopy (SEM; JEOL JMS-6700F; 10 kV), X-ray diffraction (XRD; PANalytical Empyrean; Cu K α ; step size of 0.01°) and transmission electron microscopy (TEM; JEOL-2010; 200 kV) were used to examine the microstructure of as-built Ti-6Al-4V. OM and SEM samples were etched in Kroll's reagent (1–3% HF, 2–6% HNO₃, and 91–97% H₂O) for 10 s. Quantitative image analysis was carried out by using Image J software. TEM samples were prepared using ion milling with a beam voltage of 3.5 kV and a milling angle of 4–8°. Phase identification was carried out by means of XRD and selected area electron diffraction (SAED). APT specimens were prepared by focused ion beam (FIB) on a FEI Helios dual-beam via the lift-out technique [23]. The micro-tips were prepared using the annular milling method [24] to obtain an end radius of ~50 nm. APT specimens were analyzed by laser-pulsed local-electrode atom probe LEAP® 3000X HR at 40 K and a gauge pressure

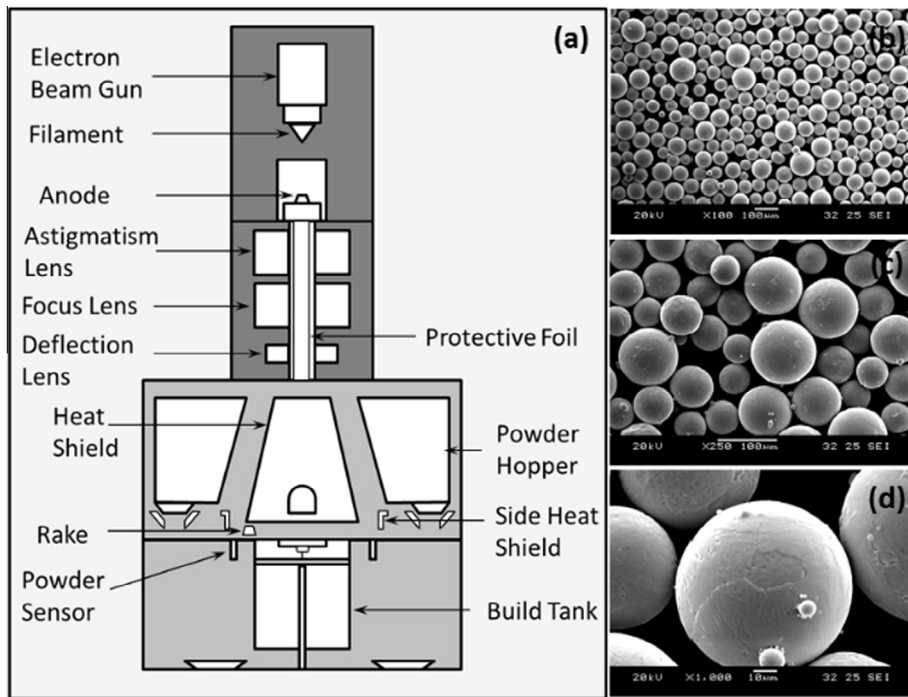


Fig. 1. (a) Schematic of EBM system. (b), (c), and (d) SEM images showing Ti-6Al-4V ELI powder with different magnifications.

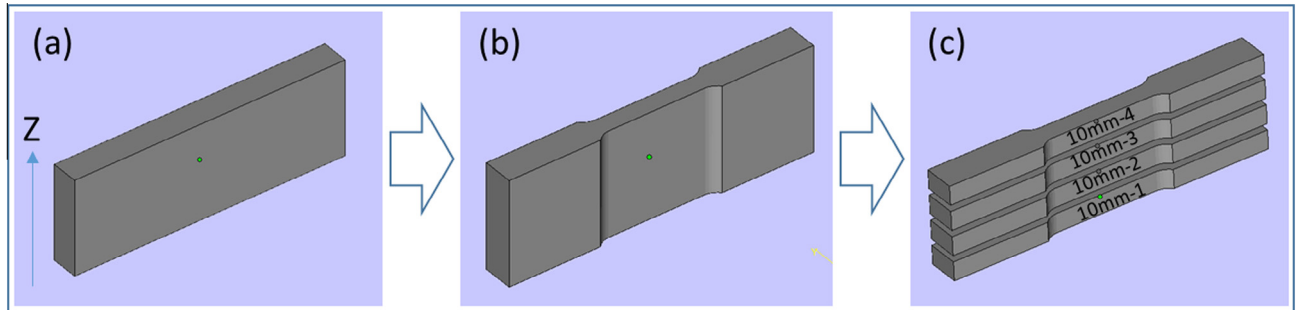


Fig. 2. (a) Schematic illustration of the horizontal Ti-6Al-4V ELI block ($100\text{ mm} \times 10\text{ mm} \times 30\text{ mm}$) built by EBM. (b) Machinery of the block into standard tensile testpieces. (c) Layout of the four tensile testpieces. The build direction is indicated by an arrow.

<2.0e-11 Torr. Pulses of green laser light (532 nm wavelength) were applied at a 200 kHz repetition rate with an energy of 0.9 nJ pulse⁻¹ and an evaporation rate of 0.30%. Data analysis was performed using IVAS® 3.6.2 software and compositional information was obtained by employing the proximity histogram (proxigram) methodology [25]. Errors bars were plotted in each compositional profile. The error bars were calculated using the equation:

$$\text{Error}\% = \pm \sqrt{C * (100 - C)} / N \quad (1)$$

where C is the composition value in at.% and N is the number of atoms in the distance step over which these values were being averaged [26].

Tensile tests were performed on Instron Static Tester (series 5569) using subsize specimens with a gauge dimension of 25 mm × 6 mm × 6 mm according to ASTM E8 standard at a strain rate of 3.33e-4 s⁻¹. Yield strength (YS, 0.2% offset method), elongation at break (% EL) and ultimate tensile strength (UTS) were measured from the engineering stress-strain curves. Vickers microhardness (HV) (1 kg f, 15 s hold) measurements were conducted on the metallographic samples using a Future Tech

FM-300e microhardness tester. At least 5 microhardness measurements were performed for each sample.

3. Results

3.1. Phase identification and microstructure

Fig. 3 shows the XRD peaks of EBM-built Ti-6Al-4V sample taken from the 10 mm-thick block in Fig. 2a. From Safdar et al. [16], it is known that most of the peaks originates from α phase. Only a weak (110) peak of β phase could be observed after zooming in, which indicates that a very small amount of β phase retained in the final microstructure. It is thus confirmed that the microstructure of EBM-built Ti-6Al-4V mainly consists of α and β phases. The lattice constants of hcp α phase in the EBM-built Ti-6Al-4V can be determined to be $a = 0.293\text{ nm}$ and $c = 0.467\text{ nm}$ respectively, with c/a ratio of 1.595. For the bcc β phase $a = 0.320\text{ nm}$. Fig. 5a shows the wavy columnar prior β grains that delineated by grain boundary α phase. The wavy grain boundaries formed because in-fill hatch melting direction rotated 90° after each layer during EBM process, which aims to minimize

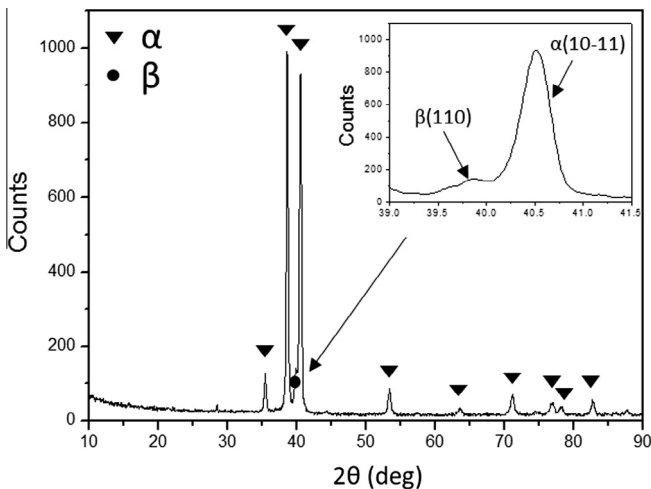


Fig. 3. XRD pattern for EBM-built Ti-6Al-4V horizontal block sample.

residual stress. It is noted that a lot of black lines can be clearly seen inside the prior β grains in Fig. 4a. After a detailed observation using OM and SEM, they were found to be the singular α bulges with a $\beta/\alpha/\beta$ sandwich structure (revealed in Fig. 4b and c). The width of these columnar β grains mainly ranges from 10 μm to 100 μm . Fig. 4d shows a typical α/β duplex microstructure. As α phase was etched out by Kroll's reagent, it exhibits dark contrast while β is in bright under SEM mode. In general, there are two sorts of transformed α/β structures existed inside the prior β grain, i.e. lamellar colony (Fig. 4e) and basket-weave (also called Widmanstätten pattern in Fig. 4f) morphology. It is of interest to note that β phase was found to be rod-like in the whole volume. The volume fraction of retained β phase was calculated as only $\sim 5\%$ in terms of the image analysis results. As its volume fraction is quite low, i.e. far less than 50%, as well as its growth obeys the Burgers relationship, β phase formed as discrete flat rods that

embedded in the continuous α phase. To be more precise, it should be the colonies with a cellular morphology instead of the lamellar structure in Fig. 4e. The thickness of rod-like β phase was measured as ~ 50 nm in SEM images. Furthermore, TEM techniques were employed to identify phases and investigate the sub-microstructures in EBM-built Ti-6Al-4V. Fig. 5 shows that numerous micro-twins exist inside α phase. It is noted that a suspected interface layer between α and β phases could be evidently seen in Fig. 5c. Moreover, it was found to be prevalent in all of our EBM-built Ti-6Al-4V parts. This interface layer appears to be quite similar with the α/β interface phase observed in the previous studies [6–8]. The difference is that the interface layer was not located symmetrically on both sides of β phase. SAED results demonstrate that it is the L phase with an fcc crystal structure of $a = 0.441$ nm [10].

In order to quantitatively study the α/β interface, APT was used to analyze the specimen cut from the EBM-built Ti-6Al-4V block in Fig. 2a. According to the mass-to-charge spectrum illustrated in Fig. 6, the form of the interstitial elements, e.g. O, Fe, N, C, H etc. that exist in the initial pre-alloyed powder could be directly known. O mainly exists as TiO and it also combine with Al and H to form AlO and H_2O . Otherwise, the H_2O detected in Fig. 6 might also be from the absorbed moisture. Fe and C will not react with other elements. N can exist either as element or compound of TiN and Ti_2N . H exists in the form of TiH and VH but it may mainly come from the analysis chamber of APT. Fig. 7a shows a micro-tip specimen prepared by using FIB for APT analysis. The APT reconstruction volume shown in Fig. 7b was obtained from the apex of this micro-tip. For clarity, only three major elements, i.e. Ti, Al and V, were illustrated. As known, Al can stabilize α phase while V is a β stabilizer [5]. Moreover, it has been stated above that the microstructure of EBM-built Ti-6Al-4V consists of fine β rods embedded into continuous α phase. Therefore, α and β phases could be indicated respectively in Fig. 7b. Al and V are two major alloying elements in Ti-6Al-4V; meanwhile they exhibit obvious partitioning behavior as shown in Fig. 7d and e, i.e. Al preferentially partitions to α phase while more V enters β phase. In addition

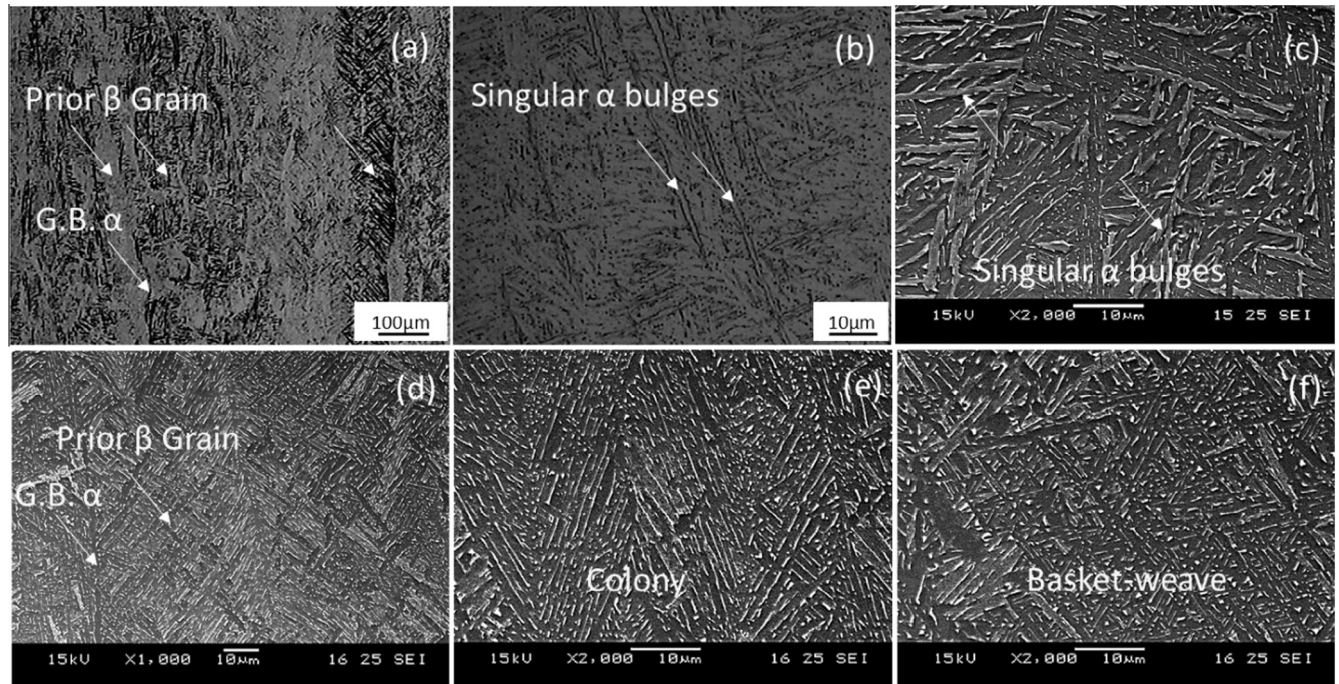


Fig. 4. OM images showing (a) wavy columnar prior β grains and (b) singular α bulges. The corresponding SEM images showing (c) singular α bulges in (b) and (d) columnar prior β grains in (a). SEM images showing transformed $\alpha + \beta$ microstructure with (e) colony and (f) basket-weave morphology.

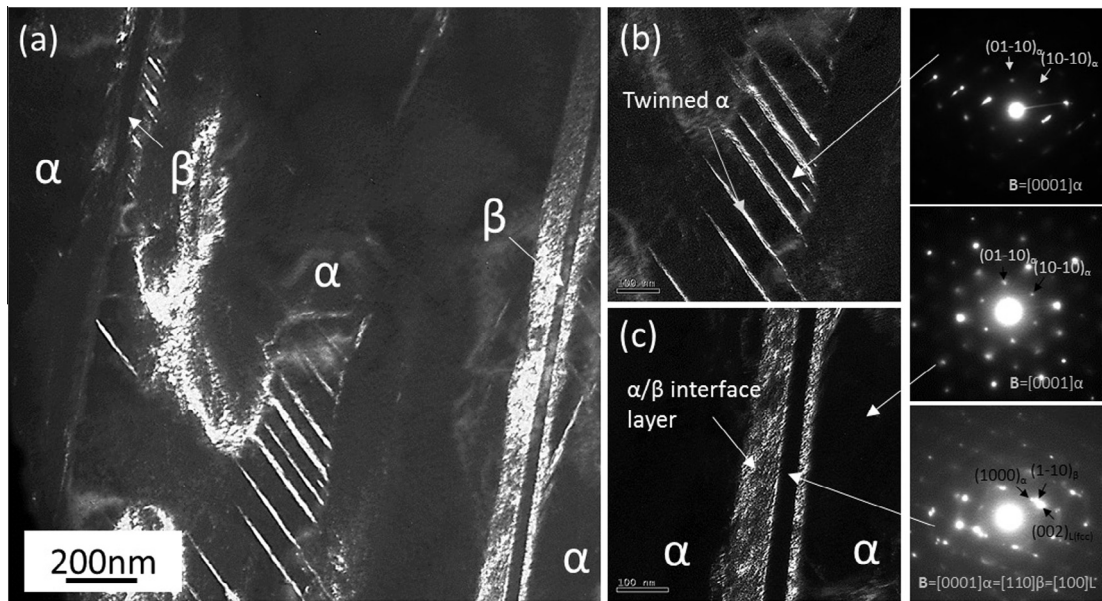


Fig. 5. (a) TEM dark field (DF) image showing α and β phases. (b) and (c) Enlarged DF images showing micro-twins in α phase and a suspected α/β interface layer, respectively. Insets indicate the SAED patterns with zone axis $[0001]_{\alpha}$ and $[001]_{\beta}$.

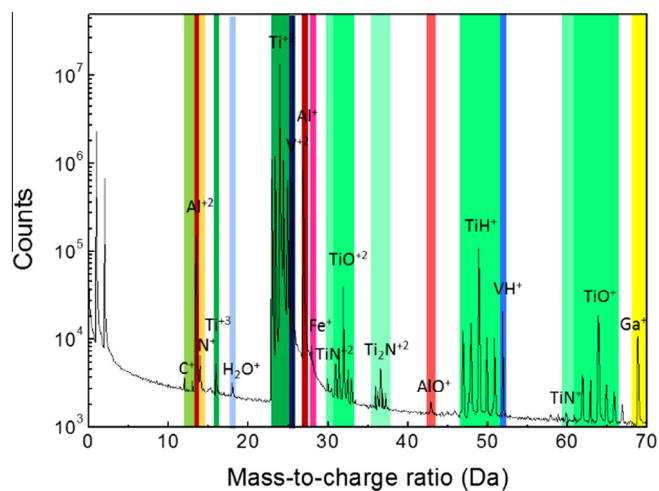


Fig. 6. Mass-to-charge spectrum of an APT reconstruction volume showing the ions or complex ions detected in the sample of EBM-built Ti-6Al-4V.

to Al and V, Fe also exhibit an obvious partitioning to β phase. Based on the 16 at.% V iso-surfaces in Fig. 7f, a proxigram was obtained in order to better reveal elemental partitioning behavior. The values of 16 at.% V was chosen because it approximately enable the major elemental concentrations in α and β phases lie midpoint in the proxigram. Fig. 8a reveals that Ti, Al and O preferentially partition to α phase while V, Fe and H more likely enter β phase. Moreover, C and N almost homogeneously disperse into α and β phases. The α/β interface could be determined to be 1.8 ± 0.2 nm in terms of the Ti concentration profile. Of particular note is that obvious concentration gradients of V and Fe exist at both sides of the interface, which enables the interface width to extend ~ 3.2 nm. Table 1 lists the accurate chemical compositions of α and β phases as well as the partitioning ratios of each element. The partitioning ratio k (for α -partitioning elements) or k' (for β -partitioning elements) were defined as $k = C_{\alpha}/C_{\beta}$ or $k' = C_{\beta}/C_{\alpha}$, respectively. The larger than unity for k or k' , the severer partitioning for the corresponding element. As seen in Fig. 8b, a pair of

parallel interfaces could be indicated by the 16 at.% V iso-surfaces. It can be known that these two planes should be the flat sides of β rod, i.e. the coherent $\alpha_{(0001)}/\beta_{(110)}$ interface. Moreover, the accurate determination of α and β compositions in this work is thought to greatly facilitate the simulation on $\alpha \leftrightarrow \beta$ phase transformation in additive manufacturing of Ti-6Al-4V by EBM. To precisely measure the thickness of β phase, a region of interest (ROI) that vertically goes across the two parallel iso-surfaces was created. The thickness of β phase was determined to be ~ 25 nm according to the depth concentration profiles in Fig. 8c.

3.2. Graded microstructure and mechanical properties

Concerning the potential graded microstructure for EBM-built Ti-6Al-4V, X-Z plane of the horizontal part was examined in detail. A region containing near-equiaxed prior β grains with a height of ~ 250 μ m (~ 5 layers) was clearly observed at the bottom (Fig. 9). An equiaxed-to-columnar transition for the prior β grains occurred due to the variation of solidification conditions (e.g. thermal gradient and solidification rate) in melt pool. The SEM observation of microstructure shows that β phase would become increasingly incomplete with build height in the initial tens of layers. It indicates different volume fractions of β phase retained, which depends on the temperature within the two-phase region as illustrated in vertical section of phase diagram of Ti-6Al-xV phase diagram [27]. The lower of the terminate temperature of rapid cooling process, the less amount of β phase will be retained. In practice, the bottom part, i.e. the observed equiaxed-to-columnar transition region that directly built on the start plate, will be removed as an extrusion once a build is completed. Nevertheless, this equiaxed-to-columnar transition phenomenon could give an important clue for precise control of EBM-built microstructure.

The following are important microstructural parameters for a quantitative characterization of EBM-built Ti-6Al-4V: prior β grain size, α/β colony size and β rod interspacing, which were sorted in a descending order in terms of their length scale. Here, α/β colony size is difficult to quantify, as its microstructure is composed of irregular mixture of colony and basket-weave structures due to

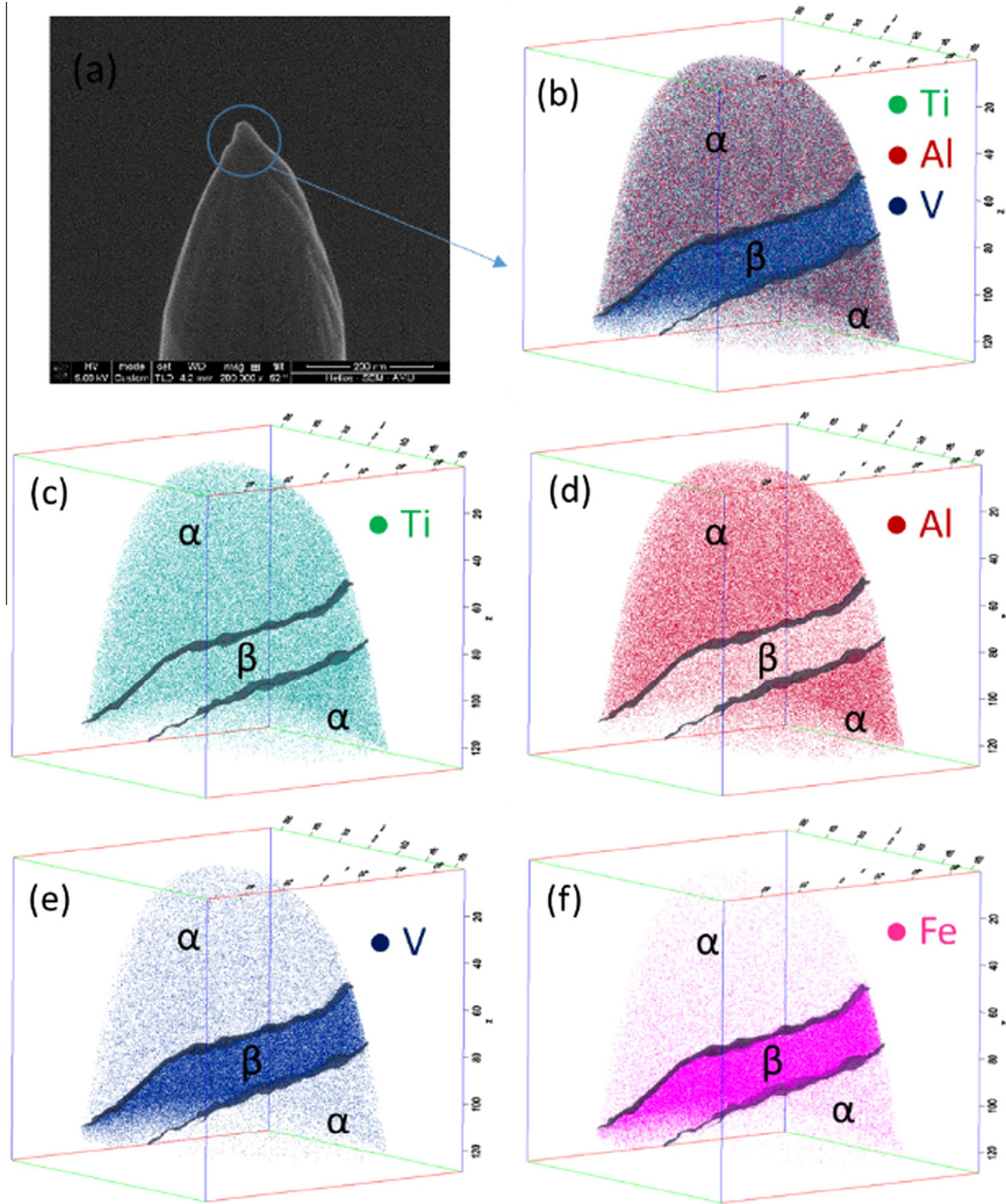


Fig. 7. (a) SEM image showing a micro-tip specimen prepared by FIB for APT analysis. (b) An APT reconstruction volume showing α and β phases. 16 at.% V iso-concentration surfaces (isosurfaces) was adopted to delineate the α/β interface. (c), (d), (e) and (f) show the elemental distribution of Ti, Al, V and Fe in the APT reconstruction, respectively.

the extremely high cooling rate. Fig. 10a, c, e and g show the α/β duplex microstructures of 10 mm-4, 10 mm-3, 10 mm-2 and 10 mm-1 samples at the X-Z plane, respectively. To be representative, all microstructures were taken from the midline area of each tensile testpiece. The size distribution histograms in Fig. 10b, d, f and h reveal that β rod interspacing continuously increases with the build height. The average β rod interspacings of 10 mm-1, 10 mm-2, 10 mm-3 and 10 mm-4 were determined to be $0.58 \pm 0.11 \mu\text{m}$, $0.66 \pm 0.16 \mu\text{m}$, $0.74 \pm 0.14 \mu\text{m}$ and $0.77 \pm 0.20 \mu\text{m}$, respectively. In addition, Fig. 11 presents that the prior β grain width gradually increases with build height, i.e. an average width of $42.77 \pm 14.52 \mu\text{m}$, $46.85 \pm 13.46 \mu\text{m}$, $54.77 \pm 20.15 \mu\text{m}$ and $56.82 \pm 13.73 \mu\text{m}$ in 10 mm-1, 10 mm-2, 10 mm-3 and 10 mm-4 samples, respectively. Both of β rod interspacing and β grain width were found to increase as build layers increased. As a result,

cooling rate was higher at the build bottom and it would constantly decreases with the rising build height. It is clear that graded microstructure occurs along the build direction for EBM-built Ti-6Al-4V. In general, the mechanical properties of engineering materials depend on their microstructure. Therefore, graded mechanical properties will be produced as a result of a graded microstructure. In order to verify the graded mechanical properties of EBM-built Ti-6Al-4V, microhardness and tensile tests were carried out on the 10 mm-1, 10 mm-2, 10 mm-3 and 10 mm-4 samples. The Vickers microhardness of these four samples are $327 \pm 5 \text{ HV}$, $324 \pm 5 \text{ HV}$, $322 \pm 7 \text{ HV}$ and $319 \pm 5 \text{ HV}$, respectively. It means that the microhardness continuously decreases with the increase of build height. Furthermore, the tensile properties degrade consecutively with the increasing build height as revealed in Table 2, i.e. all the yield strength, the ultimate tensile strength

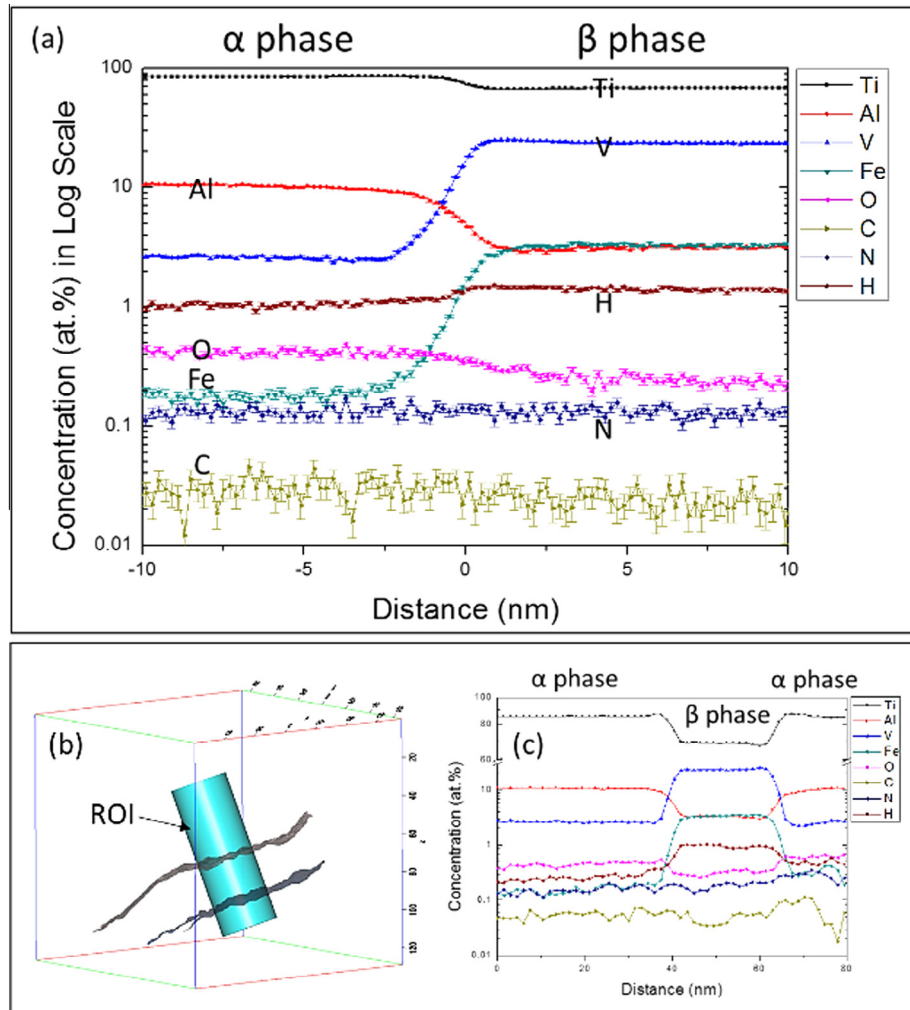


Fig. 8. (a) A proxigram showing the concentration profiles of alloying elements across the α/β interface delineating with a 16 at.% V iso-surface in the APT reconstruction in Fig. 8. (b) An region of interest (ROI) perpendicularly passes through two 16 at.% V iso-surfaces in the APT reconstruction volume. (c) 1D concentration profile along the Z axis of ROI in (b).

and the elongation decrease. It is thus confirmed that obviously graded microstructure as well as the resulting graded mechanical properties take place along the build direction for EBM-built Ti-6Al-4V.

4. Discussion

The thermal process of EBM is very complex as electron beam is the only heat source that was involved in a complicated relationship between maintaining a constant build temperature and melting. In any EBM setup there are two major heat losses: the heat radiation off the top surface and the heat conduction through the sintered powder from the surrounding surface of the part and start plate. Since only a low pressure of $\sim 2.0 \times 10^{-3}$ mbar was maintained during melting via introducing high pure He into the high vacuum build chamber, the heat loss due to convection could be neglected. Infrared (IR) imaging technique has been increasingly employed for in-situ surface temperature measurements and build flaws detection [28]. Unfortunately, it is still challenging to monitor the temperature distribution inside EBM-built parts. Temperature was only measured by a thermocouple mounted at the bottom of start plate and it is not used in any feedback due to practical reasons. For instance, the measured temperature was plotted versus time in Fig. 12a for the entire EBM build process of horizontal

Ti-6Al-4V blocks. It can be divided into three stages regarding the temperature during melting process: (1) a sharp decrease, (2) a slow increase and (3) an appropriate constant. The heat transfer (q) by thermal conduction and radiation is given by [29]

$$q = -kA \frac{\partial T_1}{\partial x} t + \sigma e A \partial T_2^4 \quad (2)$$

where k is the thermal conductivity of materials ($k = 14.1 \text{ W m}^{-1} \text{ K}^{-1}$ for Ti-6Al-4V at 650°C [4]), A is the cross section area ($A = 1.0 \times 10^{-3} \text{ m}^2$), ∂T_1 is the temperature difference between top surface and bottom part, ∂x is the build height, t is the build time, σ is the Stefan-Boltzmann constant, e is the emissivity (unity for a black body), and ∂T_2 is the temperature difference between top surface and ambient. Therefore, the heat transfer rate $\partial q / \partial t$, which directly reflects the cooling rate, could be derived as

$$\frac{\partial q}{\partial t} = -kA \frac{\partial T_1}{\partial x} \quad (3)$$

Here, we assume that the temperature of melt pool (top surface) is constant as the heat provided by electron beam to melt powder bed is supposed to be fixed for each built layer with the same cross geometry. Moreover, the melting as well as the subsequent heat radiation from the melt pool to the ambient were completed immediately due to the fast scan velocity of electron beam and high

Table 1
Chemical compositions of α and β phases for EBM-built Ti–6Al–4V ELI obtained from APT analysis (in at.% and wt.%).

	Ti	$\sigma^*(\text{Ti})$	Al	$\sigma(\text{Al})$	V	$\sigma(\text{V})$	Fe	$\sigma(\text{Fe})$	O	$\sigma(\text{O})$	C	$\sigma(\text{C})$	N	$\sigma(\text{N})$	H	$\sigma(\text{H})$	
α phase	In at.%	85.1519	0.1344	10.4907	0.1158	2.6502	0.0607	0.1644	0.0153	0.4089	0.0241	0.0273	0.0062	0.1205	0.0131	0.9861	0.0373
	In wt.%	90.3208	0.1860	6.2724	0.0392	2.9917	0.1808	0.2034	0.0832	0.1450	0.0065	0.0073	0.0016	0.0374	0.0043	0.0220	0.009
β phase	In at.%	68.2165	0.1754	3.1267	0.0655	23.6827	0.1602	3.2839	0.0672	0.2404	0.0184	0.0251	0.0059	0.1323	0.0137	1.2925	0.0425
	In wt.%	68.7896	0.1769	1.7773	0.0372	25.4158	0.1719	3.8534	0.0791	0.0810	0.0062	0.0064	0.0015	0.0390	0.0040	0.0274	0.009
k or k'																	
		1.25	3.36	8.94		19.98		1.70		1.08		1.09		1.09		1.31	

* Error.

** $k = C_{\alpha}/C_{\beta}$ or $k' = C_{\beta}/C_{\alpha}$.

vacuum. Provided that the heat loss through radiation from the melt pool to the ambient is invariable for each layer, the heat loss due to radiation could be assumed to be independent of time and build height. For the stage (1) in Fig. 12a, corresponding to the very bottom part (~ 1 –2 mm in height), both ∂T_1 and ∂x increase, hence the variation of cooling rate was not known. For the stage (2), ∂T_1 decreases and ∂x increases, as a result that the cooling rate decreases. For the stage (3) ∂T_1 remains constant while ∂x continuously increases, consequently the cooling rate will continue falling down. On the other hand, a slow cooling rate will definitely result in a coarse microstructure. Thus, it is capable of explaining the microstructural variation as mentioned above, i.e. the prior β grain width and the β rod interspacings gradually increase with the build height.

Based on our current understanding, the microstructural evolution of EBM-built Ti–6Al–4V mostly could be simplified as the following main processes as illustrated in Fig. 12b and c: (i) the rapid solidification for $Melt \rightarrow$ Prior β grains; (ii) the rapid cooling for $\beta_{\text{Prior}} \rightarrow \alpha'_{\text{Martensite}}$ from a temperature above β transus to a build temperature of ~ 600 –650 °C; (iii) the near-isothermal annealing for $\alpha'_{\text{Martensite}} \rightarrow \alpha_{\text{Colony\&Basket-weave}} + \beta_{\text{Rod}}$ at the build temperature; (iv) the slow cooling for $\alpha'_{\text{Martensite}} \rightarrow \alpha_{\text{Colony\&Basket-weave}} + \beta_{\text{Rod}}$ for the top-built layers. Here, the cooling rates during solidification and cooling in solid were calculated to be in the range $\sim 10^3$ – 10^5 °C s $^{-1}$ [13]. It must be pointed out that it is still debatable regarding the existence of α' martensite in EBM-built Ti–6Al–4V. It has been known that a full martensite microstructure forms when untransformed β is rapidly cooled down below the martensite start temperature (Ms) with a sufficiently high cooling rate. However, a variety of Ms and critical cooling rates for martensite formation in Ti–6Al–4V were reported, e.g. a high Ms of 850 °C and a low critical cooling rate of >18 °C s $^{-1}$ from [30], a low Ms of 575 °C and a high critical cooling rate of >410 °C s $^{-1}$ from [31], etc. Compared with the other published data, the Ms of 800 °C provided in the Handbook of Titanium Alloys [4] and the critical cooling rate of >410 °C s $^{-1}$ [31] should be more acceptable, as they have been widely cited for martensitic transformation in Ti–6Al–4V. Although the accurate cooling rate of EBM process is unknown, it is confirmed to exceed 410 °C s $^{-1}$. Similarly, the surface temperature of the build should be below 800 °C in terms of the temperature curve in Fig. 12a. Therefore, martensite is supposed to form during EBM-built Ti–6Al–4V process. Furthermore, another possible martensite α'' (orthorhombic) only occurs when Ti–6Al–4V is quenched from temperatures between 750 and 900 °C [4]. While a continuously rapid cooling from liquid to the build surface temperature is involved in EBM process. It is thus concluded that α' martensite (hcp) formed during the process (ii) stated above. Like other martensitic transformation, α' martensite will also undergo a reversible reaction on cooling and heating, i.e. $\beta \leftrightarrow \alpha'$. In addition, α' martensite will decompose into α and β phases, i.e. $\alpha' \rightarrow \alpha + \beta$, when it is subjected to an isothermal annealing in the $\alpha + \beta$ two phase field at intermediate temperatures. The decomposition of α' martensite in Ti–6Al–4V has been investigated by Gil Mur et al. [32] using isothermal annealing treatments. According to the kinetic curve of martensitic transformation in [32], it was found that α' could be fully decomposed at a temperature above 650 °C. More specifically, full decomposition of α' can be achieved within 1 h at 700 °C. As revealed in Fig. 12a, the temperature beneath the start plate was kept at ~ 650 °C during the most time of melting. Electron beam is the only heat source that scans over powder bed unremittingly. The heat conduction from top to the start plate along the built part is one of the main heat loss paths. It is thus able to assume that the temperature of the built upper part should be in excess of 650 °C. It demonstrates that full decomposition of α' into α and β phases occurred as stated in process (iii) in bulk microstructure, which is in good agreement with our XRD results. It was proposed that α' martensite is transformed into α as a fine precipitate that is

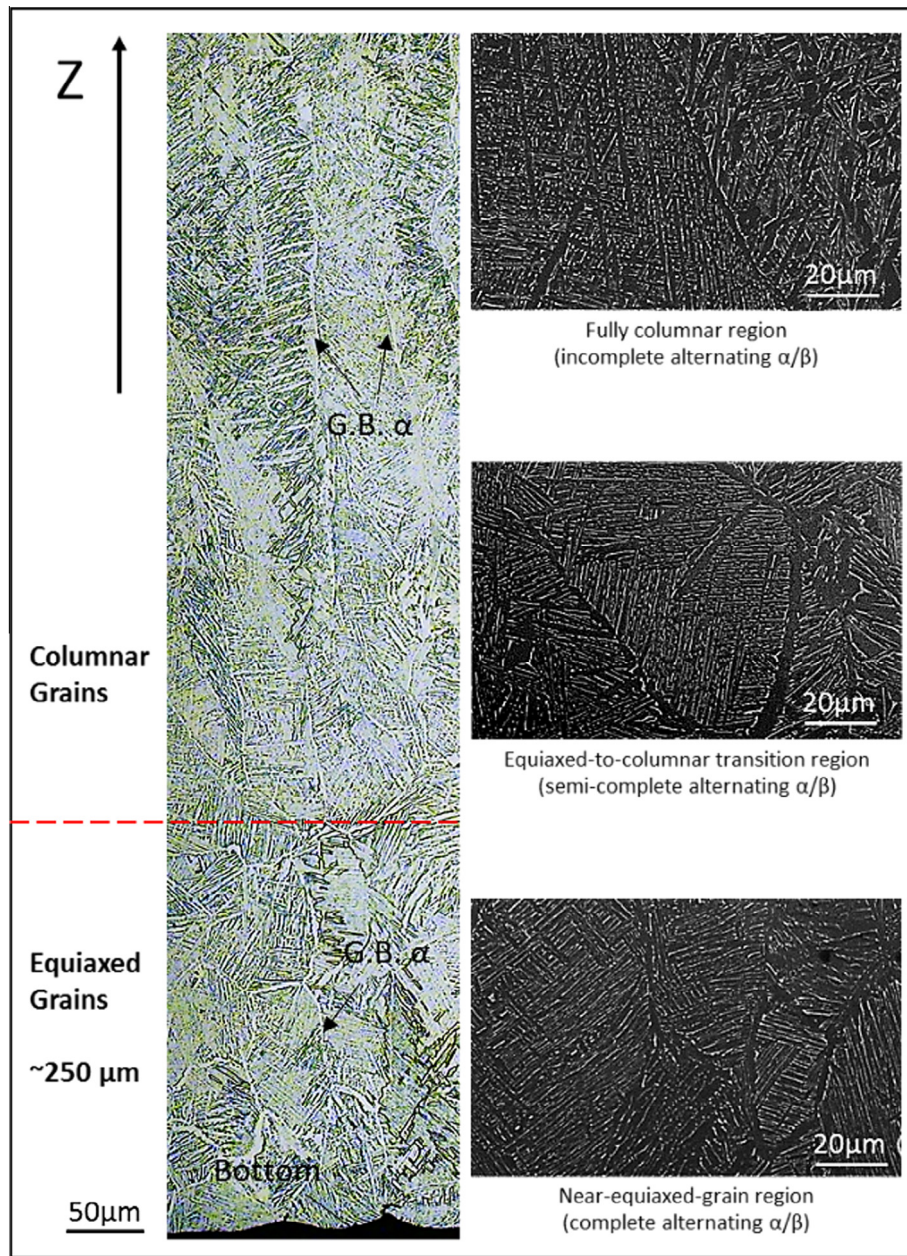


Fig. 9. OM micrograph showing the equiaxed-to-columnar transition of prior β grains at the initial tens of layers. SEM micrographs showing the alternating α/β evolution with the build height.

nucleated heterogeneously at martensite plate boundaries or at internal structures such as twins [32]. Numerous micro-twins have been observed inside α phase as shown in Fig. 5, which provides a direct evidence for the decomposition of α' into α . It also indicates the formation of α' martensite in process (ii). A slow cooling process started once the build was completed. An effective temperature range for α' decomposition will still be valid for ~ 1 h when the last built layers (top part) undergo the process (iv). The top surface of EBM-built Ti-6Al-4V has been examined by XRD and no α' was detected. This suggests that α' martensite has been fully transformed into $\alpha + \beta$ microstructure in EBM as-built Ti-6Al-4V. As we know, α' martensite is very hard, which allows a high strength but a low ductility of materials. It was previously accepted that martensite is supposed to be avoided in EBM-built Ti-6Al-4V via an elevated build temperature. However, it has been pointed out

that the Ti-6Al-4V microstructure containing a mixture of α and α' will have superior mechanical properties [33]. Thus, it is promising to further improve the microstructure and mechanical performance of EBM-built Ti-6Al-4V via introducing some amount of martensite by means of adjusting processing parameters.

It is still unclear on the interpretation of α/β interface layer (or interface phase) that was commonly observed in Ti-6Al-4V or other $\alpha-\beta$ titanium alloys [10,34]. In the present work, an L phase interface layer with a distinguished fcc crystal structure has been observed between α and β phase under dark field TEM mode as shown in Fig. 5. However, it was not identified in the APT reconstruction volumes as we only see a uniform composition component surrounding β phase. Our current experimental results suggest that the interface phase L exists and it has an identical composition but a different crystal structure with α phase. In the

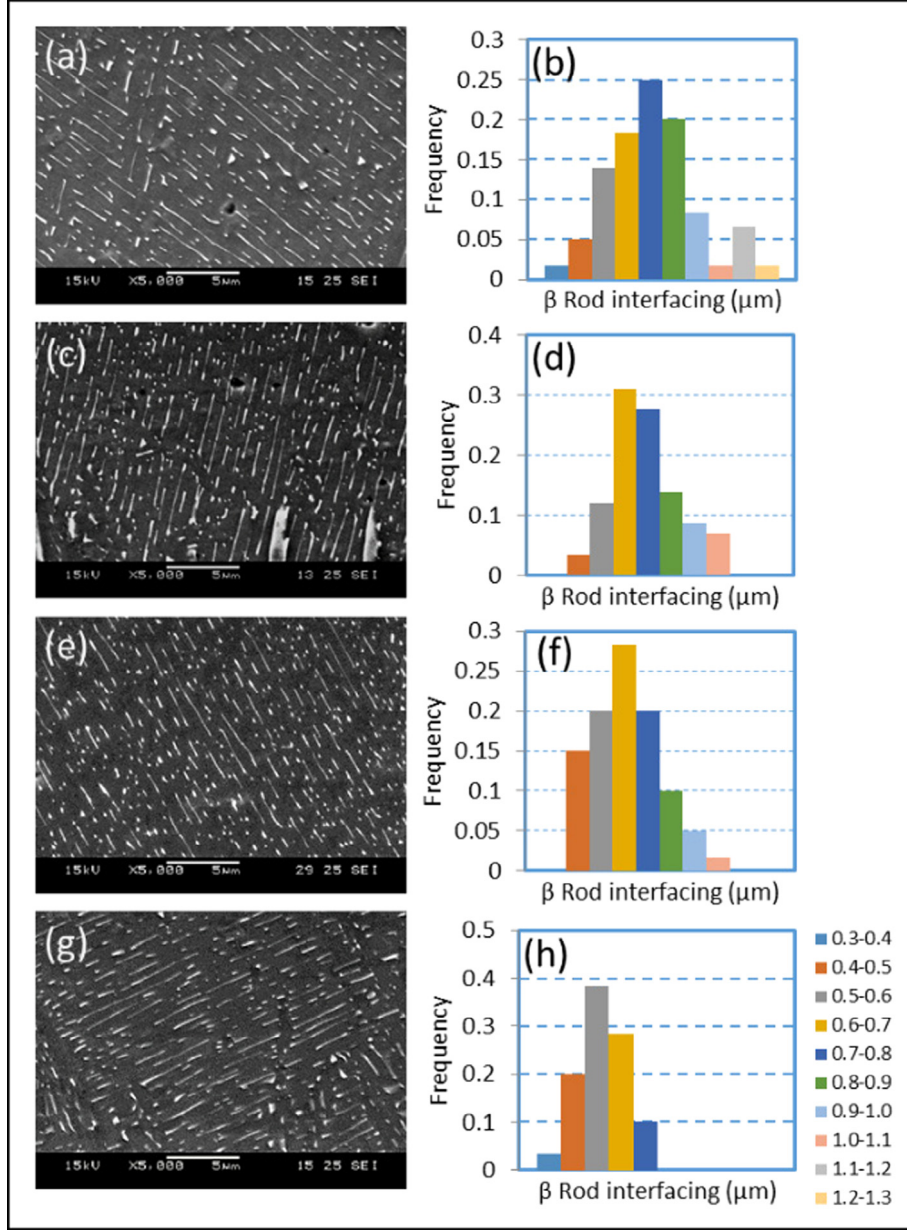


Fig. 10. SEM images showing the α/β duplex microstructure as well as the corresponding β rod interspacing distribution histograms of (a) and (b) for 10 mm-4, (c) and (d) for 10 mm-3, (e) and (f) for 10 mm-2, (g) and (h) for 10 mm-1 samples.

meanwhile, the APT results convince us of not being the artificial hydride for the α/β interface phase. As the phase transformation of $\alpha' \rightarrow \alpha + \beta$ proceeds, i.e. the advance of interface into α , vanadium will be continuously ejected from α into β due to its low solubility in α . Further, vanadium has a low diffusivity in β [5] so that vanadium concentration will form a “bump” in β adjacent to the interface (as illustrated in Fig. 13a). Specifically, we have observed a slight interfacial excess of vanadium at the interface front of β phase in Fig. 13b. It is thus known that the migration of interface would mainly rely on the transfer of vanadium atoms [35]. The Gibbsian interfacial excess of an element i , Γ_i , is defined by the excess number of solute atoms i (N_i^{excess}) per unit area (A). Γ_i can be determined utilizing proxigram concentration profiles for an arbitrary interface by [36]:

$$\Gamma_i = N_i/A = \rho \Delta x \sum_{j=1}^p (c_i^j - c_i^m) \quad (4)$$

where ρ is the atomic density (60.98 atoms nm^{-3} for β phase in this work), Δx is the distance between the p -layers in the proxigram, c_i^j is the concentration of the j th atom, and c_i^m is the average concentration of element i in the matrix. In terms of the proxigram in Fig. 13b, vanadium segregated with a Γ_i value of 2.23 ± 0.12 atoms nm^{-2} at the interface front of β phase. As no composition variation was observed, the formation of α/β interface layer has to be taken into account from the viewpoint of crystallography. There will be a $\sim 15\%$ lattice expansion involved from β to α transformation in terms of their crystallography parameters obtained by XRD in this work. This lattice strain due to the $\beta \rightarrow \alpha$ volumetric expansion must be accommodated at the α/β interface. On the other hand, a large amount of micro-twins have been observed inside the α phase, which should accommodate the deformation involved during the transformation of $\alpha' \rightarrow \alpha$, even though very small lattice difference exists between α and α' . Thus, it is suggested that the formation of the L interface layer is mainly attributed to the lattice

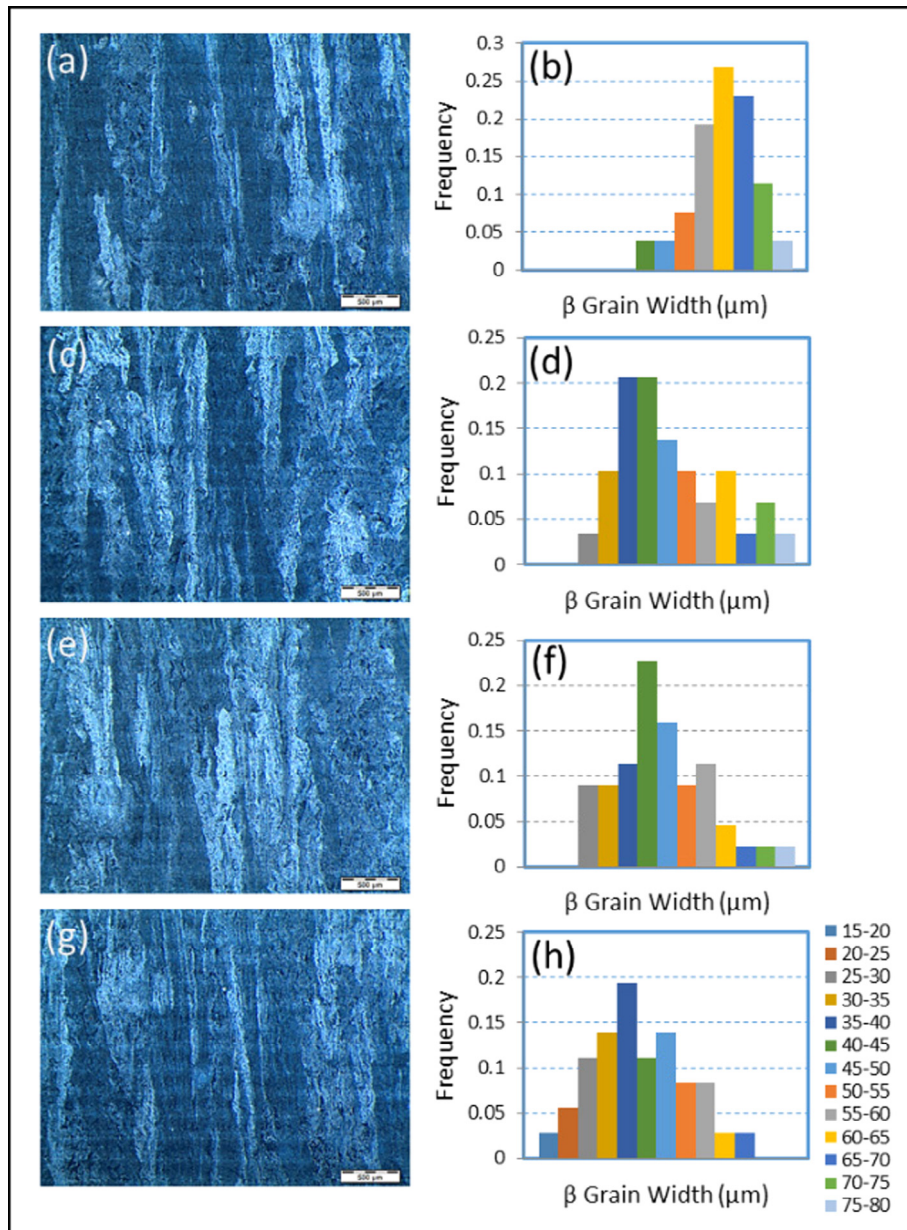


Fig. 11. OM images showing the columnar prior β grains as well as their corresponding width distribution histograms of (a) and (b) for 10 mm-4, (c) and (d) for 10 mm-3, (e) and (f) for 10 mm-2, (g) and (h) for 10 mm-1 samples.

Table 2
Yield strength, ultimate tensile strength and elongation of four EBM-built Ti-6Al-4V samples with different build heights.

Specimen	Yield strength (0.2% offset) (MPa)	Ultimate tensile stress (MPa)	Elongation (%)
10 mm-1	851.8 ± 5.8	964.5 ± 0.3	16.3 ± 0.8
10 mm-2	836.6 ± 8.7	953.7 ± 4.3	15.2 ± 1.2
10 mm-3	827.9 ± 0.3	944.5 ± 5.8	14.0 ± 0.5
10 mm-4	823.4 ± 0.1	940.5 ± 6.5	13.2 ± 0.7

mismatch between α and β phases via a shear mechanism. The interfacial segregation of vanadium at the interface front of β phase is believed to further promote the formation of this interface layer. In addition, it was reported that the L phase should act as a transition phase from β to α and it will not occur once the α and β phases are in thermodynamic equilibrium [10]. This is consistent with the nonequilibrium EBM process. More detailed work will be needed to

interpret the transformation of $\beta \rightarrow L \rightarrow \alpha$ on the crystallographic point of view.

If we neglect the interface phase for simplicity, the volume fraction of β phase can be derived from the following equations:

$$C_0 = C_\alpha V_f(\alpha) + C_\beta V_f(\beta) \quad (5)$$

$$V_f(\beta) = (C_0 - C_\alpha) / (C_\beta - C_\alpha) \quad (6)$$

where C_0 is the overall composition of Ti-6Al-4V ELI; C_α and C_β are the compositions of α and β phases; $V_f(\alpha)$ and $V_f(\beta)$ are the volume fractions of α and β phases, respectively. The $(C_0 - C_\alpha) - (C_\beta - C_\alpha)$ graph was plotted and the slope of the fit line is approximately equal to the volume fraction of β phase. Hence, $V_f(\beta)$ can be determined to be $3.56 \pm 0.51\%$. This value is supposed to be more convincing compared to those obtained by other methods because of using the accurate compositions in Table 1. Moreover, the volume fraction of $\sim 3\%$ has almost reached up the detection limit of

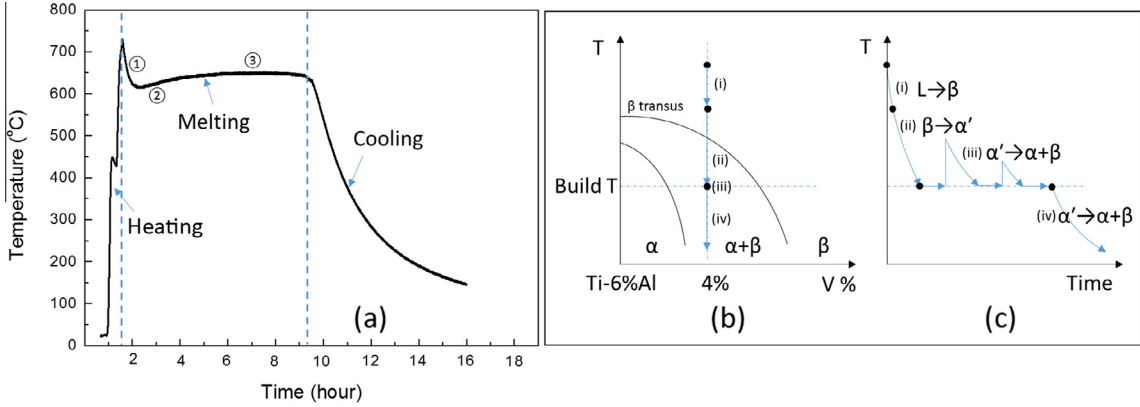


Fig. 12. (a) Temperature (measured by a thermocouple beneath start plate) vs time curve during the entire EBM build process. (b) Schematic phase diagram of Ti6Al–V and (c) simplified thermal process showing the four main phase transformation processes involved in EBM-built Ti-Al–4V.

conventional XRD techniques. This is the reason for which only a weak peak of β phase could be detected in XRD profile in this work. β phase is considerably softer than α phase; it behaves like a dispersion of soft particles in a hard matrix [37]. The deformation mechanisms of EBM-built Ti-6Al-4V with this kind of distinct microstructure are still rarely investigated. Nevertheless, its mechanical properties are believed to highly rely on the morphology, the size, the volume fraction and the distribution of β phase. In the present work, an effort has been made to obtain a quantitative characterization of α and β phases. This would no doubt be helpful to understand its deformation and fracture mechanisms in our future work.

The relationship between yield strength and microstructural scale has been commonly modeled using the classical Hall-Petch relation for a wide variety of engineering materials [38]. A more general description of the Hall-Petch dependence for yield strength could be given by [38]

$$\sigma_y = m_t(\tau_0 + k_s l^{-1/2}) \quad (7)$$

where m_t is the Taylor factor, τ_0 is the average resolved shear stress, k_s is the Hall-Petch constant, and l is the microstructural scale. Although Ti-6Al-4V usually has a multiscale microstructure, Hall-Petch dependent yield strengths were found with grain size, colony size or α lath thickness in some Ti-6Al-4V fabricated by conventional methods [39,40]. Hexagonally close-packed metals were proposed to exhibit a reasonably strong Hall-Petch dependence. That is due to the fact that they have a large value of m_t and there

is a need for slip occurring at grain boundaries on prism or pyramidal slip systems in order to adjust accommodation of strains [38]. As stated previously, ~96% volume fraction of hcp α phase formed in the microstructure of Ti-6Al-4V as-fabricated by EBM, therefore its yield strength is supposed to present an obvious Hall-Petch effect. The possibility that the graded yield strength of EBM-built Ti-6Al-4V is primarily attributed to the Hall-Petch effect was examined by plotting σ_y against $(\beta$ interspacing, $\lambda)^{-0.5}$ and (prior β grain size, $d)^{-0.5}$ in Fig. 14a. A good agreement with the Hall-Petch relation indicates that the graded property takes place mainly due to the graded microstructure. This is also consistent with the previous works showing that the yield strength of Ti-6Al-4V increases with the decreasing microstructural scale [39,40]. As m_t is taken equal to 3 for the specific α - β structure [41], values of the Hall-Petch constant k_s could be determined as 0.070 MPa \sqrt{m} and 0.553 MPa \sqrt{m} for λ and d , respectively in terms of the slopes in Fig. 14a. When the prior β grain size is taken into account as the effective microstructural scale, the slope of yield strength is steeper than that when the β interspacing is taken. It demonstrates that the prior β grain size is more influential compared to the β interspacing on yield strength. It might be probably owing to the higher capability of absorbing dislocations for grain boundary in comparison to the α/β interface.

In terms of the most commonly cited dislocation pile-up model [42], k_s could be derived as follows:

$$k_s = \sqrt{4\tau_c G b / q\pi} \quad (8)$$

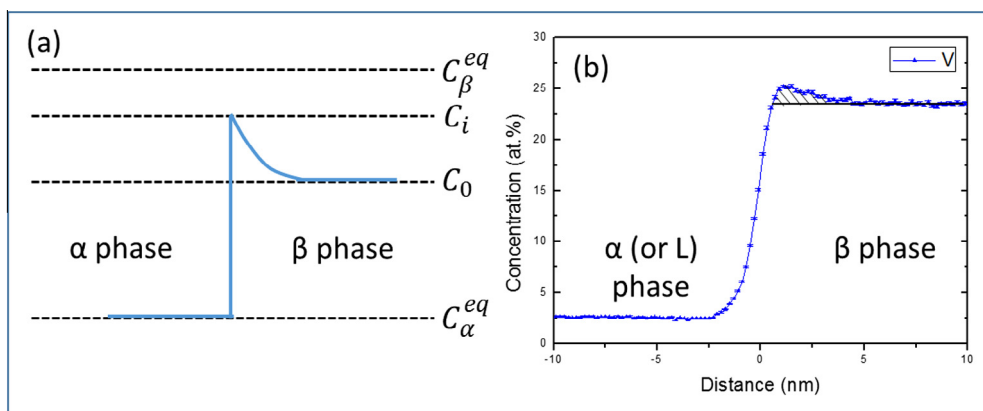


Fig. 13. (a) Theoretical vanadium concentration profile at the α/β interface. (b) Actual vanadium concentration profile across the α (or L)/ β interface delineating with a 16 at.% V iso-surface in the APT reconstruction in Fig. 8. The shaded area denotes the vanadium interfacial segregation zone at the interface front of β phase.

where τ_c is the barrier strength, G is the shear modulus, b is the Burger's vector, q is a constant (1.0 for screw dislocations and 0.67 for edge dislocations). Eq. (8) may be used to estimate k_s for EBM-built Ti-6Al-4V by assuming a barrier strength of 0.01G and taking $b = 3.0e-10$ m for $\langle a \rangle$ slip [43]. Suppose that G is constant in the same material, inserting a value of $G = 38$ GPa for additive manufactured Ti-6Al-4V [44] into Eq. (8) yields k_s values of 0.074 MPa \sqrt{m} (screw dislocations) or 0.091 MPa \sqrt{m} (edge dislocations). It is worth noting that both of the k_s values computed from the pure screw dislocation and pure edge dislocation are higher than that obtained from the α/β interfaces (0.070 MPa \sqrt{m}) and lower than that obtained from the prior β grain boundaries (0.553 MPa \sqrt{m}). Both the α/β interface and the prior β grain boundaries are the main factors influencing the strength of EBM-built Ti-6Al-4V. Therefore, neither the β interspacing nor the prior β grain size could fully account for its strength. In the case of a mixed dislocation mode, k_s is supposed to be within the value range of 0.074 MPa \sqrt{m} (screw dislocation) and 0.091 MPa \sqrt{m} (edge dislocation). Obviously, the k_s (mixed dislocation) is much closer to the measured value of 0.070 MPa \sqrt{m} from the β interspacing as compared to 0.553 MPa \sqrt{m} from the prior β grain size. Thus, it suggests that the α/β interface strengthening would play the primary role in determining the strength of EBM-built Ti-6Al-4V having a multi-scale microstructure with cellular colony and basket-weave morphology. Meanwhile, β grain refinement strengthening seems to be more effective as the prior β grain boundaries could absorb a higher amount of dislocations in comparison with α/β interfaces.

Hardness tests were frequently performed to assess the impact of processing on mechanical properties as its quick and easy implementation with a non-destructive feature. It is constructive to compare hardness values with both yield strength and ultimate tensile strength, which allows us to more conveniently estimate the mechanical properties of local parts. The stress-hardness relations have been extensively investigated. In general, the relationships among yield strength (σ_y), ultimate tensile strength (σ_u) and Vickers hardness (H_V) were proposed as follows [45,46]:

$$\sigma_y = \frac{H_V}{3} (0.1)^n \quad (9)$$

$$\sigma_u = \left(\frac{H_V}{2.9} \right) \left(\frac{n}{0.217} \right)^n \quad (10)$$

where n is the work hardening coefficient that can be measured from the slope of a log-log plot of true stress versus true strain, as given by $\sigma = K\epsilon^n$, where K is the material strength coefficient. The strain hardening exponent is a measure of the increase in strength of materials because of plastic deformation. The value of n lies between 0 and 1. When $n = 0$ the material is a perfectly plastic solid, while a value of 1 represents a 100% elastic solid. The larger of the n value, the more pronounced of the strain hardening effect. Fig. 14b is a log (true stress) versus log (true strain) for a plastic portion that lies between yield point and 1.0% strain of the four samples. Values of $n = 0.132, 0.135, 0.136$ and 0.141 were obtained for 10 mm-1, 10 mm-2, 10 mm-3 and 10 mm-4 samples, respectively. The variation of n value is believed to result from the different microstructures caused by the varying cooling rates and annealing time. It has been found that the upper part has a larger n value in comparison with the lower part. It means a more pronounced strain hardening effect occurred in the upper part, which results in short elongations in turn. Obviously, this is because the lower part was subjected to a longer annealing treatment. As known, annealing is able to effectively reduce the numbers of dislocation, alternately it will eliminate the strain hardening effect [47]. Consequently, an increasingly pronounced strain hardening phenomenon was observed with the rising build height.

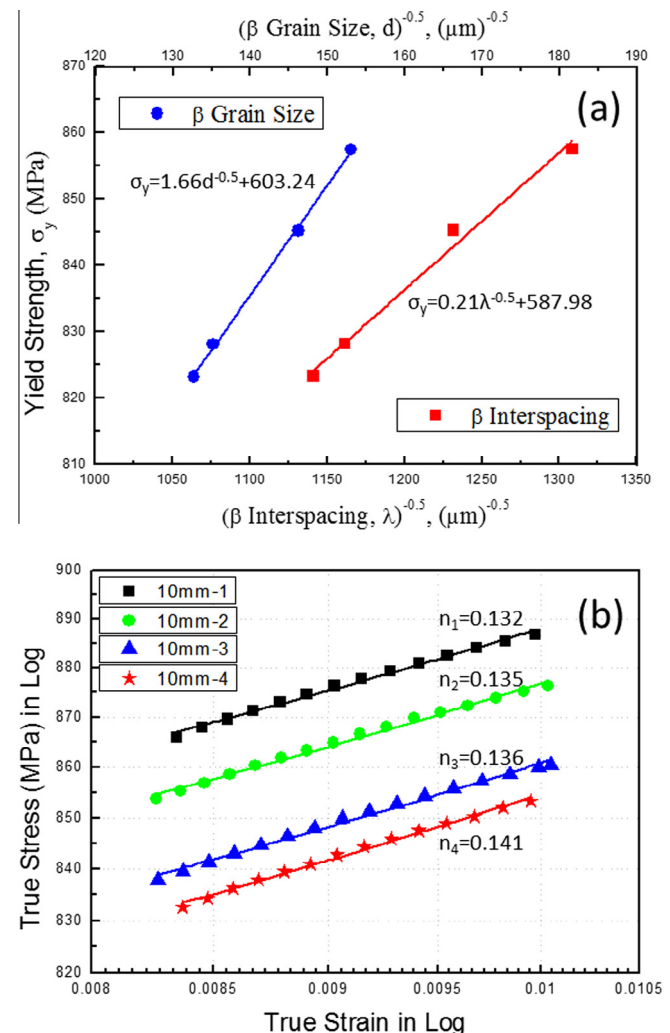


Fig. 14. (a) Variation of average yield strength σ_y with inverse of square root of average prior β grain size (d) and average β rod interspacing (λ). (b) True stress-true stain curves for the plastic response of the four EBM-built samples, plotted on logarithmic axes. The measured power-law strain hardening exponents and strength coefficients are indicated for each sample.

In addition to the empirical equations by taking the strain hardening exponent into account, some linear correlations between yield strength and microhardness, and between ultimate tensile strength and microhardness were obtained via the regression analysis method for steels [48,49]. In particular, two linear correlations between tensile strength (σ_y and σ_u) and microhardness H_V were reported for Ti-6Al-4V and its electron beam welded joints, which are given by [50]

$$\sigma_y = 3.013H_V - 127.012 \quad (11)$$

$$\sigma_u = 3.586H_V - 237.900 \quad (12)$$

The predicted yield strength and ultimate tensile strength according to Eqs. (9–12) for the four experimental samples are compiled in Table 3. It is found that the predicted yield strength and ultimate tensile strength obtained from the regression analysis method are much closer to the measured values compared to Cahoon et al. expressions. Nevertheless, the predicted ultimate tensile strength was slightly underestimated for the regression method. This might be because of its high ductility due to the ultra-fine microstructure generated in EBM-built part. On the other hand, the predicted yield strength was underestimated while the

Table 3

Comparison of yield strength and ultimate tensile strength values obtained from stress-strain curves, Cahoon et al. expressions and regression analysis.

Specimen	HV	HV (MPa)	Strain hardening exponent n	Stress-strain curve		Cahoon et al. expression		Regression analysis	
				YS (MPa)	UTS (MPa)	YS (MPa)	UTS (MPa)	YS (MPa)	UTS (MPa)
10 mm-1	327 ± 5	3206	0.132	857.6	964.2	788.6	1035.3	858.2	934.7
10 mm-2	324 ± 5	3177	0.135	845.3	949.4	776.1	1027.5	849.2	924.0
10 mm-3	322 ± 7	3157	0.136	828.2	938.7	769.4	1021.6	843.2	916.8
10 mm-4	319 ± 5	3128	0.141	823.3	934.0	753.6	1015.0	834.1	906.0

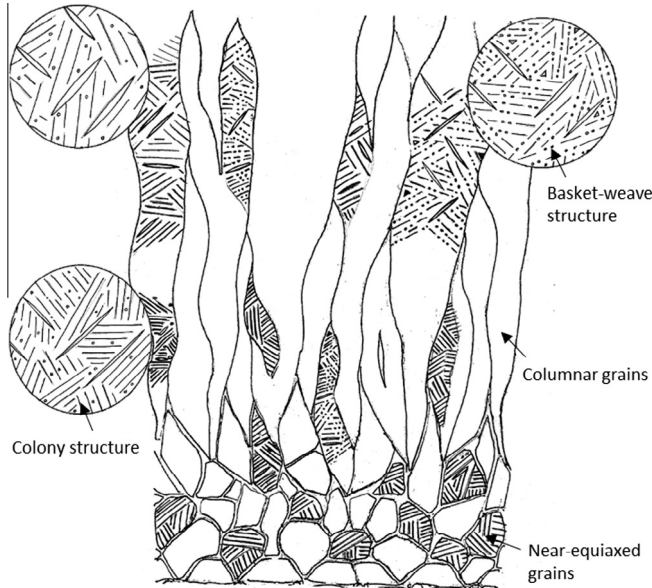


Fig. 15. Schematic microstructure of EBM-built Ti-6Al-4V on X-Z plane.

predicted ultimate tensile strength was overestimated with regard to Cahoon et al. expressions. One possible reason is that the divisors in Eqs. (9) and (10) are not very appropriate. Furthermore, the n value is found to be highly dependent on strain and strain rate [51]. As suggested, there might be no such an alternative general hardness-strength conversion expression that is available for all materials [52]. Instead, specific equations or relationships should be derived for EBM-built Ti-6Al-4V.

For graded materials, one may refer to the functionally graded materials (FGM) that are a relatively new class of engineered materials in which the composition and/or microstructure vary in one specific direction. They are usually intentionally produced by a continuous change in composition. Such a graded microstructure is supposed to better resist thermal and mechanical cycling since it does not have a specific interface [53]. EBM is the layered manufacturing technique that works under an elevated temperature. In addition, there are several phase transformations (e.g. $\beta \leftrightarrow \alpha$ or $\beta \leftrightarrow \alpha'$) involved in Ti-6Al-4V. Ti-6Al-4V is subjected to a near-isothermal heat treatment at the build temperature during EBM. The previously built layers definitely undergo a longer annealing compared to the subsequent layers, which has been seen to influence the strain hardening effect inside the build with different height. More importantly, cooling rate will constantly change with the increasing build height, which would significantly impact on the length scale of microstructure. It is thus easily understood why graded microstructure formed for EBM-built Ti-6Al-4V. In comparison to the FGM, EBM-built Ti-6Al-4V could be termed inherently graded materials (IGM). On the basis of the experimental results stated above, an overall picture of EBM-built Ti-6Al-4V could be given in Fig. 15. The graded prior columnar β grain width and β rod interspacing inside each grain are the two main

microstructural features. As expected, one of the advantages of this type of graded microstructure is to improve materials' ductility along the gradient direction without large loss of strength. We have found that the average elongation of EBM-built Ti-6Al-4V ELI along the vertical direction could reach up to ~20%. It means an increase of >30% for elongation as compared to the horizontal build direction. Of particular interest is that gradient nanograined structure that formed as an outermost surface layer was recently found to be able to effectively improve materials' ductility [54]. It has been suggested by Lu [54] that gradient microstructures could enhance elongation by the suppression of strain localization. This is due to various plastic deformation occurring concurrently at largely different microstructures thus releasing the intergranular stress between neighboring grains with different sizes. In addition to improving ductility, the graded microstructure is also believed to enhance fatigue resistance. Taking into account that the unceasing change of cooling rate is one of the main causes for the formation of graded microstructure in EBM-built Ti-6Al-4V, consistent microstructure might be achieved either by constantly enhancing melt temperature or adjusting cross section melt geometries. On the contrary, the IGM produced by EBM process may be purposely used by taking advantage of its improved ductility and fatigue resistance. The investigation on these two aspects has been placed into our research focus in the future.

5. Conclusions

The microstructure and mechanical properties of as-built Ti-6Al-4V ELI by EBM were systematically investigated. Based on these experiments, the following conclusions can be drawn:

- (1) The microstructure of as-built Ti-6Al-4V consists of columnar prior β grains delineated by wavy grain boundary α and transformed $\alpha + \beta$ structures with both cellular colony and basket-weave morphology as well as numerous singular α bulges within the prior β grains. β phase was found to form as discrete flat rods embedded in continuous α phase and its volume fraction was determined to be $3.56 \pm 0.51\%$. No α' martensite was observed as it completely decomposed into α and β phases. The hcp α phase and bcc β phase were identified by XRD and TEM. The lattice constants were measured to be $a = 0.293$ nm and $c = 0.467$ nm for α phase and $a = 0.320$ nm for β phase, respectively.
- (2) APT experimental results reveal that Ti, Al and O preferentially partition to α phase while V, Fe and H more likely enter β phase. C and N almost homogeneously disperse into α and β phases. Fe, V and Al are the three elements showing the most obvious partitioning behavior. Accurate compositions of α and β phases as well as the partitioning ratio of each element were obtained.
- (3) An interface L phase with a distinct fcc crystal structure of $a = 0.441$ nm between α and β phases was identified. The L phase was found to have the same compositions compared to the α phase. According to the proxigram with a 16 at.% V isosurface, the L/ β interface was determined to be 1.8 ± 0.2 nm while no α /L interface was detected.

Vanadium segregated with a Γ_i value of 2.23 ± 0.12 atoms nm $^{-2}$ at the interface front of β phase. It is suggested that the formation of the L interface layer is mainly attributed to the lattice mismatch between α and β phases via a shear mechanism. The interfacial segregation of vanadium at the interface front of β phase is believed to further promote the formation of this interface layer.

- (4) Graded Ti-6Al-4V microstructure including varying prior β grains and β phase interspacings was seen, i.e. near-equiaxed prior β grains as well as the equiaxed-to-columnar transition region at the initial several build layers and the subsequent columnar prior β grains with increasing grain width and β rod interspacing. The coarser and coarser columnar microstructure mainly arises from the decreasing cooling rate. In addition, an increasingly pronounced strain hardening effect was observed with the rising build height as the previously built layers were subject to a longer annealing compared to the subsequent layers.
- (5) Graded mechanical properties of Ti-6Al-4V with degraded microhardness and tensile properties were observed from bottom to top, i.e. increasing microhardness, yield strength and ultimate tensile strength while decreasing elongation as the build height rises. A good agreement with the Hall-Petch relation indicates that the graded property takes place mainly due to the graded microstructure. In addition, the α/β interface strengthening was found to play the primary role in determining the strength of EBM-built Ti-6Al-4V that possesses a multiscale microstructure with cellular colony and basket-weave morphology. Nevertheless, β grain refinement strengthening seems to be more effective as the prior β grain boundaries could absorb a higher amount of dislocations in comparison with α/β interfaces.

Acknowledgements

The authors are grateful for financial support provided by A*Star industrial additive manufacturing program: work package 3 and the fruitful discussion with Dr. Nai Mui Ling Sharon, Dr. Guglielmo Vastola, Dr. Pei Qing Xiang and Dr. He Zeming. The authors acknowledge the use of resources in NTU Additive Manufacturing Centre supported by Singapore Economic Development Board (EDB). The authors acknowledge financial support from the French CNRS (FR3507) and CEA METSA network (www.metsa.fr).

References

- [1] W.E. Frazier, Metal additive manufacturing: a review, *J. Mater. Eng. Perform.* 23 (2014) 1917–1928.
- [2] C.K. Chua, K.F. Leong, *3D Printing and Additive Manufacturing: Principles and Applications*, 4th ed., World Scientific, Singapore, 2014.
- [3] X. Gong, T. Anderson, K. Chou, Review on powder-based electron beam additive manufacturing technology, *Manuf. Rev.* 1 (2014) 1–12.
- [4] R. Boyer, G. Welsch, E.W. Collings, *Materials Properties Handbook: Titanium Alloys*, ASM International, Materials Park (OH), 1994.
- [5] G. Lütjering, J.C. Williams, A. Gysler, Microstructure and mechanical properties of titanium alloys, in: J.C.M. Li (Ed.), *Microstruct. Prop. Mater.*, World Scientific, Singapore, 1998, pp. 1–77.
- [6] C.G. Rhodes, J.C. Williams, Observations of an interface phase in the α/β boundaries in titanium alloys, *Metall. Trans. A* 6 (1975) 1670–1671.
- [7] H. Margolin, E. Levine, M. Young, The interface phase in alpha-beta titanium alloys, *Metall. Trans. A* 8 (1977) 373–377.
- [8] C.G. Rhodes, N.E. Paton, Formation characteristics of the α/β interface phase in Ti-6Al-4V, *Metall. Trans. A* 10 (1979) 209–216.
- [9] D. Banerjee, J.C. Williams, The effect of foil preparation technique on interface phase formation in Ti alloys, *Scripta Metall.* 17 (1983) 1125–1128.
- [10] C. Servant, C. Quesne, T. Baudin, R. Penelle, Contribution to the analysis of the α/β interface in some titanium alloys, *J. Mater. Res.* 6 (2011) 987–998.
- [11] M. Yan, M.S. Dargusch, T. Ebel, M. Qian, A transmission electron microscopy and three-dimensional atom probe study of the oxygen-induced fine microstructural features in as-sintered Ti-6Al-4V and their impacts on ductility, *Acta Mater.* 68 (2014) 196–206.
- [12] D. Mangelinck, F. Panciera, K. Hoummada, M. El Kousseifi, C. Perrin, M. Descours, A. Portavoce, Atom probe tomography for advanced metallization, *Microelectron. Eng.* 120 (2014) 19–33.
- [13] S.S. Al-Bermani, M.L. Blackmore, W. Zhang, I. Todd, The origin of microstructural diversity, texture, and mechanical properties in electron beam melted Ti-6Al-4V, *Metall. Mater. Trans. A* 41 (2010) 3422–3434.
- [14] Y.H. Kok, X.P. Tan, S.B. Tor, C.K. Chua, Fabrication and microstructural characterisation of additive manufactured Ti-6Al-4V parts by electron beam melting, *Virtual Phys. Prototyp.* 10 (2015) 13–21.
- [15] A.A. Antonysamy, J. Meyer, P.B. Prangnell, Effect of build geometry on the β -grain structure and texture in additive manufacture of Ti6Al4V by selective electron beam melting, *Mater. Charact.* 84 (2013) 153–168.
- [16] A. Saifdar, L.-Y. Wei, A. Snis, Z. Lai, Evaluation of microstructural development in electron beam melted Ti-6Al-4V, *Mater. Charact.* 65 (2012) 8–15.
- [17] J. Karlsson, A. Snis, H. Engqvist, J. Lausmaa, Characterization and comparison of materials produced by Electron Beam Melting (EBM) of two different Ti-6Al-4V powder fractions, *J. Mater. Process Technol.* 213 (2013) 2109–2118.
- [18] L.E. Murr, S.M. Gaytan, F. Medina, E. Martinez, J.L. Martinez, D.H. Hernandez, B.I. Machado, D.A. Ramirez, R.B. Wicker, Characterization of Ti-6Al-4V open cellular foams fabricated by additive manufacturing using electron beam melting, *Mater. Sci. Eng. A* 527 (2010) 1861–1868.
- [19] S.J. Li, L.E. Murr, X.Y. Cheng, Z.B. Zhang, Y.L. Hao, R. Yang, F. Medina, R.B. Wicker, Compression fatigue behavior of Ti-6Al-4V mesh arrays fabricated by electron beam melting, *Acta Mater.* 60 (2012) 793–802.
- [20] L.E. Murr, E.V. Esquivel, S.A. Quinones, S.M. Gaytan, M.I. Lopez, E.Y. Martinez, F. Medina, D.H. Hernandez, E. Martinez, J.L. Martinez, S.W. Stafford, D.K. Brown, T. Hoppe, W. Meyers, U. Lindhe, R.B. Wicker, Microstructures and mechanical properties of electron beam-rapid manufactured Ti-6Al-4V biomedical prototypes compared to wrought Ti-6Al-4V, *Mater. Charact.* 60 (2009) 96–105.
- [21] N. Hrabe, T. Quinn, Effects of processing on microstructure and mechanical properties of a titanium alloy (Ti-6Al-4V) fabricated using electron beam melting (EBM), part 1: distance from build plate and part size, *Mater. Sci. Eng. A* 573 (2013) 264–270.
- [22] L. Ladani, J. Razmi, S. Farhan Choudhury, Mechanical anisotropy and strain rate dependency behavior of Ti6Al4V produced using E-beam additive fabrication, *J. Eng. Mater. Technol.* 136 (2014) 031006-1–031006-7.
- [23] K. Thompson, D.T. Lawrence, D.J. Larson, J.D. Olson, T.F. Kelly, B. Gorman, In situ site-specific specimen preparation for atom probe tomography, *Ultramicroscopy* 107 (2007) 131–139.
- [24] D.J. Larson, D.J. Foord, A.K. Petford-Long, H. Liew, M.G. Blamire, A. Cerezo, G.D.W. Smith, Field-ion specimen preparation using focused ion-beam milling, *Ultramicroscopy* 79 (1999) 287–293.
- [25] O. Hellman, J. Vandebroucke, J. Rüsing, D. Isheim, D. Seidman, Analysis of three-dimensional atom-probe data by the proximity histogram, *Microsc. Microanal.* 6 (2000) 437–444.
- [26] M.K. Miller, *Atom Probe Tomography*, Springer, US, Boston, MA, 2000.
- [27] J.S. Tiley, Modeling of Microstructure Property Relationships in Ti-6Al-4V, Ph.D. Thesis, The Ohio State University, 2002.
- [28] J. Schwerdtfeger, R.F. Singer, C. Körner, In situ flaw detection by IR-imaging during electron beam melting, *Rapid Prototyp. J.* 18 (2012) 259–263.
- [29] F.P. Incropera, *Introduction to Heat Transfer*, John Wiley & Sons, 2011.
- [30] J. Sieniawski, W. Ziaja, K. Kubiak, M. Motyka, Microstructure and mechanical properties of high strength two-phase titanium alloys, *Titan. Alloy. Prop. Control* (2013) 69–80.
- [31] T. Ahmed, H.J. Rack, Phase transformations during cooling in $\alpha + \beta$ titanium alloys, *Mater. Sci. Eng. A* 243 (1998) 206–211.
- [32] F.X. Gil Mur, D. Rodríguez, J.A. Planell, Influence of tempering temperature and time on the α' -Ti-6Al-4V martensite, *J. Alloys Compd.* 234 (1996) 287–289.
- [33] H. Matsumoto, H. Yoneda, K. Sato, S. Kurosu, E. Maire, D. Fabregue, T.J. Konno, A. Chiba, Room-temperature ductility of Ti-6Al-4V alloy with α' martensite microstructure, *Mater. Sci. Eng. A* 528 (2011) 1512–1520.
- [34] F. Cortial, The α/β interface phase in titanium alloys: Artifact or real phase contribution to problem resolution, *Metall. Mater. Trans. A* 25 (1994) 241–248.
- [35] I. Katzarov, S. Malinov, W. Sha, Finite element modeling of the morphology of β to α phase transformation in Ti-6Al-4V alloy, *Metall. Mater. Trans. A* 33 (2002) 1027–1040.
- [36] X.P. Tan, C. Perrin-Pellegrino, K. Hoummada, D. Mangelinck, A.R. Vande Put, M.-C. Lafont, D. Oquab, D. Monceau, Atom probe tomographic study of L10 martensite in a Pt-modified NiCoCrAlYTa bond coating, *Corros. Sci.* 76 (2013) 1–5.
- [37] J.S. Kim, J.H. Kim, Y.T. Lee, C.G. Park, C.S. Lee, Microstructural analysis on boundary sliding and its accommodation mode during superplastic deformation of Ti-6Al-4V alloy, *Mater. Sci. Eng. A* 263 (1999) 272–280.
- [38] R.W. Armstrong, Engineering science aspects of the Hall-Petch relation, *Acta Mech.* 225 (2014) 1013–1028.
- [39] D. Lee, S. Lee, C. Lee, S. Hur, Effects of microstructural factors on quasi-static and dynamic deformation behaviors of Ti-6Al-4V alloys with Widmanstätten structures, *Metall. Mater. Trans. A* 34 (2003) 2541–2548.
- [40] I. Sen, S. Tamirisakandala, D.B. Miracle, U. Ramamurti, Microstructural effects on the mechanical behavior of B-modified Ti-6Al-4V alloys, *Acta Mater.* 55 (2007) 4983–4993.
- [41] E.B. Shell, S.L. Semiatin, Effect of initial microstructure on plastic flow and dynamic globularization during hot working of Ti-6Al-4V, *Metall. Mater. Trans. A* 30 (1999) 3219–3229.

- [42] J.P. Hirth, J. Lothe, *Theory of Dislocations*, Krieger, FL, 1992.
- [43] S.L. Semiatin, T.R. Bieler, The effect of alpha platelet thickness on plastic flow during hot working of Ti-6Al-4V with a transformed microstructure, *Acta Mater.* 49 (2001) 3565–3573.
- [44] B. Vandenbroucke, J. Kruth, Selective laser melting of biocompatible metals for rapid manufacturing of medical parts, *Rapid Prototyp. J.* 13 (2007) 196–203.
- [45] J.R. Cahoon, W.H. Broughton, A.R. Kutzak, The determination of yield strength from hardness measurements, *Metall. Trans.* 2 (1971) 1979–1983.
- [46] J.R. Cahoon, An improved equation relating hardness to ultimate strength, *Metall. Trans.* 3 (1972) 3040.
- [47] D.R. Askeland, *The Science and Engineering of Materials*, Springer, US, Boston, MA, 1996.
- [48] E.J. Pavlina, C.J. Van Tyne, Correlation of yield strength and tensile strength with hardness for steels, *J. Mater. Eng. Perform.* 17 (2008) 888–893.
- [49] S.H. Hashemi, Strength–hardness statistical correlation in API X65 steel, *Mater. Sci. Eng. A* 528 (2011) 1648–1655.
- [50] W. Lu, Y.W. Shi, X.Y. Li, Y.P. Lei, Correlation between tensile strength and hardness of electron beam welded TC4-DT joints, *J. Mater. Eng. Perform.* 22 (2013) 1694–1700.
- [51] J. Luo, M.Q. Li, W.X. Yu, H. Li, The variation of strain rate sensitivity exponent and strain hardening exponent in isothermal compression of Ti-6Al-4V alloy, *Mater. Des.* 31 (2010) 741–748.
- [52] D.J. Abson, F.J. Gurney, Hardness, strength, and elongation correlations for some titanium-base alloys, *Met. Technol.* 1 (1974) 483–489.
- [53] J.J. Sobczak, L.B. Drenchev, *Metal Based Functionally Graded Materials*, Bentham Science Publishers, 2009.
- [54] K. Lu, Making strong nanomaterials ductile with gradients, *Science* 345 (2014) 1455–1456.